Magneto–Optical Kerr Effect Microscopy Investigation on Permalloy Nanostructures

Zulzawawi Bin Haji Hujan

A thesis submitted for the degree of

MSc by research

University of York

Department of Physics

January 2013

Abstract

This thesis focuses on the investigation of magnetic domains in ultrasmall permalloy ($Ni_{80}Fe_{20}$) structures down to nanometre size. Magnetic domains and domain walls in nano objects are often observed using a very high resolution and high power microscope such as magnetic soft x-ray microscope, magnetic force microscopy imaging and photoemission electron microscopy. A reason for this is because the Kerr signal in nanostructures is very weak. However the results from this thesis demonstrate that magnetic domains in permalloy magnetic nanostructures can still be observed with very good contrast using a Magneto-optical Kerr effect (MOKE) microscope. The constructed Kerr microscope is a home-build wide field microscope and is able to produce magnetic domains image of permalloy nanowire as small as 245 nm, although the resolution limit of the microscope is 505 nm. For the first time, a magnetic domain in nanowire with width of 245 nm is observed using a wide-field microscope. The combination of hysteresis loops and magnetic domains observations for studying a magnetic sample provides a three-dimensional understanding of the magnetic characteristic of the sample. This is crucial in investigating nano samples as the theoretical arguments with the experimental results are always constrained by the experimental part. Three kinds of nanostructure sample were observed using the Kerr microscope; a cross nanowire, zigzag nanowire and a nanowire with notch and a nucleation pad at one end. It was found that a cross nanowire can form magnetic domains upon reversal and the junction forms a magnetisation vortex. Findings from zigzag nanowire demonstrate a complex, multiple magnetic domains formation upon magnetisation reversal. A weak domain wall pinning effect was observed in the nanowire, causing a multiple domains formation in the nanowire upon reversal. It can be confirmed that this effect was caused by the high coercivity of the nucleation pad. For the nanowire with notch, it was demonstrated that the coercivities were different at negative and positive field. But for such case, there is a relationship observed between the percentage notch depth and the coercivity at the junction.

Table of Contents

Acknowledgement

I would like to take this opportunity to thank all the people who have helped and support me all the way through my Master. First of all I would like to thank my supervisor, Dr Jing Wu who supervised my work and giving me ideas. Also, thanks to Xuefeng Hu who was making all the samples for my experiment. I would like to thank Tuyuen Cheng for his support and help throughout my Master. I would also like to express my gratitude to Prof Yongbing Xu for his advice on writing my thesis. I would like to extend my gratitude to my parents whom always giving me supports throughout my master. Last but not least, I would like to thank Siti Raheemah for being supportive and taking care of me at all time throughout my Master.

Declaration

I hereby declare that the work contained in this thesis is my own and has not been submitted for examination for any other degree at any University. All collaborators works have been acknowledged in this thesis. All the nickel iron ($Ni_{80}Fe_{20}$) samples mentioned in the thesis were fabricated by Xuefeng Hu. And the simulation result for one sample mentioned in the result chapter was done also by Xuefeng Hu. Both the fabrications and simulation were done in the University of York.

1. Introduction and Background theory

1.1 Introduction

Study of magnetism has been of interest for centuries, the first known magnetic material was magnetite (Fe_3O_4) and its earliest description was recorded around 2500 years ago. But at that time, the development and study of magnetism was very limited not until 1920 when the first understanding of the relationship between electricity and magnetism was introduced by Hans Christian Oersted. He discovered that an electric current produces magnetic field. Along with the first electromagnet built in 1825, the study of magnetic materials increased dramatically because of the available high power magnetic fields produced using electromagnet [1].

In 1898, Valdemar Poulsens's invented the telegraphone to record voice [2]. This was the beginning of the magnetic storage phenomenon. Further in nineteen fifties the first commercial hard disk drive was introduced by IBM with only 4.4 megabyte of storage density. The small storage density of the hard disk drive continued to increase significantly until in the year 2000 where the increase is in the order of five magnitude as shown in Figure 1.1. Recently, the areal density of the HDD is more than 250 Gb/in^2, and densities as high as 520 Gb/in2 have been demonstrated in the laboratory [3]. The change of the areal density of magnetic storage can be seen on Figure 1.1 showing how the high demand for magnetic storage had an impact on the immense development in magnetic storage. The introduction of perpendicular recording in 2005 has largely increased the areal density of HDD. But further increase of the areal density is hindered due to the superparamagnetic effect. Superparamagnetic effect refers to the fluctuation of magnetisation due to thermal agitation when the magnetic grain size (bit size) is too small.

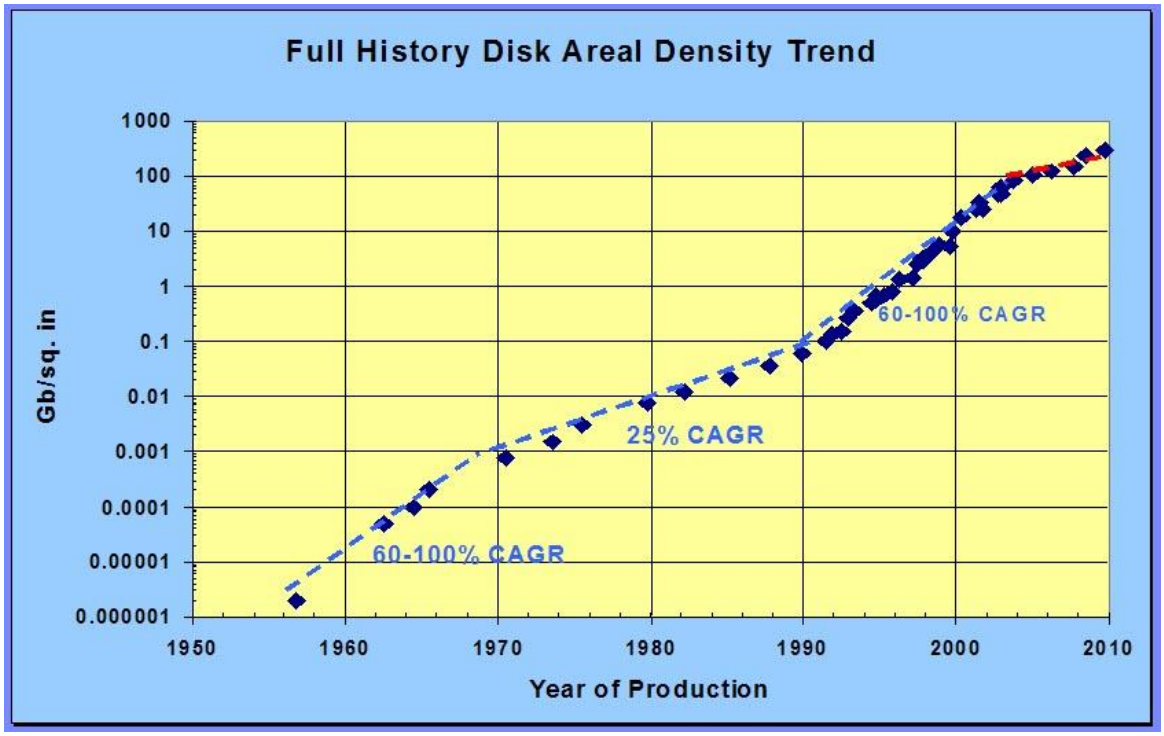

Figure 1.1: Graph showing the increasing areal density of HDD [4].

With the magnetic recording as the key technology to support the information technology for our daily life, a lot of efforts were made to find other methods of information storage. One of the proposed methods was the use of nano magnetic objects as a high density magnetic storage device [5] and other well-known example is the magnetic domain-wall racetrack memory [6]. Though, the possible use of nano magnetic objects is not only limited to magnetic storage. For instance, the ferromagnetic nanowires are said to have the potential for future magnetic and spintronic devices such as magnetic diode [7] and magnetic logic gate [8]. Because of the possibility of nanowires as the future spintronic devices, interest in the study of magnetic nanowires has enormously increased. A lot of studies and researches have been conducted to understand the magnetic properties of nanostructures materials. However, understanding of the magnetic properties of nanostructures objects is still a challenging theoretical issue as well as experimental issue.

1.2 Background theory

1.2.1 Ferromagnetism

Iron, cobalt, nickel, and permalloy such as nickel iron ($Ni_{80}Fe_{20}$) are examples of ferromagnetic materials. In 1907, Pierre Weiss published his hypothesis on ferromagnetic materials [9], which gives an in-depth understanding of ferromagnetic materials behaviour for the first time. The hypothesis explains that magnetic moments in ferromagnetic materials interact with each other where every single one of them tries to align the others in its own direction. This hypothesis leads to the Curie Weiss law:

$$\chi = \frac{C}{T - \theta_{Weiss}}, \qquad \text{Equation 1.1}$$

where χ is the magnetic susceptibility of the material, *C* is the curie constant, *T* is the absolute temperature and θ_{Weiss} is the Curie-Weiss constant, Ferromagnetic material remains its magnetisation even after removing the applied magnetic field. Weiss theory deduced that the existence of magnetic domains in ferromagnetic materials explains their demagnetisation state but Weiss did not explain the origin of magnetic domains. Therefore Heisenberg came up with a theory by using quantum mechanical approach to describe these domains. He explained that the origins of these domains are the result of exchange interactions between magnetic moments in ferromagnetic materials. Both theories will be explained in the next section below.

1.2.2 Weiss theory

The most important advancement in understanding ferromagnetic was the introduction of ferromagnetic domain concept introduced by Weiss in two papers [9, 10]. These two papers were developed based on the earlier work of Ampere, Weber and Ewing which proposed the existence of magnetic domains in ferromagnetic material. It also explains that magnetic moments are in order even in demagnetized state and these magnetic domains are consistently reorienting during magnetisation process by external magnetic field. As explained before that these magnetic domains will stay in the aligned order until it reaches the Curie temperature where the

ferromagnetic properties will change to paramagnetic. To explain this change, Weiss use the Langevin model of paramagnetism where it uses the Curie law of paramagnetic susceptibility to calculate the change in ferromagnetic to paramagnetic properties.

Weiss theory was a pioneer in explaining the spontaneous magnetisation in ferromagnetic materials. In the Weiss theory, it proposes the mean (molecular) field, H_m to be proportional to the spontaneous magnetisation, M_s of the magnetic domain and gives [11]:

$$H_m = \alpha_m M_s \,, \qquad \text{Equation 1.2}$$

where α_m is the mean field constant. The Weiss molecular field is the effect in the interatomic interaction causing the neighbouring magnetic moments to align parallel to each other in order to reach the lowest energy state. This shows that the interaction between magnetic moments in atoms causing the molecular field which is an internal field that is strong enough to magnetise the material without the presence of external applied magnetic field. Therefore the effective magnetic field acting within a magnetic domain is:

$$H_{eff} = H + H_m \,, \qquad \text{Equation 1.3}$$

where H is the external magnetic field. Using Weiss theory, it generates the value of molecular field, H_m in iron to be of the order 10^7 Oe [12]. But it only takes a field of the order 1 Oe to rearrange the domains in iron and 10^3 Oe and to remove them. Above the Curie temperature, the Curie law becomes:

$$\frac{M}{(H + \alpha_m M_s)} = \frac{C}{T} \,. \qquad \text{Equation 1.4}$$

Using $M = \chi H$ gives:

$$\chi = \frac{C}{(T - C\alpha_m)} = \frac{C}{(T - T_c)} \,, \qquad \text{Equation 1.5}$$

where T_c is the Curie temperature but when the temperature is above T_c, θ_{Weiss} is used as shown in Equation 1.1. This explains the paramagnetic properties of ferromagnetic material at temperature above Curie temperature.

Even though Weiss theory seems to be invalid, it is actually logical in describing the approximation of a coupling force between spin and can be used to describe basic understanding of ferromagnetism. Furthermore, there are general agreement between the theoretical results of Weiss theory and experimental results for sample like Fe, Ni [13] and Co. It is concluded that Weiss field theory is too simple as it did not include the thermal fluctuations and the possible fluctuations between spins.

As a final point, Weiss theory successfully describes the temperature dependence paramagnetic susceptibility well above the Curie temperatures shown in Figure 1.2 but at low temperature it needs the exchange interaction approach.

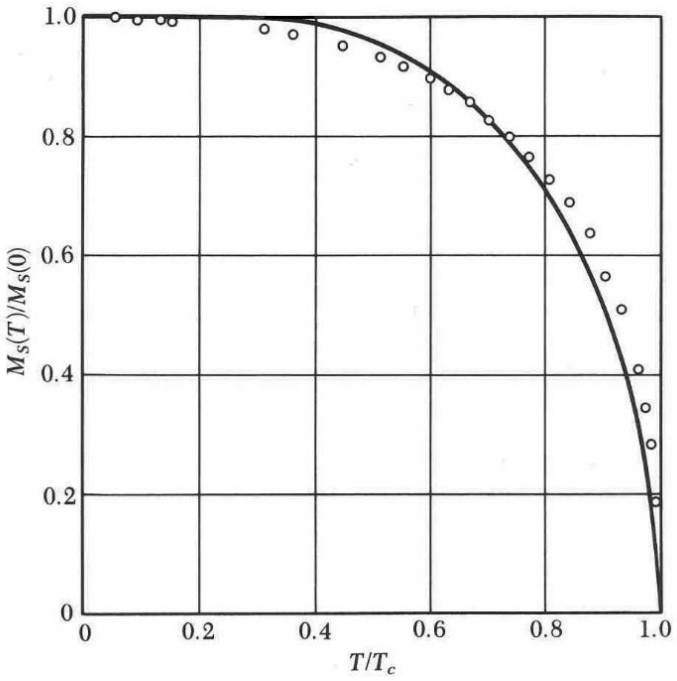

Figure 1.2: The saturation magnetization of nickel as a function of temperature [14]. This curve of M versus T is produced in this way to show roughly the experimental results.

1.2.3 Exchange interaction theory

A quantum theory approach is required to explain ferromagnetism. The Weiss theory did not try to mention anything about the origin of the molecular field. Origin of the molecular field was not understood until in 1928 [15], Heisenberg proved that it was

caused by the quantum mechanical exchange interaction in the atoms. Heisenberg Theory is based on the Pauli exclusion principle. The Heisenberg exchange interaction based on effective interaction between the two neighbouring electron spins is written as:

$$E_{exc} = -2J_{ij}S_iS_j\,, \qquad \text{Equation 1.6}$$

where $S_i$andS_j are the spin angular momentum vectors of the two electrons and J_{ij} refers to the exchange integral between the two electrons. If the exchange integral is positive (J_{ij}>0), it will give ferromagnetism where parallel arrangement is favoured as it gives the lowest energy. When J is negative and large, it will give antiferromagnetic or ferromagnetic where the spins alignment will be anti-parallel as it gives favourable lowest energy.

Exchange interaction depends mainly on interatomic distance and it decreases rapidly with distance. This means that the summation of the total exchange interaction is limited to the nearest neighbour pairs only. As a result, the total exchange interaction can be written as:

$$E_{exc} = -2\sum_{i,j} J_{ij}S_iS_j \qquad \text{Equation 1.7}$$

Heisenberg theory explains precisely why the ferromagnetic atoms tend to align parallel to each other.

1.2.4 Hysteresis loop

The hysteresis loop phenomenon in ferromagnetic material is caused by the magnetisation reversal of the magnetic domains when an external magnetic is applied. Therefore one can relate the magnetic characteristic of the material to the hysteresis loop properties of that material. Referring to Figure 1.3, hysteresis loops show the graph of the magnetic induction, B versus the applied magnetic field, H. Once the material attains saturation, all the magnetic moments will align in one direction. The slope in hysteresis loop means that the magnetisations of the magnetic domains are not reversed at the same time. This is what usually happen in

bulk sample, however a large jump usually occur in thin film sample where the magnetic domains reverse nearly at the same time. In Figure 1.3, the curve ABCD shows the magnetisation rotation from the positive magnetic field direction to the negative magnetic field direction (opposite) and the curve DEFA shows the magnetisation rotation from negative magnetic field direction back to the positive magnetic field direction.

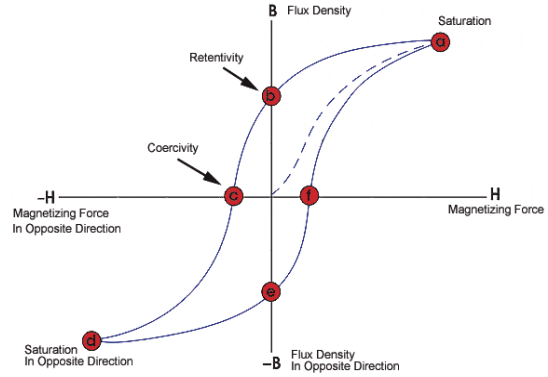

Figure 1.3: Graph of hysteresis loop to study the magnetic characteristic of the magnetic sample [16]. The coercivity is the amount of magnetic field required to reduce the magnetisation of the material to zero and retentivity or remanence is a measure of the remaining magnetisation when the applied magnetic field is dropped to zero.

1.2.5 Magnetic domains and domain walls

As explained before, Weiss hypothesized the existence of magnetic domains in ferromagnetic materials to explain the demagnetisation state. He proposed that the demagnetisation state in magnetic materials is caused by the magnetic domains which are regions with their magnetisation in different directions so that the net magnetisation is zero. Nonetheless, Weiss theory did not describe the origin of the ferromagnetic domains and the hysteresis loop phenomena. The first experimental proof of the existence of magnetic domains was the well-known Sixtus and Tonks experiments done by Barkhausen [17] where he observed the magnetisation reversal of stressed nickel wires which showed the magnetisation reversal occurred by a single large jump between two opposite saturated states. In 1932, Bitter obtained the first ever images of the magnetic domains using a powder technique [18]. Later in 1935, Landau and Lifshiftz explained that the sub-divisions of magnetic

domains occurred in order to reduce the magnetostatic energy due to saturation in the magnetic sample [19]. The magnetostatic energy can be evaluated as:

$$E_m = \frac{\mu_0}{2} \int H_{Stray}^2 dV \,, \qquad \text{Equation 1.8}$$

where μ_0 is the permeability of free space. The equation E_m presents the interaction of dipoles with the field H_{stray} produced from the other dipole and dV is the volume of space. The $\frac{1}{2}$ is included to prevent from counting the interaction twice. Although the interaction of dipoles is much weaker than the powerful exchange interaction that occurs in short range distance, but in long range the dipoles interaction is dominant. Therefore dipoles interaction is very important in describing the properties of magnetic moments in long range distance that is linked to the formation of magnetic domains specifically to reduce the magnetostatic energy. The dipoles interaction causing the magnetic domains formation can be explained by referring to Figure 1.4.

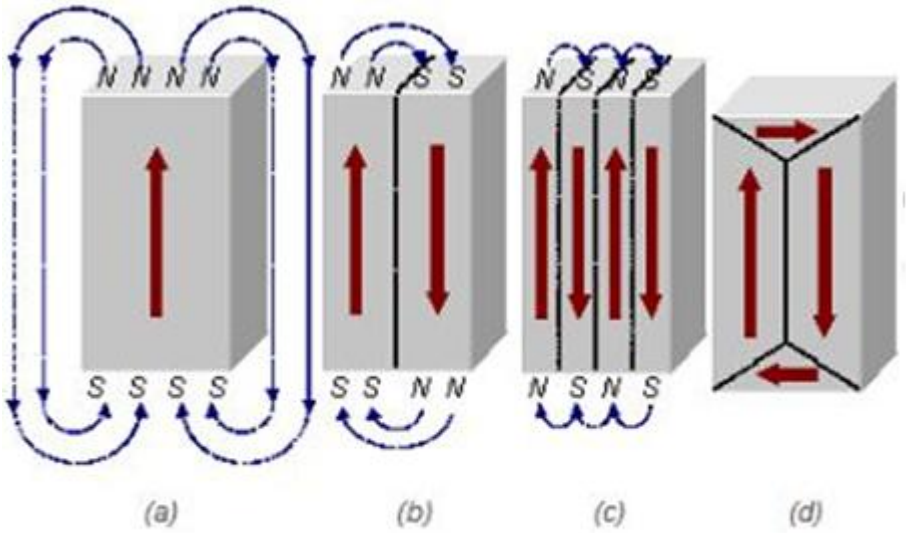

Figure 1.4: Schematic description of the reduction of magnetostatic energy by formation of magnetic domain [20].

From Figure 1.4 (a) shows a large magnetostatic energy resulted from the magnetic poles at the surface of the material which causes the stray field. After that, the magnetic domain is divided into two as shown on Figure 1.4 (b) which reduces the magnetostatic energy by half. Further in Figure 1.4 (c) there are four magnetic domains which further reduce the magnetisation energy into quarter than the one in

the saturation state. And finally in Figure 1.4 (d) shows the closure of domains structure where the net magnetisation of the material is equal to zero. Additional divisions of magnetic domains can also occur but only up to when the energy for the formation of each additional domain wall is greater than the reduction in the magnetostatic energy. Therefore the size of magnetic domain also depends on this new factor known as the magnetic domain walls which will be described later. And lastly, more complicated magnetic domain patterns can exist in different shape materials and different constituent of magnetic material.

1.2.6 Shape anisotropy

For a small patterned magnetic structure, the sample can be saturated along the direction of the applied magnetic field to give a single magnetic domain of the sample. Such sample can retain its single domain magnetisation or form sub-divisions magnetic domains without the applied magnetic field, given that the size and shape is less than the critical value of the material. Likewise, the formed domain patterns characteristic is more favourable due to the shape and size of the sample effect related to the magnetostatic energy of the sample. The shape anisotropy energy density can be derived from the magnetostatic energy related to the stray field produced by the magnetic dipoles on the sample surface which gives:

$$\varepsilon_s = \frac{1}{2}\mu_0 M_s^2 (N_a cos^2\theta + N_b sin^2\theta) \ , \qquad \text{Equation 1.9}$$

where N_a is the demagnetization factor parallel to the easy-axis, θ is the angle between the easy axis and the magnetisation and N_b stands for the demagnetization factor perpendicular to the easy-axis of the sample. Therefore, as an example, a nanowire wire will have its easy axis along the wire plane as this is much more favourable due to the shape anisotropy effect for lowest energy. Other example is an elliptical shape sample as shown on Figure 1.5 where the more favourable magnetisation direction is along the long axis of the sample. In addition, the saturation magnetic field is higher along the short axis than saturation magnetic field along the easy axis due to the higher magnetostatic energy for the short axis.

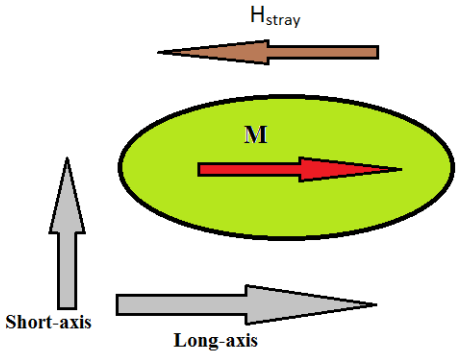

Figure 1.5: Schematic diagram of an elliptical shaped sample showing it's long axis and short axis.

1.3 Different energy densities in ferromagnetic material

The energy of different magnetic domains arrangements are not only from the magnetostatic energy contributions, but also from other different energy contributions. The other energy contributions will be discussed in this section in details in order to understand the generalised concept of different magnetisation directions and different magnetic domains formations in the ferromagnetic materials. It is also important to know the sources of the energies that influence such domains arrangement in order to do micromagnetic calculation of the magnetisation distribution in the ferromagnetic sample. There are five main energy contributions; magnetocrystalline anisotropy, exchange energy, magnetoelastic energy, magnetostatic energy and zeeman energy.

1.3.1 Magnetocrystalline anisotropy

Magnetocrystalline anisotropy describes the tendency of the magnetisation direction of the material along a certain crystallographic directions. This preferred crystallographic axis is called the easy axis and the direction where the magnetisation direction is the least favourable is known as the hard axis. It is

experimentally proven that the hard axis has higher saturation field than the easy axis.

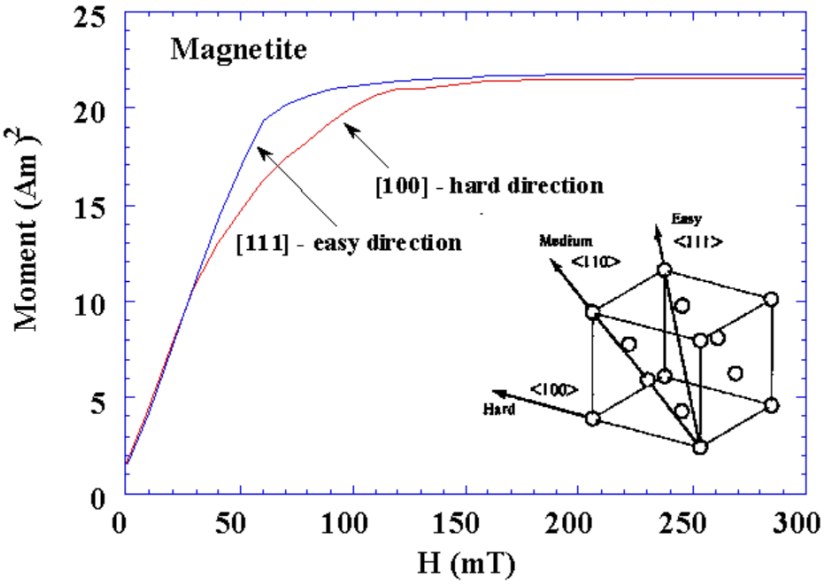

Figure 1.6: Magnetisation curve of magnetite for easy and hard axis [21].

From Figure 1.6, the preferred easy axis of magnetite is the [111] axis and the hard axis is the [100] axis. And as shown by the curve, the saturation field for the easy axis is lower than the saturation field for the hard axis. The magnetocrystalline anisotropy energy density for cubic crystals such as iron and nickel is:

$$\varepsilon_a = K_1 (a_1^2 a_2^2 + a_2^2 a_3^2 + a_3^2 a_1^2) + K_2 (a_1^2 a_2^2 a_3^2) + \dots , \qquad \text{Equation 1.10}$$

where, K_1 and K_2 are the respective primary and secondary anisotropy constants for the material and $\alpha_{1,2,3}$ are the directional cosines relative to the cube edges. For nickel, the values of K_1 and K_2 are -4.5 x 10^3J/m^3 and -2.5 x 10^3 J/m^3 respectively [22]. And the magnetocrystalline anisotropy energy density for the uniaxial materials such as cobalt is:

$$\varepsilon_a = K_1 sin^2\theta + K_2 sin^4\theta \dots \qquad \text{Equation 1.11}$$

where θ is the angle between the easy axis and magnetisation. Experimentally, the constants for cobalt at room temperature are: K_1=4.1x10^5J/m^3 and K_2=1.5x10^5 J/m^3 [23].

As the effect of magentocrystalline anisotropy always appear in a single crystal, therefore in polycrystalline samples the magentocrystalline anisotropy will be averaged throughout the random orientation of each crystallite formations. It is proved by Bozorth that the magnetocrystalline anisotropy for nickel-iron alloys, depends largely on the percentage content of nickel content [24]. The curve relating the nickel content in nickel iron with the anisotropy constants of the nickel iron is shown in Figure 1.7.

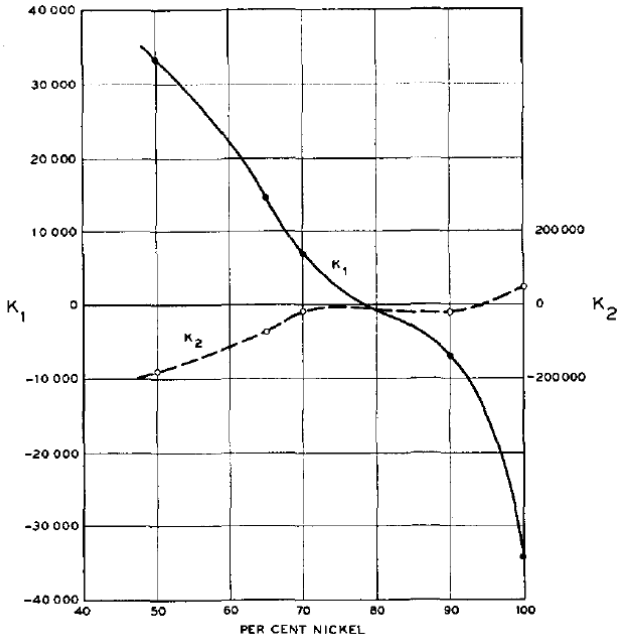

Figure 1.7: Variation of anisotropy constants of nickel iron at different percentage content of nickel at room temperature [24]. The solid curve represents the variation of the magnetocrystalline anisotropy constant, K_1 and the dotted line represents the magnetocrystalline anisotropy constant, K_2 at different content of nickel in nickel iron.

1.3.2 Exchange energy

The exchange energy is the energy that keeps the magnetic moments to be aligned parallel to each other. This is described before as the interaction energy for the short range distance with the nearest neighbour. Therefore the energy to change the direction of the magnetisation is called the exchange energy and is given in the form:

$$\varepsilon_{ex} = A \sum_{i=1}^{3} (\nabla \alpha_i(r)^2) \, . \qquad \text{Equation 1.12}$$

In this equation, A is the exchange stiffness constant (J/m) which is temperature dependent and $\alpha_{1,2,3}$ are the direction cosines of the spin at lattice point r.

1.3.3 Magnetoelastic energy

Magnetoelastic energy is part of the magnetocrystalline anisotropy that depends on the mechanical strain on the material. When strain is applied to the crystal lattice, the distances between the atoms are shifted causing change to the interaction energies and this effect is called the magnetoelastic energy. Clearly, for a crystal lattice which has no strain will has zero magnetoelastic energy and therefore its magnetisation is determined by other magnetic anisotropy. With the spin-orbit coupling effect known as magnetostriction with symbol λ_s defined for various lattice directions, the magnetoelastic energy density is derived as:

$$\varepsilon_{me} = \frac{3}{2}(\lambda_s \sigma sin^2\theta), \qquad \text{Equation 1.13}$$

where σ is the stress and θ is the angle between the stress direction and the magnetisation direction. Stress in thin films and multilayer can be applied during fabrication of sample by applying thermal stress and different lattice alignments between layers.

1.3.4 Magnetostatic energy

The magnetostatic energy is described in the previous section and its density is:

$$\varepsilon_m = \frac{\mu_0}{2} \boldsymbol{H_{Stray}}.\boldsymbol{M_s} \, , \qquad \text{Equation 1.14}$$

where $\boldsymbol{M_s}$ is the saturation magnetisation vector. As discussed previously, the magnetostatic energy is caused by the stray field, $\boldsymbol{H_{Stray}}$ resulted from the magnetic

dipole on the surface of the material. Additionally the stray field will always try to oppose the direction of the saturation magnetisation, $\boldsymbol{M_s}$.

1.3.5 Zeeman energy

The Zeeman energy can be considered as the potential energy of a magnetic moment in a field. It is the energy caused by the interaction of the saturation magnetisation and the external applied magnetic field, therefore its energy density is written as:

$$\varepsilon_{zeeman} = -\mu_0 \boldsymbol{H_{Stray}}.\boldsymbol{M_s} \qquad \text{Equation 1.15}$$

1.4 Domain walls

From the previous discussion, the existence of the magnetic domains in ferromagnetic materials and how their specific orientations and properties are related to the energy contributions to the ferromagnets. It have been explained that it is very important to know that when magnetic domains exist in a region, there must be different directions of magnetic domains. Thus, there must be walls that separate different magnetic domains and they are known as the magnetic domain wall. Because the formation of magnetic domains is for energy minimisation, therefore domain walls are formed along with magnetic domains naturally. Thus, the energy of different domain walls orientation will also be balanced with the magnetostatic energy for having the one magnetic domain state. In general, domain wall configuration largely depends on the minimisation of exchange and anisotropy energy.

1.4.1 Bloch wall

Bloch wall is the transition layers between domains where the magnetisation changes from one domain to the other. It is known that the magnetisation of Bloch wall rotates along the axis perpendicular to the plane of the wall. Bloch walls form in

bulk material where the domain wall width is lot smaller than the magnetic material. Figure 1.8 shows the Bloch wall with total angular displacement of 180°. If the Bloch wall transition is over N atomic planes, therefore for the transition, one pair of spin will give exchange energy of:

$$F_{ij} \approx J_{exch} S^2 \left(\frac{\pi}{N}\right)^2 \qquad \text{Equation 1.16}$$

The exchange energy density of the spin transition can be written as:

$$\sigma_{exch} = J_{exch} S^2 \frac{\pi^2}{Na^2}, \qquad \text{Equation 1.17}$$

where J_{exch} is the exchange integral, S is the spin angular momentum and a is the lattice constant of the material. Certainly if N increases, the number of spin magnetic moments aligned in the hard axis will also increase. Therefore, there will be an increase in the magnetocrystalline anisotropy energy per unit area and it is given as:

$$\sigma_a = K_1 N a, \qquad \text{Equation 1.18}$$

where K_1 is the magnetocrystalline anisotropy. Furthermore, the total energy per unit area of the Bloch wall will be calculated by summation of the exchange energy density of the spin transition and the magnetocrystalline anisotropy energy per unit area, which gives:

$$\sigma_{Bloch} = \sigma_{exch} + \sigma_a \approx J_{exch} S^2 \frac{\pi^2}{Na^2} + K_1 N a . \qquad \text{Equation 1.19}$$

The total wall energy per unit area is a minimum with respect to N when

$$N_0 = \sqrt{\frac{J_{exch} S^2 \pi^2}{K_1 a^3}} = \frac{\pi}{a}\sqrt{\frac{A}{2K_1}}, \qquad \text{Equation 1.20}$$

where A is the exchange stiffness constant. The 180° Bloch wall energy density can be obtained by substituting Equation 1.20 into Equation 1.19 and the result is:

$$\varepsilon_{DW} = 4\sqrt{AK_1}. \qquad \text{Equation 1.21}$$

The wall thickness is in the order of

$$\delta_{Bloch} = Na = \pi\sqrt{\frac{A}{K_1}}. \qquad \text{Equation 1.22}$$

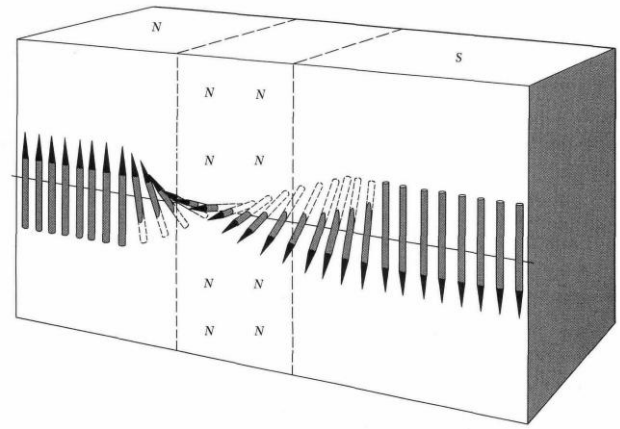

Figure 1.8: Picture showing the schematic of the micromagnetic structure of 180° Bloch wall [25].

1.4.2 Néel wall

In 1955 Neel demonstrated that the domain wall energy depends on the thickness of the sample when the thickness is less than a few hundred nanometres [26]. For a thin film sample, the thickness of the sample is comparable to the domain wall width. Therefore in this case, the energy related to the stray field on the sample surface at the Bloch wall becomes very large. The magnetostatic energy effect relative with the exchange and anisotropy energies will cause a change to the Bloch wall magnetic rotation alignment. The unfavorable formation of Bloch wall in thin film will cause the wall to change to Néel wall in which the magnetisation of the Néel wall is along the plane of the sample as shown in Figure 1.9. The result of this is a much lower overall energy and follows the anisotropy energy effect.

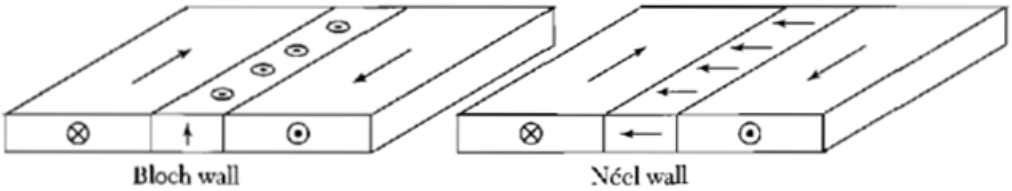

Figure 1.9: Schematic diagrams of the out of plane spin of Bloch wall and in plane spin of Néel wall [27].

The total energy per unit area of Néel wall can be calculated by including the exchange energy and the magnetocrystalline energy to give:

$$\sigma_{Neel} = 4\sqrt{A\left(K_1 + \frac{\mu_0}{2}M_s^2\right)}. \qquad \text{Equation 1.23}$$

Considering zero magnetocrytsralline anisotropy constant, K_1 as for NiFe will give Néel wall energy per unit area in the order of:

$$\sigma_{Neel} = M_s\sqrt{8\mu_0 A}\,. \qquad \text{Equation 1.24}$$

Therefore the width of Néel wall can be written as**:**

$$\delta_{Neel} = \pi\sqrt{\left(\frac{A}{K_1}\right) + \frac{2A}{\mu_0 M_S^2}}\,. \qquad \text{Equation 1.25}$$

Figure 1.9 shows the wall energy for Bloch and Neel walls in thin films, as functions of film thickness. From the curve, it is observed that the Bloch wall energy increases with film thickness around less than 40 nm width but Néel wall shows a decrease in energy causing the Néel wall to be more favourable.

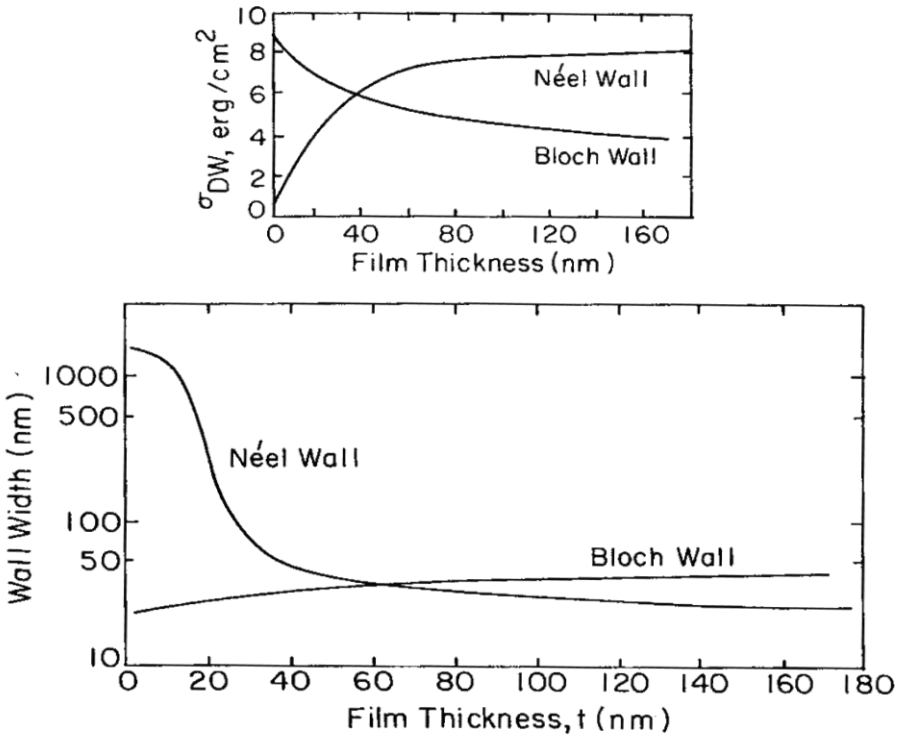

Figure 1.20: Curves showing the energy per unit area (top) and thickness (bottom)of a Bloch wall and a Neel wall as function of the film thickness. Parameters used are $A=10^{-11}$ J/m, B_s=1 T, and K=100 J/m^3 [23].

1.5 Magnetic domains and domain walls in permalloy nanowire

As this project involves the observation of magnetic domains in nanowire, it is essential to know the different types of domain walls formation in nanowire which gives the distinct properties of nanowire magnetisation. The thickness of nanowires are usually fabricated around few tens of nanometres but the axial length are significantly large, in the order of micrometres. The typical width of nanowire is in the order of hundreds of nanometres which is incomparably smaller than the long axis length. Nanowires can come in different forms or shapes such as zigzag nanowire and nanowire with notch connected to an elliptical pad. Nanowires have simple magnetisation distribution due to the geometry of nanowire. The nanowire magnetisations tend to align along the long axis of the nanowire due to the magnetostatic energy and the shape anisotropy of the nanowire. The magnetic

moment spin of permalloy nanowires or any ultrasmall magnetic samples prefer to be positioned parallel to the edges. Such effect is to reduce the magnetostatic energy of the nanowire and this agrees with the experimental results [28] shown in Figure 1.21.

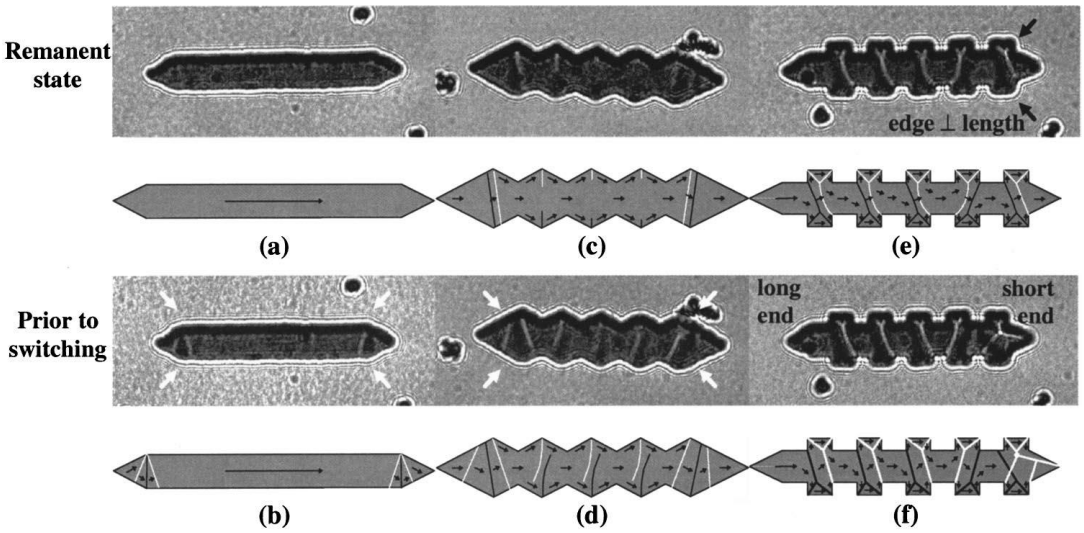

Figure 1.21: Fresnel images taken showing the distribution of magnetization within the samples. The overall length of all elements is 2.5 µm. In (b), white arrows mark the inner corners of element tips and n (d) white arrow marks the near end structures. The black arrows in (e) mark parts of the edge normal to the element length and close to the element end [28].

As a result of the shape anisotropy and the spin alignment parallel to the edge of sample, in elliptical pad the magnetic moments form a vortex as they follow the elliptic pattern of the sample edges. This caused the saturation field of the elliptical pad to be lower than a nanowire sample because by forming a vortex, it helps to reduce the energy for saturation magnetisation. Both theories are proven with the experimental results in [29].

Domain wall formation can be divided into two; the tail-to-tail and head-to-head domain walls depending on the 'head' or 'tail' side of the magnetic moment as shown on Figure 1.22.

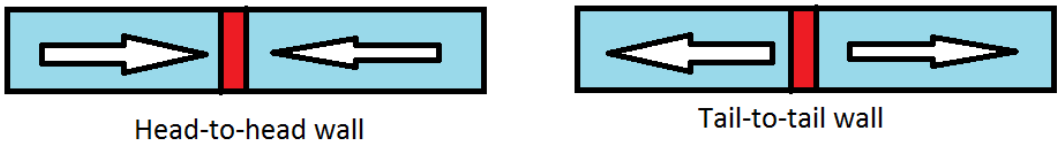

Figure 1.22: Schematic of the head-to-head and tail-to-tail domain walls.

There are three different domain walls structure; the transverse wall (TW), the vortex wall (VW) and the asymmetric transverse wall which is an intermediate state between the first two walls. The three different domain walls are shown in Figure 1.23 and simulation diagrams of the TW and VW are shown in Figure 1.24 [30] to demonstrate the detailed structure of magnetic moments in each wall. As the width and thickness of the nanowire is increased, a symmetric transverse will become distorted causing it to be asymmetric and thus forming the asymmetric transverse. Further increase in the nanowire width and thickness will increase the chance of the formation of vortex wall. Domain walls possess chirality where the magnetisation head or rotation can be either up or down. Chirality characteristic of domain walls is shown in Figure 1.23 where in the VW the rotation changes from clockwise to anti-clockwise. In a symmetric nanowire, different chiralities have equivalent energy state. Figure 1.25 from Nakatani [31] can be used to determine the type of domain walls at different wire widths and thickness.

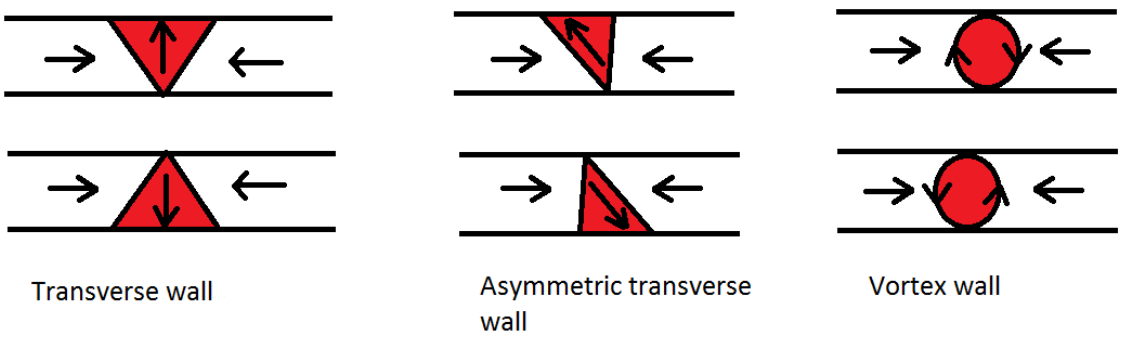

Figure 1.23: Different types of domain walls with chirality.

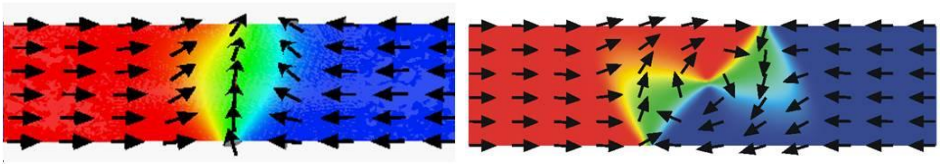

Figure 1.24: Example of detailed simulation of spins alignment for transverse wall (left) and vortex wall (right) [30].

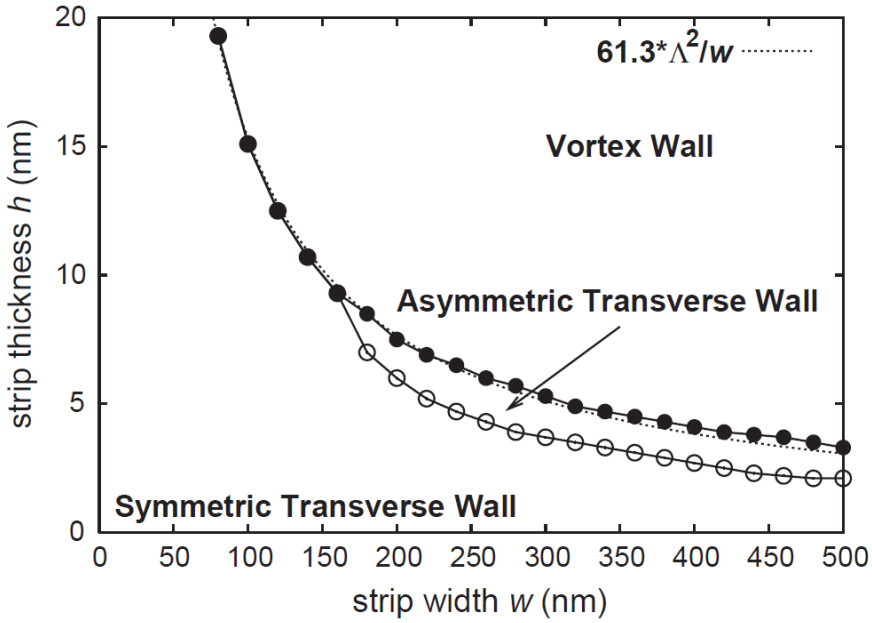

Figure 1.25: Curves showing the relationship between the permalloy nanowire width and the thickness of the domain wall formed [31].

From Figure 1.24, it shows the micromagnetic simulations of domain walls. Each of the arrows representing the spin can be divided into cells and the cell size depends on the exchange length value of the magnetic material. This length is very important for micromagnetic modelling that will be discussed in section 2.17. The micromagnetic exchange length of the nanowire is written as:

$$\Lambda = \sqrt{\frac{2A}{\mu_0 M_s^2}}, \qquad \text{Equation 1.26}$$

where A is the exchange parameter of the nanowire and M_s is the saturation magnetisation of the material. For nickel iron with A=13x10^{-12} J/m and M_s =860x10^3 A/m, the exchange length is around 5nm. This value will be used for micromagnetic

simulation to determine the cell size for the micromagnetic simulation of nickel iron. For a nanowire patterned with notch as what is going to be done for this project, the spin at the notch will align along the edges of the notch. The notch will change the domain walls nature in the nanowires by trapping and pinning.

1.6 Domain walls pinning behaviour in nanowire with notch

One of the nanowires that will be used for this project is a nanowire with notch connected to an elliptical pad as shown in Figure 1.26. The propagation of domain walls in notched nanowires has become a main interest for magnetic research. There are many proposed applications for such shape of nanowire, for examples as a magnetic logic [8], magnetic sensor [32] devices and as described before, as a magnetic memory storage [33]. The main theory for the possible use of this nanowire structure is the extreme control of the magnetisation direction in different parts of the wire by introducing notch and nucleation pad at the wire. Therefore the propagation of magnetic domain walls and the distribution of magnetisation will be controlled effectively and can be encoded as information stored in the wire. But this method requires a high control of domain wall propagation behaviour, therefore an intense investigations are needed to determine the effect of nucleation pad and notches in the propagation of domain wall.

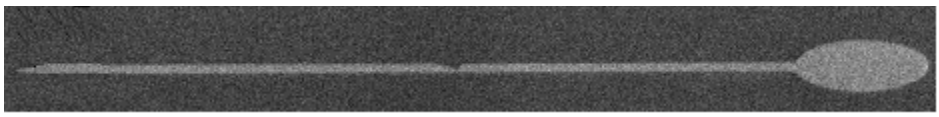

Figure 1.26: SEM image of a nanowire with notch and nucleation pad.

2. Experimental Method

2.1 Introduction

There are a lot of methods to observe magnetic domains but the classical Magneto-optical Kerr effect (MOKE) technique is the most versatile and has more advantages in comparison to other methods. MOKE is an effect when light reflected from a non-transparent magnetic sample can change in either polarisation or reflected intensity depending on the type of MOKE present in the sample. The types of MOKE will be discussed later in this chapter. Although the magnetic domain contrast is very weak, it can be enhanced by using digital image processing. Therefore, the development of digital image processing helps to increase the effectiveness of this method. With the many available image processing software products such as Matlab and LabVIEW, there are a lot of different ways of enhancing the weak domain contrast in the magnetic sample. Additionally, there is no special treatment needed for the sample to be observed under Kerr effect microscope. Coating of the sample is allowed and sometimes this is done to enhance the MOKE signal using dielectric coating [34]. The sample can be cooled in cryostats or heated using optical heating stages therefore the temperature effects of the magnetic sample can be observed. Applying physical stress to the sample is possible while doing the observation, therefore making possible to study the stress effect on magnetic domains. The Kerr microscope can be changed easily to study the in-plane or out-of–plane magnetisation components of the sample. Investigation of the magnetic domains on the sample is done directly while applying magnetic field to the sample and domain wall motion can be observed using this method effectively.

2.2 Other methods

In addition to magneto-optical Kerr microscopy, there are other methods of observing magnetic domains. Nowadays, with the plenty of existing microscopic probes with the capability of imaging magnetic domains in very small magnetic structures such as Lorentz microscopy [35], electron holography [35, 36] and also scanning electron microscopy with polarisation axis [37]. Although they are capable of detecting magnetism in a very small sample (up to nano-scale), but due to their limitation of applying and freely modifying magnetic field inside an electron microscope, hence studies of magnetism for the samples are limited. Other example is the Transmission Electron microscopy (TEM), which is known to have a smaller field of view than the Kerr microscope. However for other microscopes that do not utilize the electron microscope such as magnetic force microscopy, spin-polarised tunnel microscopy [38] and other resonant technique [39], there are also other limiting factors that restrain their capability to observe magnetism such as the in situ preparation requirement for the spin-polarised tunnel microscopy. Alternatively, there are other high advance magnetometry techniques that have been developed and are capable of observing magnetism in nano-scale magnetic samples for example Hall-probe technique and nano Superconducting Quantum Interference Devices (SQUID) [40]. Despite the advantages, unfortunately these techniques need the fabrication of specialized sample, meaning they are not compatible with other general samples and sample shapes. In general, a technique which is very flexible, versatile, non-destructive to the sample and capable to detect magnetisation in small structures remains as the most desired method of study. Besides having all the desired criteria, MOKE is the least expensive method of study available compared to the other techniques mentioned earlier.

2.3 Magneto-optical Kerr effect

Kerr effect is an effect when a linearly polarised light reflects from a magnetic sample, its polarisation axis becomes rotated and at the same time, it is elliptically rotated. It was first reported by John Kerr in 1877 [41], but similar effect was first

discovered by Faraday in 1845 [42] where he found out that the plane of polarisation of light transmitted through a magnetic sample was rotated. The angle of rotation of polarisation observed for both effects depend on the strength of the magnetisation of the surface of the sample and the magnetisation orientation of the sample surface with respect to the plane of light incidence. This influence of the magnetisation orientation can be described by the different magnetisation geometries of Kerr effect.

The rotation effect of MOKE can be described generally in the form of dielectric tensor which account for the effect of magnetic medium. The dielectric law is given as:

$$\boldsymbol{D} = \boldsymbol{\varepsilon E}\,. \qquad \text{Equation 2.1}$$

In Equation 2.1, $\boldsymbol{\varepsilon}$ is the dielectric permittivity tensor which connects the electric field vector $\boldsymbol{E}$ of the plane of light wave along with $\boldsymbol{D}$, the induced electrical displacement vector. The generalized dielectric permittivity tensor is given in [43] in the form of:

$$\boldsymbol{\varepsilon} = \varepsilon \begin{bmatrix} 1 & -iQ_v m_3 & iQ_v m_2 \\ iQ_v m_3 & 1 & -iQ_v m_1 \\ -iQ_v m_2 & iQ_v m_1 & 1 \end{bmatrix} \begin{bmatrix} B_1 m_1^2 & B_2 m_2 m_2 & B_2 m_1 m_3 \\ B_2 m_1 m_2 & B_1 m_2^2 & B_2 m_2 m_3 \\ B_2 m_1 m_3 & B_2 m_2 m_3 & B_1 m_3^2 \end{bmatrix}, \qquad \text{Equation 2.2}$$

where Q_v is the Voigt constant in which it is material dependent that describes the magneto-optical rotation of the plane of polarisation of light, in this case the reflection in the Kerr effect. This Voigt term is a complex material parameter that is to the first order proportional to the magnetisation of the sample. B_1 and B_2 are constants describing the Voigt effect and m_i are the components of the unit vector of magnetisation along the cubic axis. Q_v, B_1 and B_2 are very complex and are not well known for the majority of materials, but the real parts of these constants are the most dominant. By using the term in Equation 2.1 the dielectric law can be generalised as shown in [44]:

$$\boldsymbol{D} = \varepsilon(\boldsymbol{E} + iQ_v \boldsymbol{m} \times \boldsymbol{E}). \qquad \text{Equation 2.3}$$

In Equation 2.2, ε is the dielectric permittivity tensor, vector $\boldsymbol{D}$ represents the secondary light amplitude which is produced by the magneto-optic interaction between $\boldsymbol{E}$ and the magnetisation vector $\boldsymbol{m}$ in the sample. From Equation 2.3, the cross product proves the gyroelectric nature of the Kerr effect with its symmetry which can be explained using the Lorentz force ($\boldsymbol{m} \times \boldsymbol{E}$) theory**.** In general, what being observed in MOKE is the magneto-optic response of the medium which is in the form of change in the polarisation of the incident light. This change is made of two types, the change of the in-phase component of the reflected light causing rotational change in the plane of polarisation of the incident light and the out-of-phase change which cause the elliptical change to the polarisation of incident light.

2.4 Geometries of Kerr effect

There are three different geometries of MOKE where their differences are relative to the plane of light incidence. The three different geometries of MOKE are shown in Figure 2.1 which consists of the polar MOKE, longitudinal MOKE and transverse MOKE.

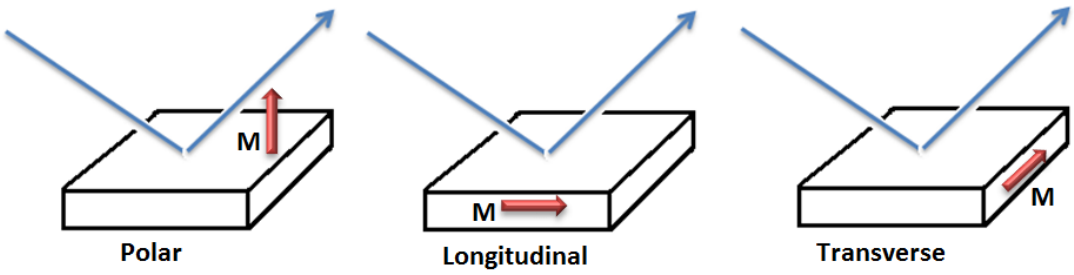

Figure 2.1: Schematic to show the three different magnetisation orientations (a) longitudinal, (b) transverse and (c) polar orientations the Kerr effect can be observed.

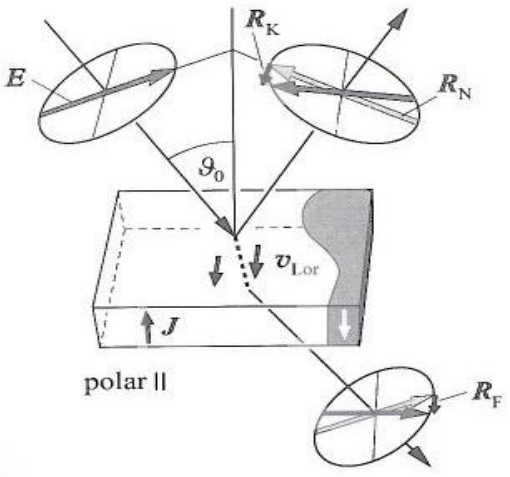

Figure 2.2: Diagram of the polar MOKE showing the magnetisation direction and the Lorentz movement direction, $\boldsymbol{v_{Lor}}$ which gives the Kerr effect in reflection and Faraday Effect in transmission [43].

In polar MOKE, the linearly polarised light induces electrons to oscillate parallel to its plane of polarisation, which in this case it is the plane of electric field $\boldsymbol{E}$. From Figure 2.2, $\boldsymbol{R_N}$ is the regularly reflected light where it is polarised in the same plane as the incident light. A small vibration is induced by the Lorentz force in the direction perpendicular to the primary motion and to the magnetisation direction. This secondary motion is proportional to the Lorentz movement ($-\boldsymbol{m} \times \boldsymbol{E}$) (similar to the second term in Equation 2.3), generates the Kerr amplitude $\boldsymbol{R_k}$ for reflection. Therefore the difference in angle between $\boldsymbol{R_N}$ and $\boldsymbol{R_K}$ resulted in the magnetisation-dependent polarisation rotation. Polar effect is strongest at normal incidence (θ=0°).

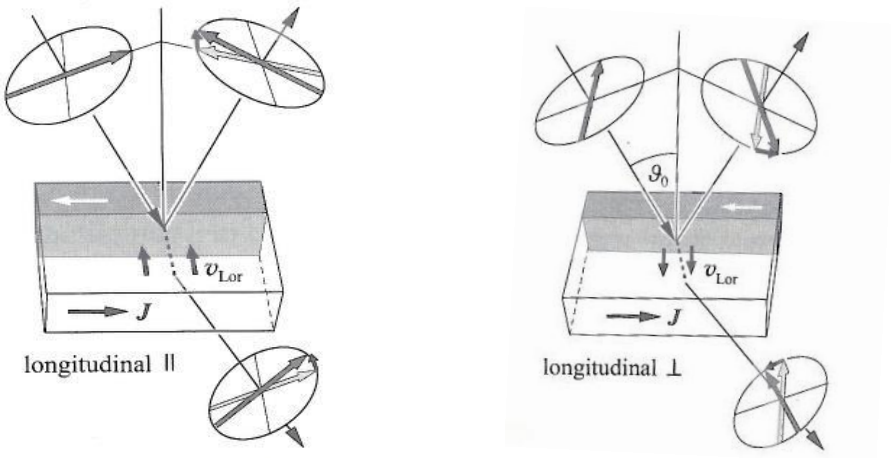

Figure 2.3: Schematic of parallel and perpendicular plane of the longitudinal geometry relative to the plane polarisation of the incident light [43].

For longitudinal geometry, the magnetisation direction of the sample is parallel to the plane of light incidence. The longitudinal effect induces rotational change to the plane of polarisation for both parallel polarisation and perpendicular polarisation plane of incident light. From Figure 2.3, the Lorentz motions in the two different polarisation of the plane of incidence are opposite to each other giving rise to opposite rotational direction of the resulting Kerr amplitude. Longitudinal effect disappears for normal light incidence (θ =0°) as the Lorentz force either vanishes or points along the beam.

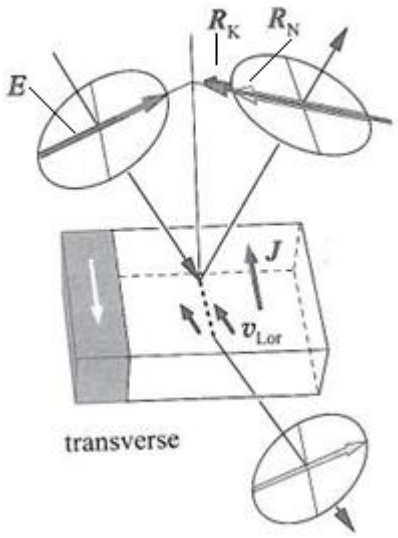

Figure 2.4: Sketch of the transverse MOKE with the Lorentz movement [43].

Transverse MOKE occurs when the magnetisation direction is perpendicular to the plane of light incidence. As shown in the

Figure 2.4, the transverse effect cause amplitude change to the reflected light but the polarisation direction of the Kerr amplitude is the same as that of the regularly reflected light. Thus, it will produce little contrast in the resulting image as there will also be noise in the form of intensity change from the light source which can affect the transverse MOKE signal. Yet the transverse MOKE can be used for measuring function [45]. Similar to the longitudinal MOKE, the transverse effect is eliminated in normal light incidence to the sample surface.

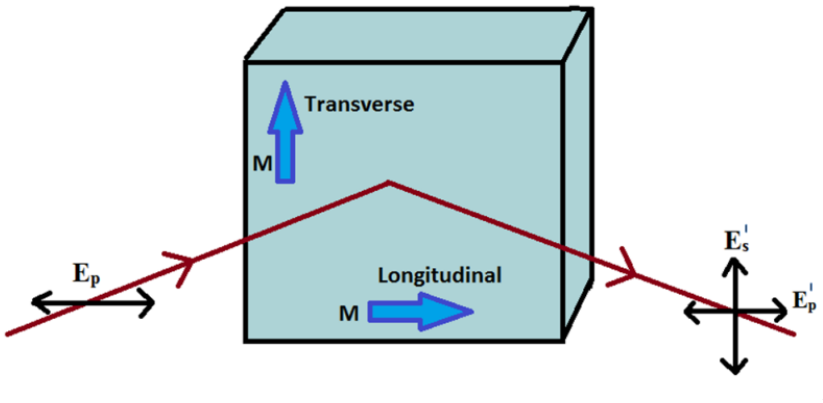

Figure 2.5: Schematic diagram showing the superpositions of the *p*-polarised light (*P*-light) and *s*-polarised light (*S*-light) of the incident light.

The explanation for longitudinal and transverse Kerr effect above can be simplified by using the Kerr Fresnel reflection coefficient that has been obtained by applying Maxwell boundary conditions at surface films [46]. Referring to Figure 2.5 which shows the superposition of the *p*-polarised and *s*-polarised light that is incident to the surface and then gets reflected, the coefficients for transverse as given in [47] are given by Equation 2.4, 2.5 and 2.6 and written as:

$$r_{pp}^{t} = \left(\frac{n\beta - \beta'}{n\beta + \beta}\right)\left(1 + \frac{k_2 sin2\theta}{n^2(n^2 cos^2\theta - 1) + sin^2\theta}\right) \quad \text{Equation 2.4}$$

$$r_{ss}^{t} = \frac{\beta - n\beta'}{\beta + n\beta'}, \quad \text{Equation 2.5}$$

$$r_{ps}^{t} = r_{sp}^{t} = 0\,. \quad \text{Equation 2.6}$$

And the Fresnel reflection coefficients for the longitudinal Kerr effect [47] are:

$$r_{pp}^{l} = \frac{n\beta - \beta'}{n\beta + \beta'}, \quad \text{Equation 2.7}$$

$$r_{pp}^{l} = \frac{\beta - n\beta'}{\beta + n\beta'} \quad \text{Equation 2.8}$$

$$r_{ps}^{l} = r_{sp}^{l} = \frac{\gamma_s \beta k_2}{(n\beta + \beta')(\beta + n\beta')}, \quad \text{Equation 2.9}$$

where θ is the angle of incidence measured from the normal of the sample, n is the index of refraction of the film, $k_2 = in^2Q$ is the off diagonal element of the relative permittivity tensor, $\gamma_s = sin\theta$, $\beta = cos\theta$, and $\beta' = \left(1 - \frac{sin^2\theta}{n^2}\right)^{\frac{1}{2}}$. Referring to the transverse coefficients above, the transverse Kerr effect does not cause rotational change to the plane of polarisation of the incident light given that the off-diagonal terms which cause the rotational are equal to zero as shown in Equation 2.6. The only parameter that is magnetisation-dependent is the reflection coefficient relating the incident and reflected *p*-polarised light given in Equation 2.4. Therefore there will only be light intensity change for transverse effect as explained previously. Further, for longitudinal Kerr effect, the coefficients confirm that there is a magnetic-dependent rotational change to the plane polarisation of the incident light by the derived off-diagonal terms in Equation 2.9.

The light intensity, after passing through the analyser can be presented using the normal polarisation equation in the form of:

$$I = I_0 cos^2\,\theta\,, \quad \text{Equation 2.10}$$

where I_0 is the intensity of the reflected light before entering the analyser and θ is the angle between the plane polarisation of I_0 and the plane of analyser. Hence, the maximum intensity change can be calculated by differentiating Equation 2.10, which gives:

$$\frac{dI}{d\theta} = 2I_0 cos\theta sin\theta. \quad \text{Equation 2.11}$$

The resulted maximum change of intensity is at $\theta = 45^{o}$, but this is the maximum change of the whole reflected light. A change of the light intensity caused by the Kerr rotation which is relative to the whole reflected light is needed and shown as:

$$\Delta I = \frac{dI}{d\theta}\frac{\alpha_r}{I}. \quad \text{Equation 2.12}$$

Hence, the relative change due to the Kerr rotation is:

$$\frac{\Delta I}{I} = \frac{2I_0 cos\theta sin\theta}{I_0 cos^2\,\theta}\alpha_r\,, \qquad \text{Equation 2.13}$$

and I_{Kerr} is:

$$I_{Kerr} = \frac{\Delta I}{I} = 2\alpha_r tan\,\theta, \qquad \text{Equation 2.14}$$

where ΔI is the light intensity change due to Kerr rotation and α_r is the angle of Kerr rotation**.** Furthermore, by plotting the graph in Figure 2.6 relating the Kerr sensitivity and the analyser setting as shown in Equation 2.14, it is demonstrated that the I_{Kerr} is very high in the regions of analyser setting near to 90°.

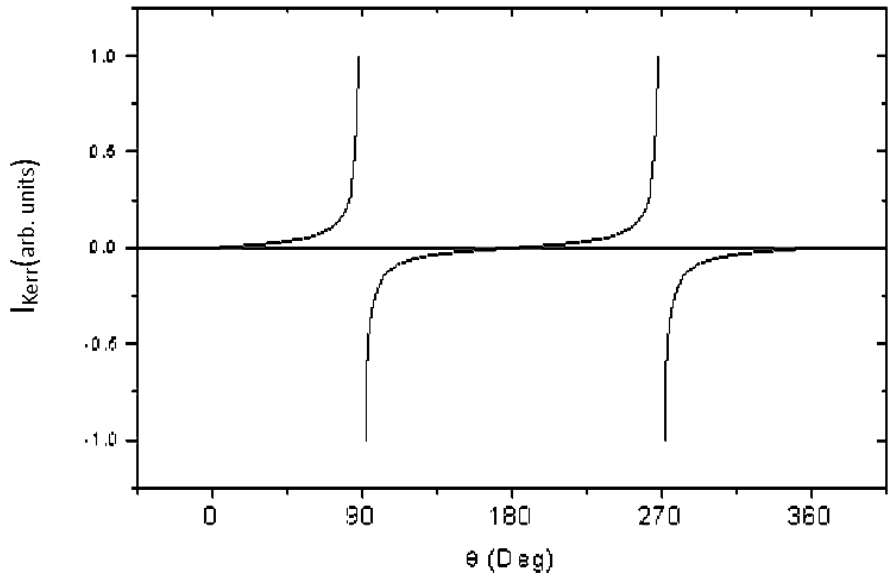

Figure 2.6: Graph of Kerr sensitivity versus the angle between the plane polarisation of the polariser and the plane of analyser.

As seen in Figure 2.6, the high slope of the graph at 90° means a slight change in the angle of analyser can cause a high gain or loss of Kerr sensitivity. Experimentally, it is hard to pinpoint the analyser angle by a few degrees. Moreover, there is always a degree of imperfection to the polarized light [48] because of the polarizers being less than 100% efficient and to the range of angles of incidence in the focused beam on the sample. Therefore it is impossible to set the analyser exactly at 0° cross with the polariser to completely remove the background light for a very high Kerr sensitivity.

In order to get high Kerr sensitivity, it cannot always be achieved by setting the analyser and the polariser to be perfectly crossed or trying to remove much of the background light through extinction as discussed above. If the resulted image is too dark, the signal processed electronically will be too small. The resulted dark image captured by the camera will contain less Kerr signal as it is very dim, therefore larger analyser angle α_r is more favoured. Similarly, for a high Kerr sensitivity microscope setup, the signal-to-noise ratio, r_{SN} of the Kerr microscope needs to be high enough so that the weak Kerr signal is not lost in the noise. Kerr signal is very weak but it can be enhanced electronically on condition that the r_{SN} is large enough.

2.5 Wide-field Kerr microscope set up

The first part of the experiment was to build a 'homemade' wide-field Kerr microscope on an optical table. The wide-field Kerr microscope built is based on the commercial reflected light wide-field microscope as shown in Figure 2.7. The setup is shown in Figure 2.8. The optics used are all strain free as this is mandatory for polarization microscopy.

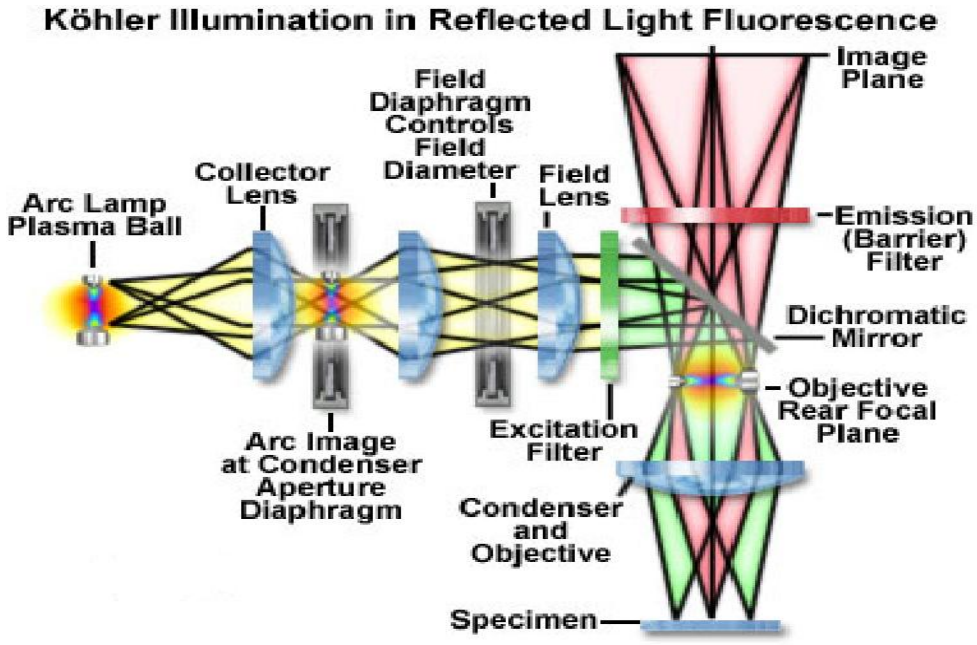

Figure 2.7: The regular setup of commercial wide-field reflected light microscope with Kohler illumination [49].

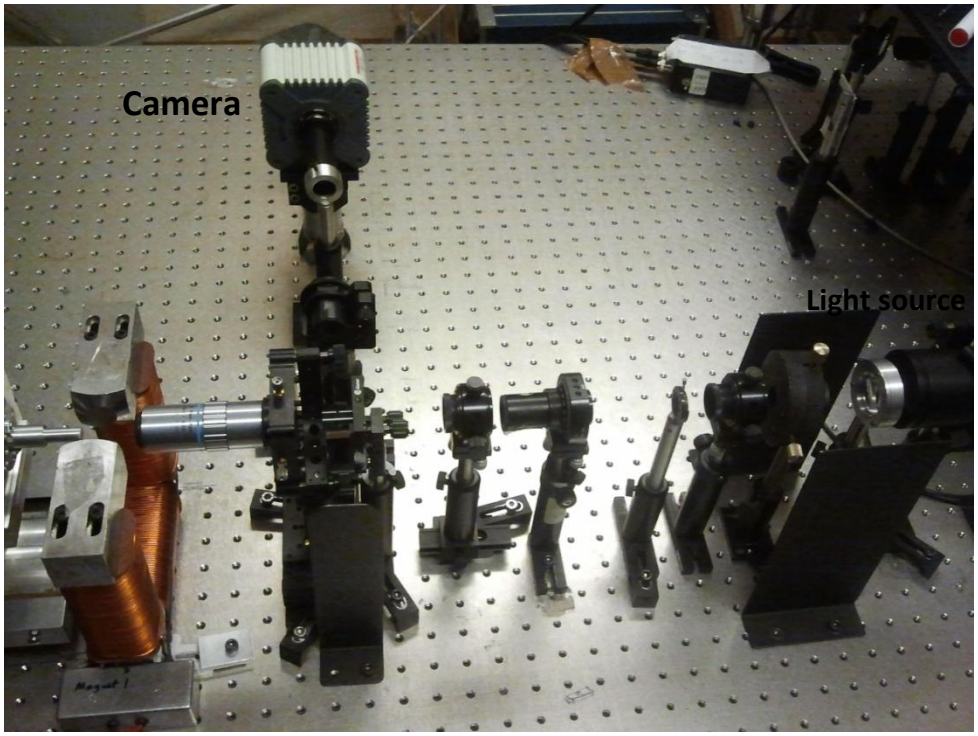

Figure 2.8: Top view of the Kerr microscope setup.

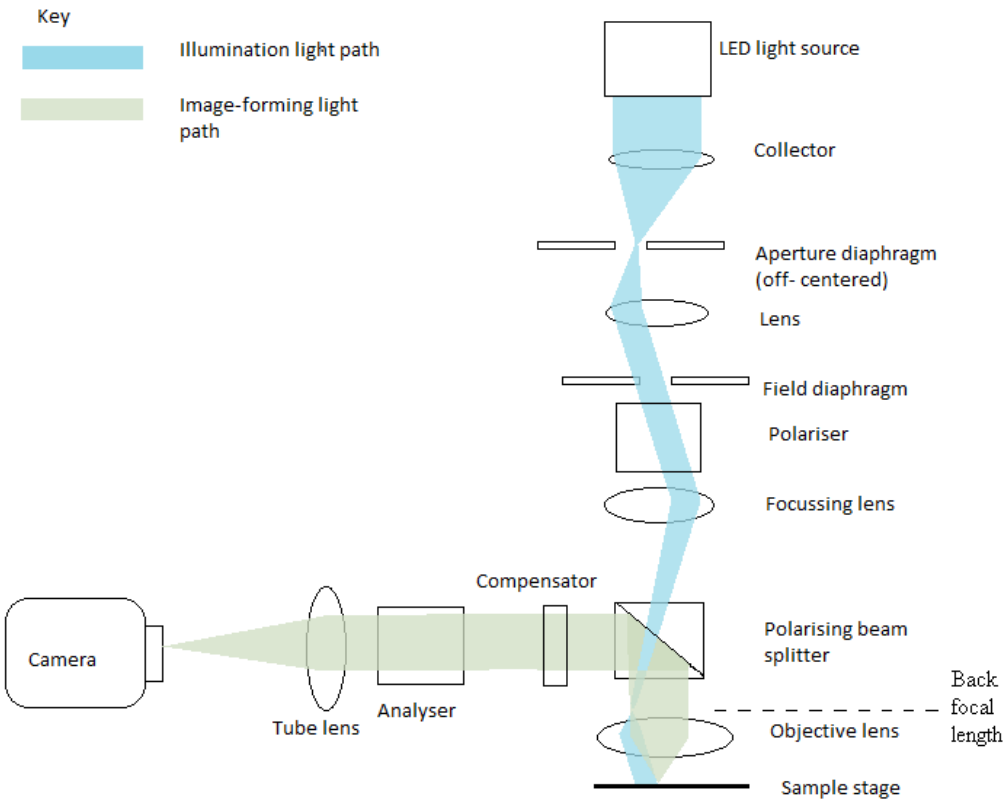

Figure 2.9: The 'homemade' wide-field Kerr microscopy set up showing the two

different light paths, the illumination light path and the image-forming light path. The setup is the off-centered aperture sensitivity setup for longitudinal Kerr effect and also transverse Kerr effect.

2.6 Optics

As shown on Figure 2.9 the light source used for this setup is a LED lamp. When the light passes through the collector, it focuses the light to the iris of the aperture diaphragm. Aperture diaphragm is crucial in Kerr microscopy setup and will be looked at later in this chapter. The second lens in the setup change the light rays to infinity as it passes through the field diaphragm and the polariser. Then, the focussing lens will focus the light to the back focal plane of the objective lens. Further, the light is collimated by the objective lens to illuminate the magnetic sample on the sample stage.

The light illuminated on the sample is then reflected along with the changes due to the Kerr effect. The changes involved are polarisation, intensity change and phase change depending on the type of MOKE that occurs in the magnetic sample. Subsequently, the reflected light is reflected by the polarising beamsplitter away from the illumination light path. Thus, the light together with the changes goes through the compensator and analyser. The compensator used in the setup is a quarter wave plates. The analyser translates the plane polarisation change into an intensity change and the image is focused on the CCD chip by the tube lens. It can be noticed from Figure 2.9 the light is projected to infinity as it passes through the polariser, compensator and analyser. In account for this is that at infinity light rays, these optic components will not distort the image.

Before the polarising beamsplitter was used, the original reflector that had been used was a non-polarising beamsplitter. This beamsplitter has a splitting ratio of 50:50, resulting in a 50% light loss from the light source and an additional 50% lost after it is reflected to the compensator. As explained earlier, signal-to noise ratio depends on the illumination intensity, therefore this loss is unbearable as this will lead to an image with a very low Kerr signal and very dim (dark image). Kerr effect is already

too small to be observed, this large amount of light loss will further reduce the Kerr sensitivity of the setup. The reflector was later replaced with polarising beam splitter with transmission percentage of 90% P-polarised light and reflectance percentage of 99.5% of S-polarised light. Therefore the plane of incident light is a P-polarised light and thus, the plane of polariser needs to be aligned along the P-polarised light as required for Kerr microscopy.

The polarizer and analyser are set to nearly perpendicularly crossed with each other for the polar and longitudinal Kerr effect. This is to get the maximum extinction in one of the domain for an optimum magnetic domain contrast. For transverse effect, a 'longitudinal with transverse sensitivity' setup is applied and a way to do this will be explained later in this chapter. This setup utilizes a Glan-Taylor prism as the polariser and analyser. This polarizer has an extinction ratio of greater than 10^5:1, which is high enough for the observation of the weak Kerr effect.

2.7 Sources of noise

For the overall setup for Kerr microscopy the sources of noise that are taken into account are;

1) The shot created by the quantized nature of light, this is an inevitable noise which varies with the photon number in the image.

2) Electronic noise that is independent of the image intensity caused by the instruments and the detection electronics.

3) Fluctuation of the light source and in the sample which are proportional to the image intensity.

4) Stability noise of the overall microscope setup, especially when observing nano-sized samples where nanometre movement of the sample during the experiment can cause significant noise contribution in the image and even worse, the loss of signal.

As the shot noise is the unavoidable noise, it preferable to take into consideration the relative signal-to-noise ratio caused by this noise. Also this can be used to represent the overall noise in the microscopy setup. A method in [43] show; that the shot noise can be written as $N_{shot} = \sqrt{\frac{1}{2}F_{inc}(I_1+I_2)}$, where F_{inc} is the number of photons illuminating the sample, is the intensity of dark magnetic domain in the image and is the intensity of the other magnetic domains in the image. Again, simplified from [43], the optimum value of the analyser angle α_r ($\alpha_r = 90 + \alpha_s$) in relation to the signal-to-noise ratio and the optimum signal-to-ratio are:

$$tan\ \alpha_{opt}^{SN} = \sqrt[4]{\frac{A_K^2 + I_B}{A_N^2 + I_B}} \qquad \text{Equation 2.15}$$

$$r_{SN}^{Opt} = \frac{4A_K A_N \sqrt{F_{inc}}}{\sqrt{A_N^2 + I_B} + \sqrt{A_K^2 + I_B}} \approx 4A_K\sqrt{F_{inc}}\ . \qquad \text{Equation 2.16}$$

Here, A_N is the regular amplitude, A_K is the magneto optical amplitude (effective Kerr amplitude) and I_B is the background intensity. This proves that the maximum value of signal-to-noise ratio depends on the Kerr amplitude and the number of illuminating photon, however it is not determined by the Kerr rotation. Therefore, it is important to maximize the illumination intensity on the sample and the use of a powerful light source is important. Further addition of the electronic noise, fluctuation noise and other noise reduces the signal-to-noise ratio but overall it does not affect the essential feature of the explanation above.

2.8 Light source

The light source used was a royal blue LED light with a wavelength of 455 nm. The first light source used was a tungsten lamp, although it can produce very bright light, it gets heated up very quickly and there was no ventilated lamp house with fan heat sinks to remove the heat generated by this bulb. And, in comparison to the LED, the tungsten lamp gives out a less stable light source. At some point, a laser was utilized into the setup as a light source but laser illumination introduces speckles and

hotspots in the image. To reduce the formation of hotspots and speckles on the image, a rotating plastic disc was inserted in front of the laser source. The speed of the spinning plastic disc can be controlled throughout the experiment. In part a of Figure 2.10, the result shows an image with hotspots and speckles that are highly prevalence even after placing the rotating plastic disc into the setup. There are a number of ways to reduce the speckles and hotspots [50] however the LED was chosen for its well-defined output image and optimized thermal management. The difference in the quality of image produced by using laser and LED as a light source can be seen in Figure 2.10.

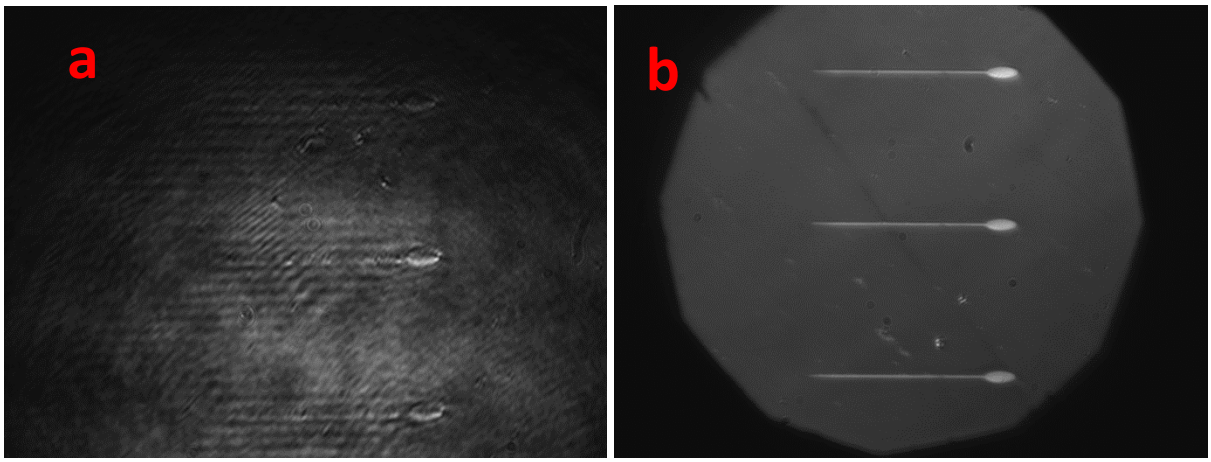

Figure 2.10: Images of nanowires with width around 380 nm with nucleation pad under the microscope using two different light sources, the figure on the left shows the image produced by using laser as the light source (a) with the introduction of rotating plastic disk whereas the image on the resulted from using LED (b).

2.9 Kohler illumination and field diaphragm

Wide-field microscopes use the Kohler illumination technique. Kohler illumination is a method of sample illumination where the purpose is to obtain an incredibly even illumination of the sample and that the image of the illumination source (light source) is not present in the resulting image. In most modern microscopes, the Kohler illumination is used and no construction of this technique is needed. But, to build a 'homemade' microscope, this part is very vital as uniform illumination is needed for Kerr effect observation. To achieve Kohler illumination, the light emitted from the

light source must be focussed at the back focal plane of the objective lens, as a result the illuminating light rays goes to infinity, thus giving Kohler illumination to the surface sample. From Figure 2.9 the focussing lens is used to focus the light rays at the back focal length of the objective lens and at the same time it imaged the field diaphragm is imaged on the sample surface. This can be seen on part b of Figure 2.10 where the field diaphragm image can be seen on the resulted image and it limits the area of the sample to be illuminated by blocking the undesired light rays.

In conclusion, the position of the back focal plane of the objective lens is required for Kohler illumination. However, the position of the back focal length is classified information as different companies have their own 'secret ingredients' in their commercial microscope which remain unrevealed. An attempt was made to try to contact the main office of the manufacturer of the objective lens asking them for the distance value of the back focal length, however they denied my request as the back focal length value of their objective lens is classified. Therefore the value was calculated manually and this is illustrated by the ray diagram in Figure 2.11 . The focussing lens with a known focal length is moved forward and backward while the illuminated light is confirmed for infinity rays. To check for infinity rays, the size of the light spot must be the same size near the output of the objective lens and at another distance about two feet away from the objective lens. After this is accomplished, the focussing lens is locked at that position and as shown in Figure 2.11 the field diaphragm is fixed at the back focal length of the focussing lens to image the field diaphragm into the resulting image. The resulted back focal length value is so different that it is not equal to the calculated value using the back focal length equation ($BFD = 2F \times NA$) which is caused by the unique internal design of the microscope.

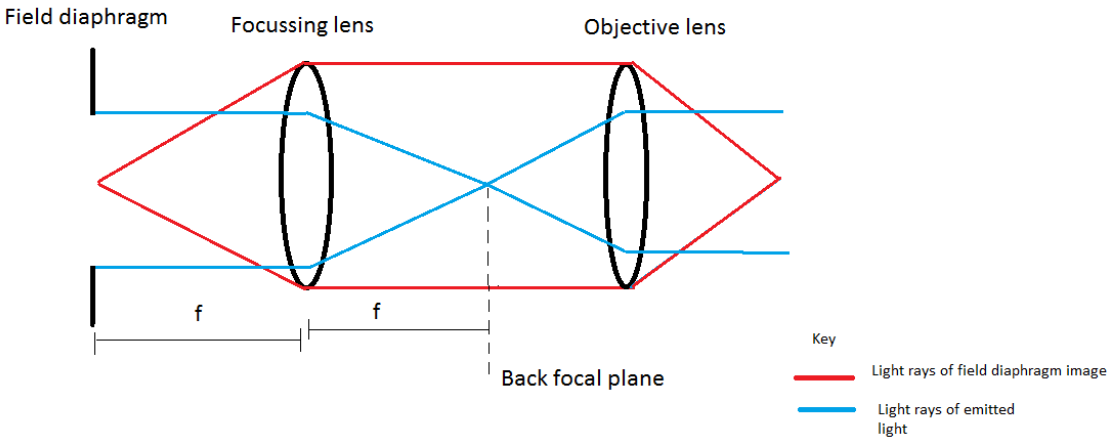

Figure 2.11: Schematic diagram demonstrating the two different light rays from the field diaphragm. Red lines represent the light rays of the image of the field diaphragm while the blue lines represent the emitted light passing through the field diaphragm.

The field diaphragm can effectively control the field of illumination on the sample. As seen in Figure 2.12, the field diaphragm can be decreased until only the area of the zigzag nanowire is iluminated. This is very useful to avoid illumination in unwanted area such as the electrical pad connecting the sample for current induced observation where the electrical pad can cause unnecessary high intensity illumination on the resulting image.

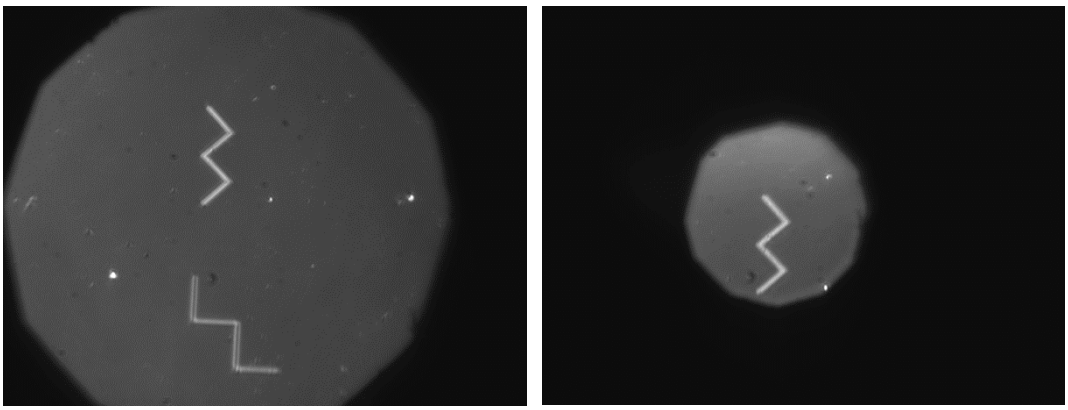

Figure 2.12: Two captured images at different field diaphragm sizes where the right part showing the image with smaller field diaphragm. The width of the zigzag wire is around 841 nm.

2.10 Aperture diaphragm

The aperture diaphragm is one of the most crucial parts of the Kerr microscope. In normal microscope, the aperture diaphragm controls the optical resolution and intensity of illumination. The smaller the size of the aperture diaphragm, the higher the resolution of the image but the lower the intensity of illumination will be and increasing the aperture size will reduce the resolution but the illumination intensity will increase. The same effects also occur in Kerr microscopy with some additional effects. The additional effects are; closing and opening the aperture diaphragm change the angle of incidence, and moving the aperture diaphragm off-centered depending on which direction it moves to, determines the type of MOKE the microscope will observe. Therefore, the aperture determines the angle of incidence with the largest angel of incidence being limited by the numerical aperture of the objective lens. This shows the fundamental role of the aperture diaphragm in the Kerr microscope setup.

In Figure 2.13, this image is the conoscopic image of the microscope. In a modern microscope this can be seen by replacing the eyepiece with the auxiliary telescope or with the build in Bertrand lens. But in the setup, additional lens is inserted in front of the camera that has the right focal length to focus the back focal plane of the objective lens to the camera. The cross-shaped image describes the extinction zone when the polariser and the analyser are crossed (crossed polarised) for maximum extinction in the sample image. The cross-shaped is also known as the Maltese cross and the main reason for this event to happen is because light bundle converge in wide-field microscopy. Light rays that is not in the cross part cannot be terminated because they are reflected in an elliptical and rotated polarised condition. Therefore for maximum contrast results, the aperture stop is positioned in the dark (cross) area as shown in Figure 2.13.

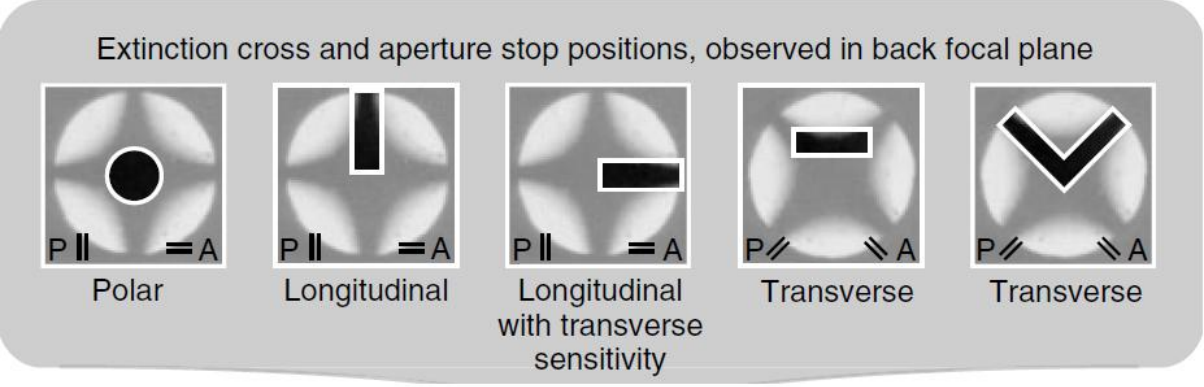

Figure 2.13: Diagram showing the extinction cross and aperture stop positions for different MOKE geometry [44].

Further if the aperture iris is set to the centre, the whole alignment is straight and the angle of incidence will be zero degree because this results in an illumination cone that hits the sample cone vertically. Due to symmetry, Kerr amplitudes resulting from the in plane magnetisation (longitudinal and transverse MOKE) components cancel each other and the net Kerr amplitude will be zero. Consequently, in this setup, the sensitivity is to the out-of-plane magnetisation in which as described earlier is for the polar Kerr effect. The aperture location for polar Kerr effect is shown in Figure 2.13 and is as illustrated to be in the middle and round shape. An off-centered aperture iris gives an obliquely incident bundle of rays which is required for longitudinal and transverse Kerr sensitivity. The aperture locations for the longitudinal and transverse Kerr effects are shown in Figure 2.13. In the setup, an adjustable square slit is used. For longitudinal Kerr sensitivity, a square aperture with adjustable size is used. Because the longitudinal Kerr effect can only be detected in oblique incidence, the square aperture is positioned off-centered at one arm of the maltese-cross. This gives an incident light with its plane parallel to the magnetisation direction of the sample. Let's simply call the transverse magnetisation in this same sample to be the 'transverse axis' of the sample. Therefore, changing the aperture stop to the 'longitudinal with transverse sensitivity' will change the plane of the incident light to be parallel to the magnetisation direction along the 'transverse axis' of the same sample. This gives the 'transverse axis' a magnetic contrast by using longitudinal Kerr effect. It is better to use the longitudinal with transverse sensitivity setup for observing transverse effect than the other two transverse setups in Figure 2.13, for

obvious reason that the longitudinal effect gives a stronger magnetic domain contrast than transverse effect, as the transverse effect has higher noise because the Kerr signal is from the light intensity change where much of the light source noise goes in with the result. Whereas in longitudinal sensitivity the polariser and analyser are cross-polarised near to extinction where most of the unwanted signal is removed. In addition to that, this saves time to focus mainly on the longitudinal setup to observe both the longitudinal and transverse Kerr effect.

2.11 Compensator

As explained before, the plane of polarisation of the reflected light is not just rotated but also elliptically polarised. If the elliptical polarisation is more dominant than the linear polarisation of the reflected light, a compensator is used to remove the elliptical component and convert it into a linear wave. In this setup, a quarter-wave plate is used as the compensator in which it must be aligned along the analyser plane. However, using a compensator is not always necessary because oblique incidence (light incident not at normal incident) can create a phase shifts by rotating the polariser away from symmetry positions. Meaning, the polariser and the analyser can be adjusted simultaneously until the desired contrast and brightness is achieved. In the setup, it utilizes the use of longitudinal Kerr effect even for the transverse effect, the longitudinal with transverse sensitivity is used as explained above. The elliptical polarisation effect was observed experimentally using the Kerr microscopy in the longitudinal sensitivity mode. Two MOKE experiments were done where one of them was done with the compensator removed. And the result used was a nanowire aligned along the longitudinal plane of the microscope. Result on Figure 2.14 shows the two hysteresis loops that confirm the elliptical polarisation to be very low in the setup and the use of compensator is not compulsory.

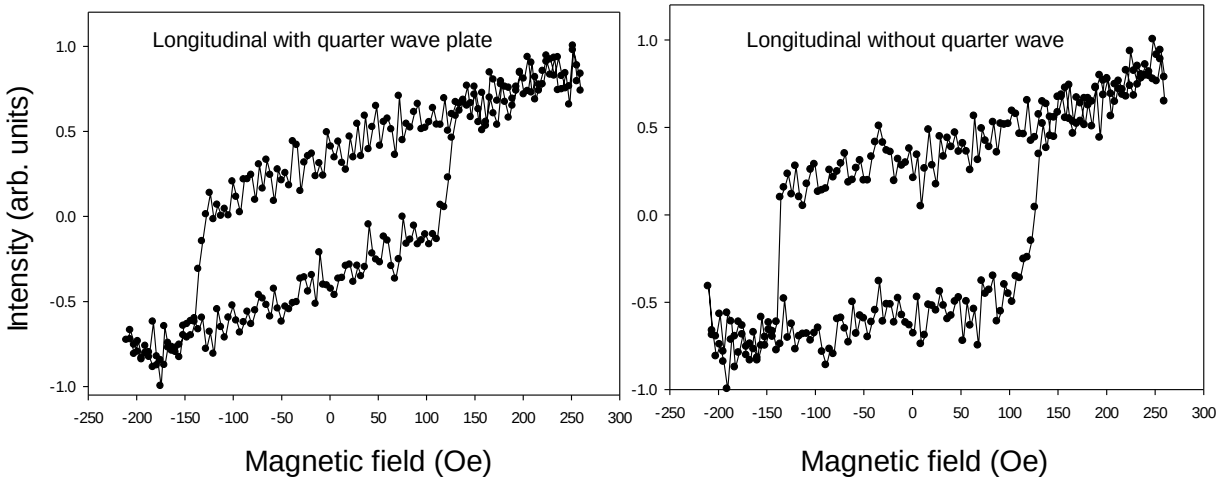

Figure 2.14: Two hysteresis loops from two experiments where one of them is done with a compensator in the set up and the other one without the compensator in the setup. The loops are results from averaging of 10 loops from sample of around 350 nm width nanowire.

2.12 Lateral Resolution and magnification of objective lens

Resolution is a very important parameter when doing microscopy given that domain structures have different sizes down to nanometres. Because resolution is limited due to the diffraction limit, the sample to be observed must not be smaller than the resolution of the microscope. The lateral resolution in a microscope is dependent on the value of the numerical aperture of the objective lens and it is written as:

$$NA = n\ sin\ \alpha\ , \qquad \text{Equation 2.17}$$

where n is the refractive index of the medium and α is the half angle of the cone of light from the specimen received by the objective. The minimum distance between two points that can be resolved is given by:

$$D = \frac{c\lambda}{NA}, \qquad \text{Equation 2.18}$$

where λ is the wavelength of the light source. In the microscope setup, the NA of the objective lens is 0.55 and by assuming c to be 0.61 and together with the light

source wavelength of 455 nm, the resolution of the microscope is 505 nm. 505nm is the resolution limit of the setup, but a smaller sample up to 245 nm can also be observed and its Kerr contrast can be made visible by doing digital contrast enhancement. For sample smaller than the resolution limit, the sample image is broadened and this can be seen in the results chapter of this thesis.

The total magnification of microscope may be controlled by the tube lens but this does not change the resolution of the microscope. In other words, the image field of the microscope can be increased or decreased by changing the magnification.

The equation for magnification is given as;

$$\mathrm{M} = \frac{f_2}{f_1}, \qquad \text{Equation 2.19}$$

where f_2 is the focal length of the tube lens and f_1 is the focal length of the objective lens. The tube lens focal length is 200mm and the objective lens focal length is 4 giving a 50 times magnification (50x). For nano sized samples, increasing the magnification can increase the amount of pixel surface area on the detector chip of the camera. But during the experiment study, only the tube lens can be changed because there is not much option for the objective lens choice. A 500 mm tube lens was used giving the magnification 125x. The resulted image was significantly enlarged. With this new change in the setup, a MOKE experiment was done on the nanowire, but unfortunately the resulted hysteresis loop was very noisy with very small Kerr effect signal. It is deduced that, due to the very long focal length (500 mm) of the tube lens giving an extra 300 mm distance between the tube length and the camera have caused a lot of light loss. Further, the significantly enlarged image also cause the loss of image brightness at the camera compared to the non-enlarged image.

Due to the fact that this is a ‘homemade’ microscope, it is extremely important to make sure the optimum performance of the objective lens. Due to the specific design of the objective lens, the distance l between the tube lens and the objective lens is limited to a certain value. This is to ensure the optimum optical performance of the objective lens and to avoid formation of shadows in the resulting image. The equation of l is given as:

$$l = (\emptyset_2 + \emptyset_1)\frac{f_2}{\emptyset}$$ Equation 2.20

$$\emptyset_1 = 2f_1 \times NA\,,$$ Equation 2.21

where $\emptyset_1$ is the objective exit pupil diameter, $\emptyset_2$ is the effective diameter of tube lens and $\emptyset$ is the image field diameter. These values are shown in
Figure 2.15. With f_1=4mm, NA =0.55, the value of $\emptyset_1$ is 4.4mm. Inserting the value of $\emptyset_1$ into Equation 1.20, together with $\emptyset_2 = 24$ mm, f_2=200 and $\emptyset$= 24 mm give $l =$ 163 mm. Therefore the value of l must be 163mm or lower for optimum performance of the objective lens

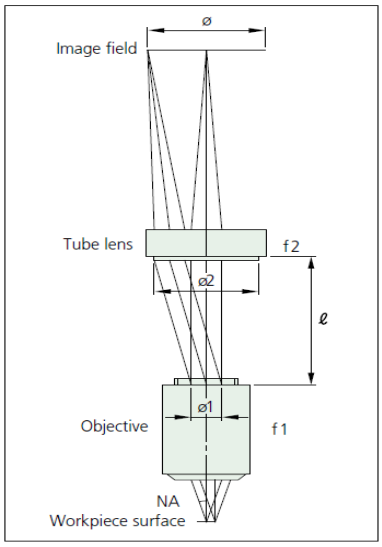

Figure 2.15: Schematic diagram showing the placement of objective lens and the tube lens [51].

2.13 Camera

The camera used in the setup is the Hamamatsu ORCA-ER camera. This camera has a LabVIEW driver available, allowing possible control of the camera from LabVIEW programme. It is a huge advantage as the whole project involves the use of LabVIEW programme to control the whole system. But because the camera is an old version, it was hard to find the compatible frame grabber and the right computer with the right PCI slots for connecting the frame grabber. As the experiment involves taking thousands of images at short time, a high spec computer with 64-bit window

was needed. The whole processes of ordering, testing and returning the frame grabber and the computer took more than two months.

Different camera has different spectral response characteristic and it is described using the graph of quantum efficiency versus the wavelength of the light source.

Figure 2.16 shows the spectral response characteristic of the ORCA-ER camera for different light wavelength. Thus, one can see that the quantum efficiency of the light source (with wavelength of 455 nm as described before) for the setup is around 68% which is close to the optimum quantum efficiency of the camera at 72%. To detect the weak Kerr effect, a high spectral response of the camera is needed and this camera has that requirement.

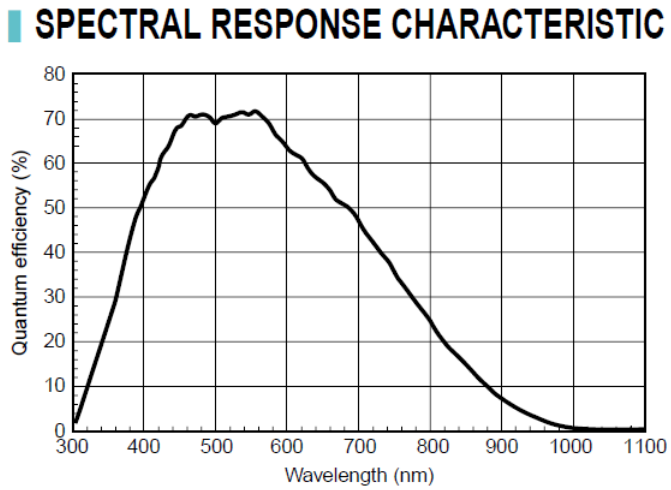

Figure 2.16: Spectral response graph of the ORCA-ER camera [52].

2.14 Electromagnet

The electromagnet used in the setup has a limit of 2.8k Oe with poles separation of 27 mm and shown in Figure 2.17. The magnetic field strength is controlled by a LabVIEW programme in a computer. A 1000 W amplifier is used as the power supply for the electromagnet. The voltage output signal from the LabVIEW is connected to the amplifier, the amplifier then converts this signal into the required power to the electromagnet and the electromagnet will produce the required magnetic field. The amplifier has bi-polar ability, therefore it can produce positive and negative field

depending on the sign of the output voltage signal from the computer. The magnet has magnetic field of around 1700 Oe and -1700 Oe the value of amplifier input voltage and magnetic field are directly proportional to each other. Therefore, between these values, any change in the amplifier input value will cause a directly proportional change in the magnetic field strength. This will be very useful when developing LabVIEW programme for the setup and it will be explained later in this chapter.

Figure 2.17: Shows the value of the electromagnet where the distance in between poles is around 27 mm.

2.15 Programming

For the project, three LabVIEW programmes were created with three different roles. A significant amount of time was spent to create these programmes to make sure they functioned well. All the programmes were created to be as user-friendly as possible making them very flexible and easy to understand for further development. The programmes are:

1) Programme for taking a sets of pictures with known magnetic field for each picture.
2) Programme to analyse the sets of images and to do digital contrast enhancement.
3) Programme to extract the hysteresis loop for the magneto-optical magnetometry.

The programmes were divided into three because the work will involve taking thousands of pictures and saving them in the hard drive and reading thousands of images at a fast rate. Therefore with different purpose of each programme, it is better to separate them into three to avoid the computer from crashing as this had happened previously.

2.15.1 Taking sets of images in loop.

The programme is divided into two parts. The first part which is on the left side of Figure 2.18 is to set the camera setting for different functions available in it. The functions that come with the camera are the exposure time setting, binning functions and more. After the desired setting is chosen, the image can be viewed in video form before starting the experiment. It is extremely important to avoid saturated pixels in the image because the area with saturated pixels will have no data at all. This can be seen when there is a bright white spot in the image when viewing the sample before the experiment. It can also be checked using the saturation option tool in the camera software provided with the camera.

The second part (right side of Figure 2.18 of the programme is to take the sets of images in a user-specified manner. The sets of images are taken in loops which cycle around the magnetic values chosen by the user. These sets of images are taken in a routine similar to data points taken to get a hysteresis loop of the magnetic sample. Before starting the experiment, the magnetic field number and the number of repetition for the experiment is typed into the 'magnetic field' box and the 'loops' box respectively. These boxes can be seen on Figure 2.18. The user is allowed to choose the step size of the magnetic field strength between two images in sequence. This can be controlled by changing the number of images to take in each cycle and this value is inserted in the 'number of image' box. For example, choosing a magnetic field of 200 Oe and image number of 100 means an image is taken in every 2 Oe change in the magnetic field ($\frac{200Oe}{100} = 2\ \mathrm{Oe}$). In the experiment the magnetic field will go from 200 Oe to -200 Oe and then back to 200 Oe in the fashion of a hysteresis loop, while taking picture in every 2 Oe step of the magnetic field and

then this is repeated again with the amount of times stated in the ‘loops box’. The whole images are coded with numbers with respect to the magnetic field strength and the sequence of loops. All the images will be saved into the hard drive of the computer. Due to the large amount of high definition images being saved in a small amount of time, usually at range of tenth thousands of images, a high spec computer is used with very high RAM and hard drive.

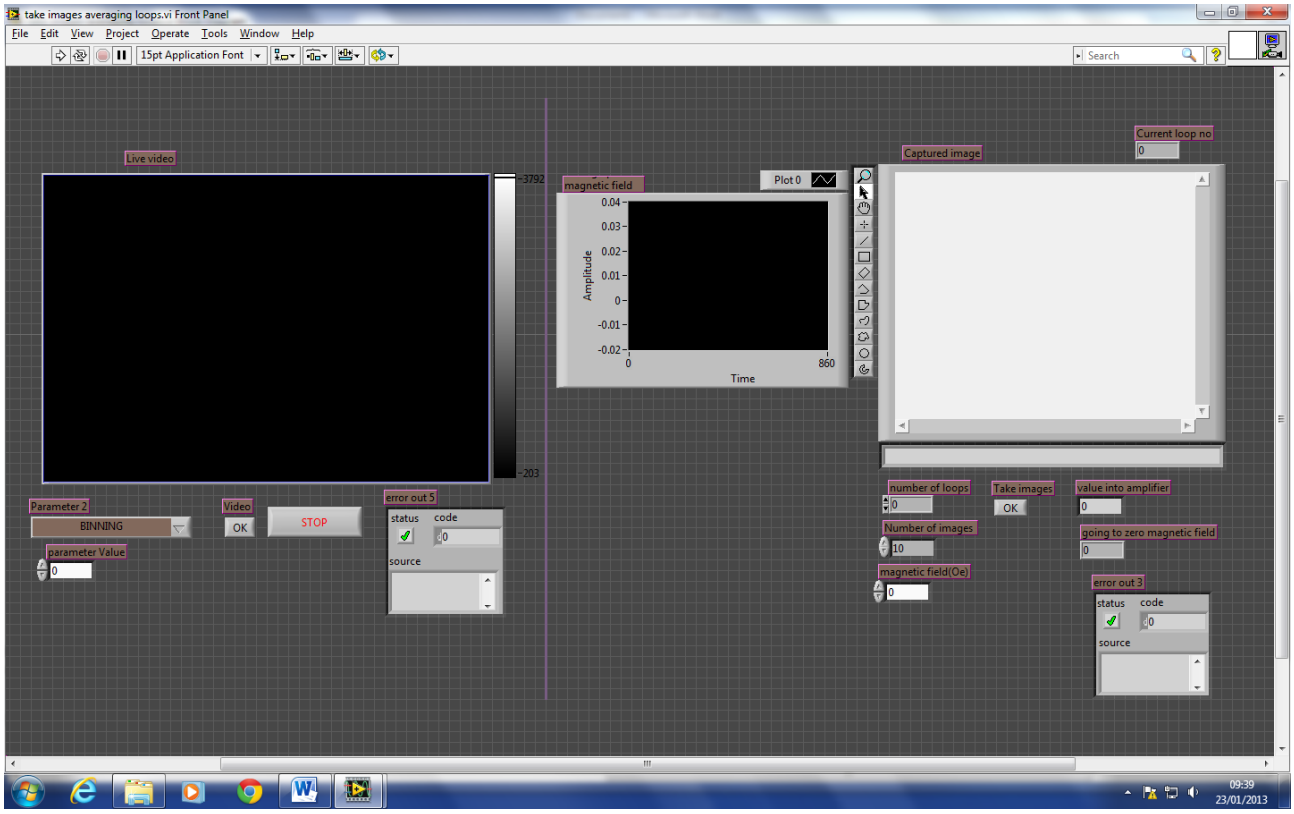

Figure 2.18: Screenshot image of the front panel of the LabVIEW programme for taking sets of images in loops.

2.15.2 Magneto-optical magnetometry

The second programme is developed to extract the hysteresis loop of the magnetic sample from the images. From Figure 2.19, the bottom part of the programme is used to choose the area of the sample for the extraction of hysteresis loops. Before running the programme, the values of the magnetic fields, number of images and

loops number must be inserted in the respective box shown on Figure 2.19. These are the same values that were inserted when taking the pictures. After clicking the run button, the user will be asked about the location of the folder where the images were saved in and then the user will be requested to choose the area of the sample for hysteresis loop extraction as shown in the screenshot of Figure 2.20. The single hysteresis loop is shown in the right side of the programme as shown in Figure 2.19. On Figure 2.19 the graph in the middle of the programme shows the time-wave graph the Kerr signal from a cycle of one loop. The main purpose is to see how large is the fluctuations of the light source, the electronic drift and other noises. Fluctuation from the light source and the camera are represented by the formation of slope (not the high jump caused by magnetisation reversal) in the time wave graph of the Kerr signal. The final value for every single loop is saved in a folder and will be averaged by the top part of the programme shown on Figure 2.21.

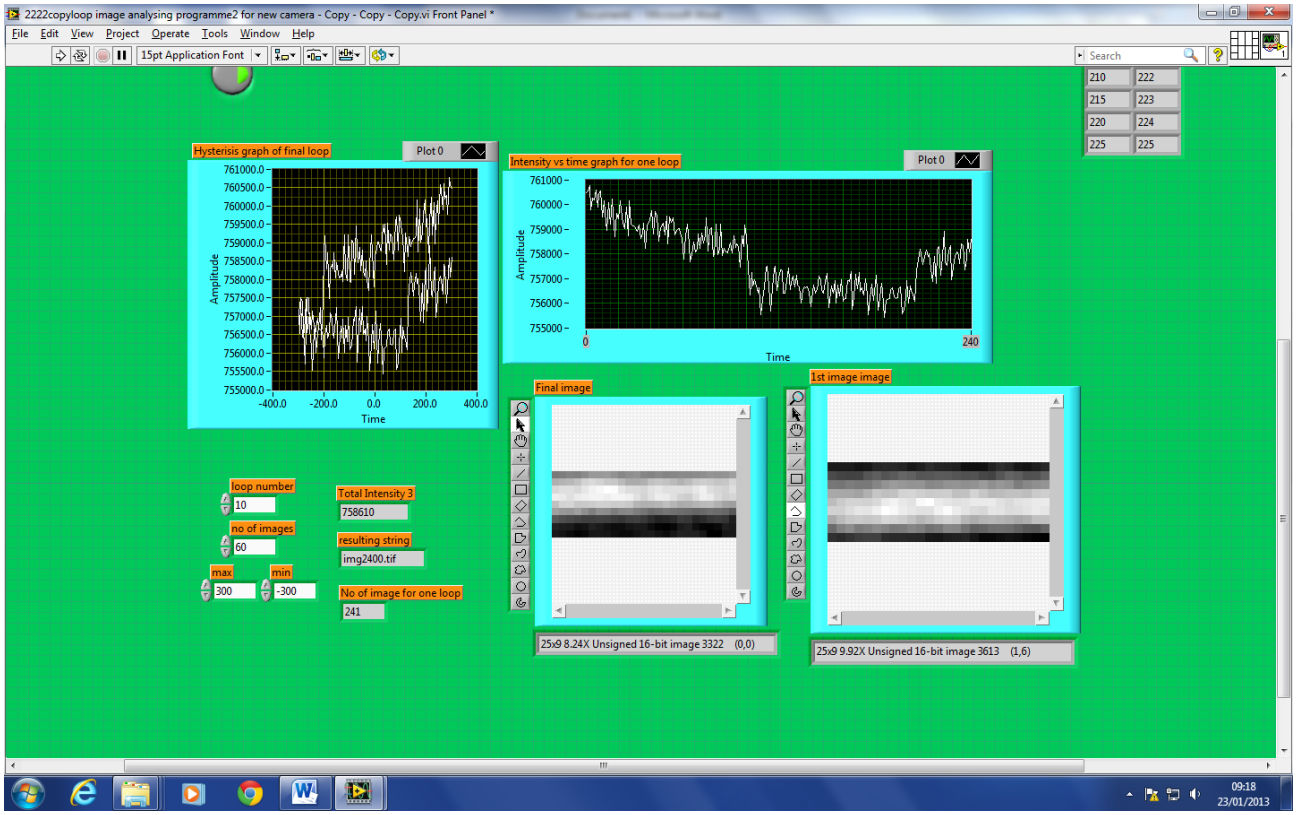

Figure 2.19: Screenshot of the frontpanel at the bottom part of the LabVIEW for the hysteresis loops extraction at different part of the sample.

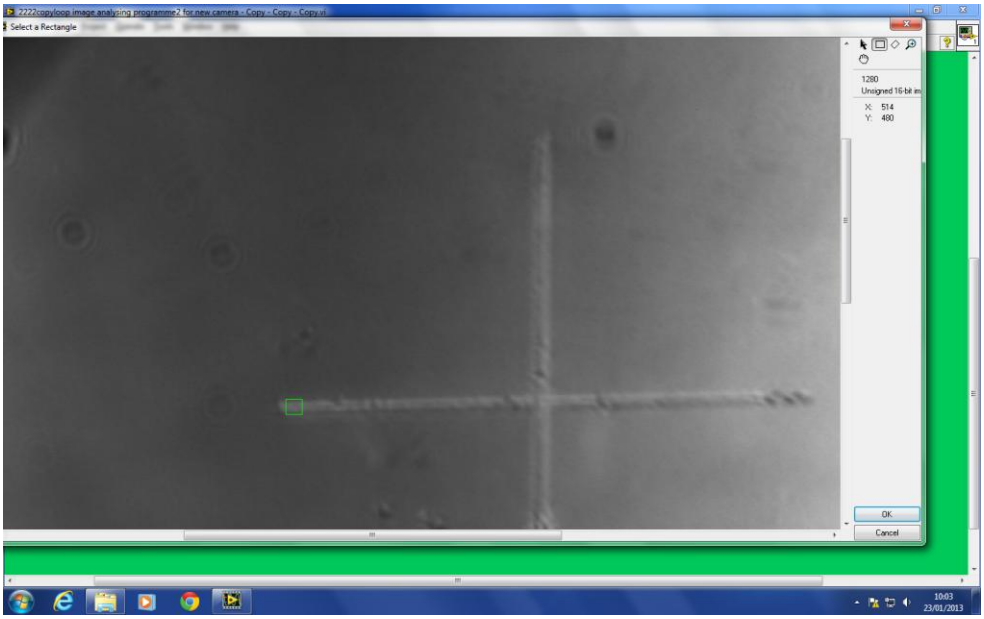

Figure 2.20: Screenshot picture when choosing the area of the sample for hysteresis loop observation. The small green square represents the desired area for hysteresis loop examination.

The top part of the LabVIEW is for the loop averaging in which it reads the values in the saved file and then averages them. The averaged hysteresis loop is shown in the graph at the centre of the front panel shown in screenshot of Figure 2.21. The user can easily improve the result by using the functions built in the programme. The functions include slope correction, changing values of averaging point and normalisation. User can change the values in these functions panel and view the improvement. A limitless trial can be done to improve the result until the desired result is achieved. Normalisation is mandatory when doing experiment in which the repetition is high. It is because of the electronic 'drift' when the experiment is running for a long time causes large difference in the light intensity values for different loops making it impossible to average them. Therefore, normalisation helps to put all the hysteresis loops to be in range with each other for averaging. The 2d arrays on the right side of Figure 2.21 show the coded number of image with respect to the magnetic field strength. This is very important as a reference of the magnetic field strength when doing the magnetic domains extraction from the image at different magnetic field strength and will be described in the next section.

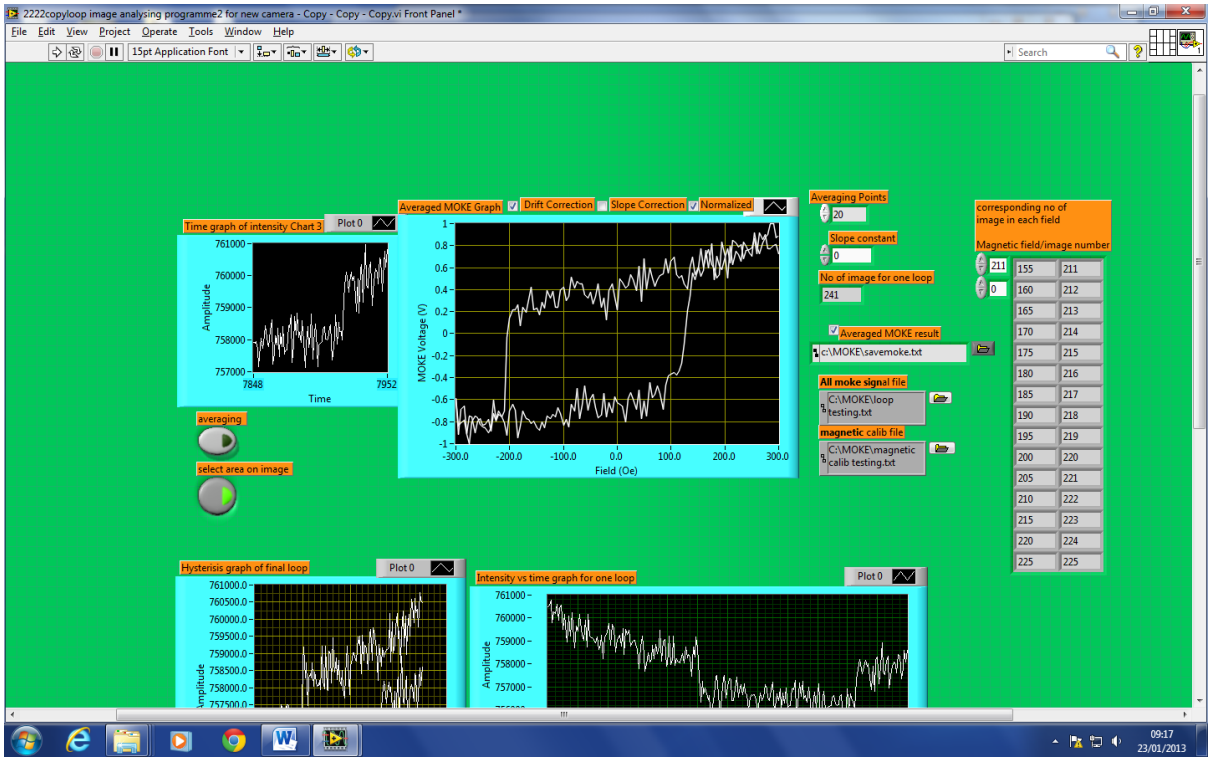

Figure 2.21: Screenshot picture of the top part of the LabVIEW for averaging of the extracted hysteresis loops.

2.15.3 Analyse sets of images and digital contrast enhancement

This is the part where the image processing is done. This program is developed purely to get the magnetic domains contrast by doing image subtraction and averaging over the repeated loops. The contrast is produced by doing subtraction of image from a certain field subtracted with the image at a different magnetic field. The user has the option to choose images for subtraction in any desired magnetic field at the range of field chosen when taking the images.

Before running the programme, as usual the value of loops repetition and number of images must be inserted into the programme. As shown on the left part of Figure 2.22, the two image numbers to be subtracted must also be inserted. These image numbers are the implied image numbers relative to the magnetic fields during the experiment and the relation of these numbers can be referred to the 2d array on Figure 2.22 and this is described in the magneto-optical magnetometry section.

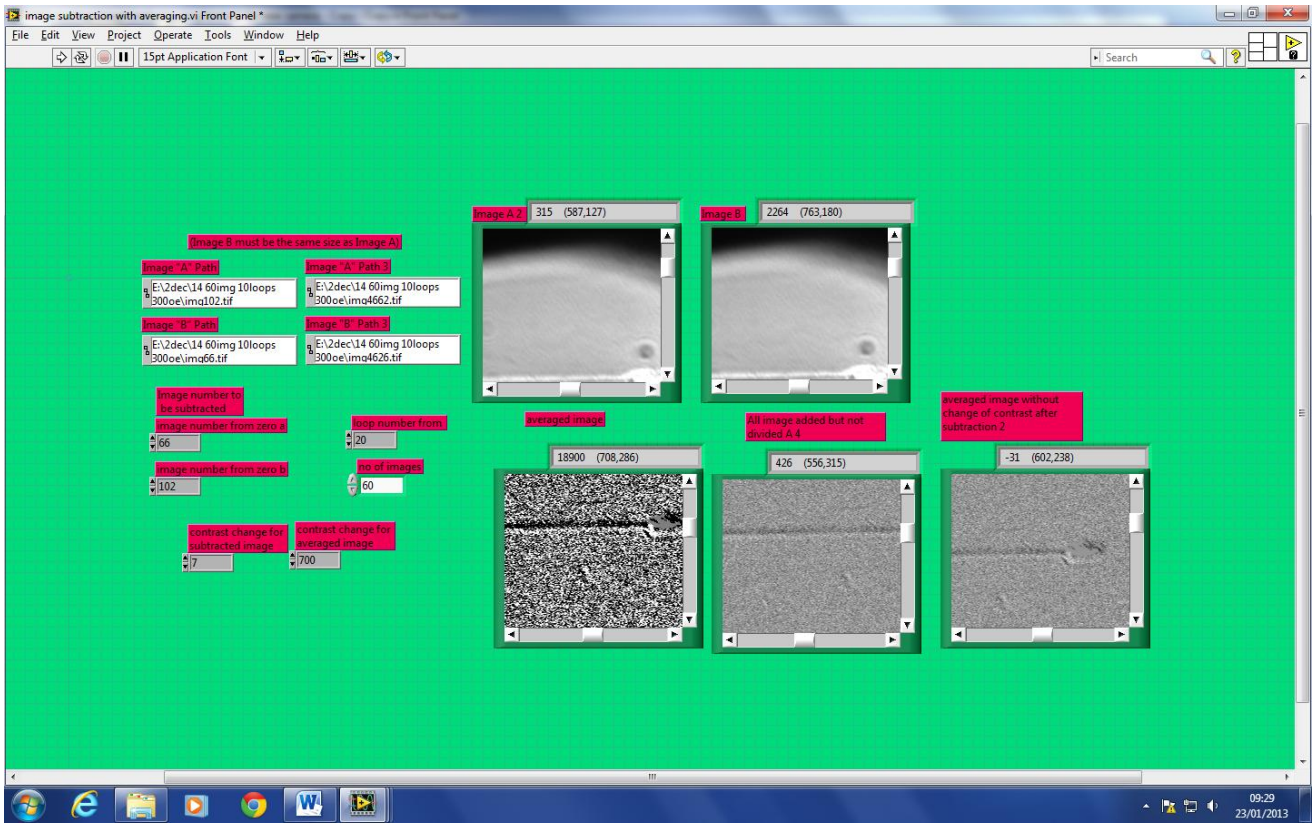

Figure 2.22: Screenshot of the front panel LabVIEW for magnetic domains contrast observation.

The most powerful element of this programme is the ability to get the averaged magnetic domains image from the number of repetition chosen by the user. Depending on the hard drive and RAM of the computer, a repetition of over 30 times can be performed for magnetic fields range of ±300 Oe with 5 Oe step size. Therefore a single loop will contain 7500 images with all the magnetic contrast of the sample can be observed between magnetic field range of +300 Oe and -300 Oe for every 5 Oe step in this range. The magnetic contrast can be seen by doing subtraction, for example subtracting at -80 Oe and at saturation field of the sample at 300 Oe. After clicking run, the programme will automatically subtract images at -80 Oe and 300 Oe for all loops and the subtracted image for all 30 loops will then be averaged giving a very high magnetic contrast image. On the other hand, if the user only want to see differences in magnetic domains between the saturations of 300 Oe and -300 Oe. Thus the capturing of images is set to range of ±300 Oe with the step set to 600 Oe. As a result only two images in one loop and the loop repetition can be

set to over 2000 times which will give an extremely high magnetic contrast in the image.

Additionally, the programme is provided with the contrast change function. Contrast change is the direct multiplication of the pixel in the image with the contrast constant value inserted into the ‘contrast change’ boxes at the front panel of the programme as shown in Figure 2.22. There are two types of contrast change that are available in the programme; contrast change to the subtracted image and contrast change to the two images before they are being subtracted. Both of the change give different contrast enhancement, therefore these two values can be changed simultaneously until the desired magnetic contrast image is achieved. An image window is set to specifically display the change of image contrast that is caused by the contrast change before subtraction. With this function, the user can inspect any improvement, if any, in the resulted magnetic domains contrast whether it is caused by the contrast change before subtraction or by the contrast change after subtraction.

2.16 Sample preparation

Most of the samples fabricated for this project are patterned nanowires made of nickel iron (NiFe). All the samples were fabricated by Xuefeng Hu who is a PhD at the University of York. The samples for the project were fabricated using the lift-off technique, combined with optical or e-beam lithography. This method is capable of fabricating small patterned structures of up to 10 nm. This method allows any kind of shapes fabrication and produces a sample with constant thickness thoroughly. To fabricate the sample, a cleaned silicon substrate is coated with an electron beam resist. After coating, the desired pattern is drawn on the coated substrate using e-beam lithography. In e-beam lithography, an electron beam is focused on the desired area using magnetic lenses. The direction of the electron beam is controlled by an electrostatic field produced by a set of deflection plates. The electron beam will engrave the resit, as a result, a pattern will be exposed on the resist. Then, the material is deposited on the patterned substrate by thermal evaporation or sputtering. In the exposed area, the material will sit on the substrate and remain there, whereas the rest will be deposited on the resist. Next, the product is immersed

in acetone to remove the resists. Therefore only the material on the substrate stays. This process is called the lift-off. The quality of the deposited material is determined by the thermal evaporation or the sputtering process but other than that, it is a very flexible and useful technique for nano-scale pattern fabrication. A summary of this technique is explained using diagrams shown in Figure 2.23.

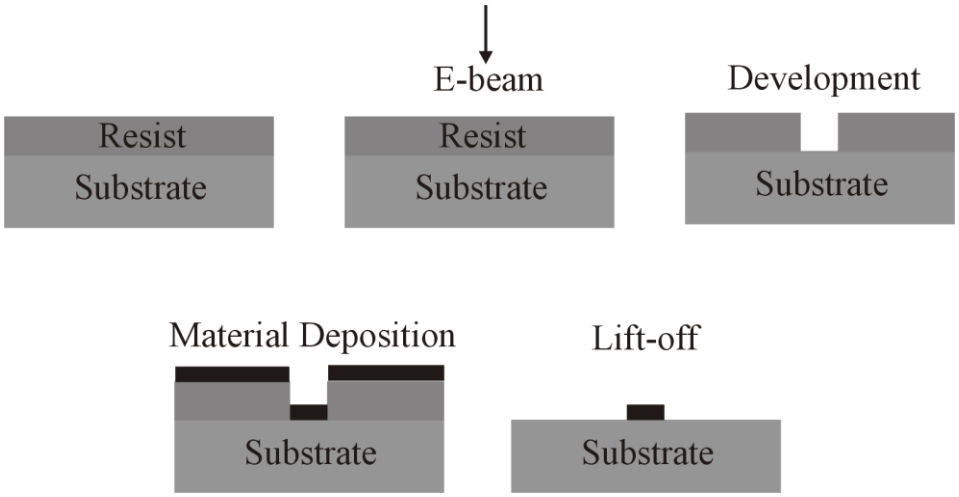

Figure 2.23: Summary diagrams of the lift-off technique, combined with optical or e-beam lithography technique for sample fabrication.

2.17 OOMMF Simulation

The simulation result was done also by Xuefeng Hu who is a Phd student at the University of York. To do the micromagnetic calculation and simulation, he used software known as Object Oriented Micro-Magnetics Framework (OOMMF) package. OOMMF is an open source software which was developed by M. J. Donahue and D. G. Porter from National Institute of Standards and Technology (NIST) [53].

For the field driven-dynamic magnetisation, the simulations use the Landau-Lifshitz-Gilbert (LLG) differential equation [54]:

$$\frac{d\boldsymbol{M}}{dt} = -\gamma\left(\boldsymbol{M} \times \boldsymbol{H}_{eff}\right) - \frac{\gamma\alpha}{M_s}\left(\boldsymbol{M}\left(\boldsymbol{M} \times \boldsymbol{H}_{eff}\right)\right), \qquad \text{Equation 2.22}$$

where γ is the LLG gyromagnetic ratio derived as:

$$\gamma = \frac{\mu_0 ge}{2m_e}, \qquad \text{Equation 2.23}$$

and $\boldsymbol{M}$ is the magnetization vector (A/m) per unit, $\boldsymbol{H}_{eff}$ is the effective field vector (A/m) which depend on energy of system E at Equation 2.24, α is the damping coefficient and M_s is the saturation magnetization (A/m), g is the Landé g factor, e is the charge of electron and m_e is the mass of electron.

Total energy of the system is:

$$E = E_{ex} + E_{demag} + E_a + E_{zeeman}. \qquad \text{Equation 2.24}$$

The exchange energy is:

$$E_{ex} = \int_v A\left(\nabla(\boldsymbol{M}/M_s)\right)^2 dV, \qquad \text{Equation 2.25}$$

where A is the exchange stiffness, and the anisotropy energy is:

$$E_a = K_1 sin^2\theta + K_2 sin^4\theta, \qquad \text{Equation 2.26}$$

where θ is the angle between the direction of magnetization and the symmetric axis.

The demagnetisation energy is:

$$E_{demag} = -\frac{1}{2}\mu_0(\boldsymbol{M}.\boldsymbol{H_d}) = -\frac{1}{2}\mu_0 M_s(\boldsymbol{m}.\boldsymbol{H_d}) = \frac{1}{2}\mu_0 M_s\left(\boldsymbol{m}.(\nabla\Phi_d(\boldsymbol{r}))\right) \qquad \text{Equation 2.27}$$

$$= \frac{\mu_0 M_s^2}{8\pi}\left[\int_V \frac{(\nabla.\boldsymbol{m}(\boldsymbol{r}'))(\boldsymbol{r}-\boldsymbol{r}')}{|\boldsymbol{r}-\boldsymbol{r}'|^3} d^3\boldsymbol{r}' + \int_S \frac{(\boldsymbol{m}(\boldsymbol{r}').\boldsymbol{n})(\boldsymbol{r}-\boldsymbol{r}')}{|\boldsymbol{r}-\boldsymbol{r}'|^{\boldsymbol{3}}} d^2\boldsymbol{r}'\right],$$

where $\boldsymbol{H_d}$ is the demagnetisation field vector, $\boldsymbol{n}$ is the unit vector normal to the surface and $\boldsymbol{r}$ is the relative displacement**.**

The Zeeman energy is:

$$E_{zeeman} = -\mu_0 \int_v \boldsymbol{M}.\boldsymbol{H}_{ext}\, dv \qquad \text{Equation 2.28}$$

The effective field is:

$$\boldsymbol{H}_{eff} = -\frac{1}{\mu_0}\frac{\partial E}{\partial \boldsymbol{M}}$$ Equation 2.29

In the Equation 2.23, the Land´e factor g is close to 2 for many ferromagnets, in particular the 3d series. Equation 2.22 can be divided into two parts where the first part is the procession term which means that it will let the magnetization ***M*** process around the field and no losses are included. And the second part is the damping term that dissipates energy and it is dimensionless. For physical materials, the value of α will be in the range of 0.004 to 0.15. But if it is a confined structure such as nanowires, α will be larger than the above value. This term is introduced phenomenologically in order to get the system to settle down into an equilibrium state instead of processing endlessly. The more intelligent ways of incorporating the damping into the model are still an active research topics and different ways can produce variety of magnetization procedures.

The OOMMF utilizes a LLG solver to relax the 3D spins on a 2D mesh of square cells. For certain geometry of samples, it will divide this geometry into a number of cells and the so-called mesh is shown in Figure 2.24. The magnetisations of each cell are the initial values which are given by users. Under a certain external magnetic field, according to these initial values, the system energy can be calculated by using formulas between Equation 2.24 and Equation 2.28. And using this value of the energy of the system and in addition to using FFT's (an efficient way for calculating the self-magnetostatic field caused by the long range order included from the magnetization of all other nodes in the mesh), the self-magnetostatic (demagnetic) field can be computed. By inserting the value of the energy of the system E into Equation 2.29 and substituting Equation 2.29 into the LLG equation (Equation 2.22), the value of the new magnetisation $\boldsymbol{M}_{new}$ can be acquired. The above procedure is repeated for many times to obtain the so-called equilibrium state of magnetisation under a certain cut-off condition ($|\boldsymbol{M} \times \boldsymbol{H}|/M_s \leq 10^{-5}$). Now we can consider that magnetisations of all the cells are stable under this external magnetic field. If the magnetic field is changed then the above calculation is repeated to get new equilibrium value.

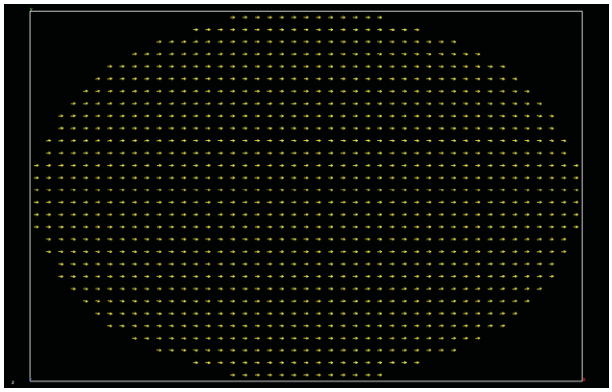

Figure 2.24: Mesh of simulation points for an elliptical sample.

Finally, there are key points to take into consideration:

(1) The cell size is very important to choose before performing simulation. Generally speaking, it should be smaller or close to the exchange length of the material. This is mentioned in section 1.6.

(2) The lateral condition of the geometry of the sample will affect the simulation. The cell shape chosen for the simulation is cube shape. Therefore if non regular shape such as circle, the simulation will produce wrong simulation results..

(3) Damping parameter is crucial that affect the simulation. If it is too small, the whole simulation will takes a very long time. Therefore choosing a value of around 0.5 will accelerate the calculation speed and simulated result will not be largely deviated from the actual process (real situation).

3. Results and discussions

3.1 Focused MOKE magnetometer result

It was necessary to understand the Kerr effect and its geometries experimentally before setting up the Kerr microscope. Therefore, experiments on Kerr effect were done using a focused MOKE magnetometer which was built by previous PhD student Serban [55] in the spintronic lab. The setup was built for longitudinal MOKE geometry and utilise a bridge detector to read signals from the light reflected from the magnetic sample. Two continuous nanowire samples with the width of 1000 nm and 400 nm were observed using the focused MOKE setup. During the experiments, the setup was improved by changing the area of the reflected light beam that can enter the detector. By making sure only the light beam that contains the wanted MOKE signal to come into the detector, the noise in the result was reduced. Although the setup was already capable of getting MOKE signal, but focussing on perfecting the alignment and also controlling the iris that eliminate the unwanted light beam to enter the detector help to increase the sensitivity of the setup to detect Kerr effect. From the result of the experiment, a single hysteresis loop of a continuous 400 nm wire have a signal to noise ratio of 3:1 which showed the very low noise of the improved setup. Figure 3.1 shows the hysteresis loops result for each wire in which each loop is an average of three loops. The signal-to-noise ratio of the 400 nm width nanowire was further increased to more than 4:1 by averaging three loops. This explains how important it is to do averaging for noise reduction and also knowing the properties of the light bundles of incident light and reflected light may help to improve the Kerr microscope setup.

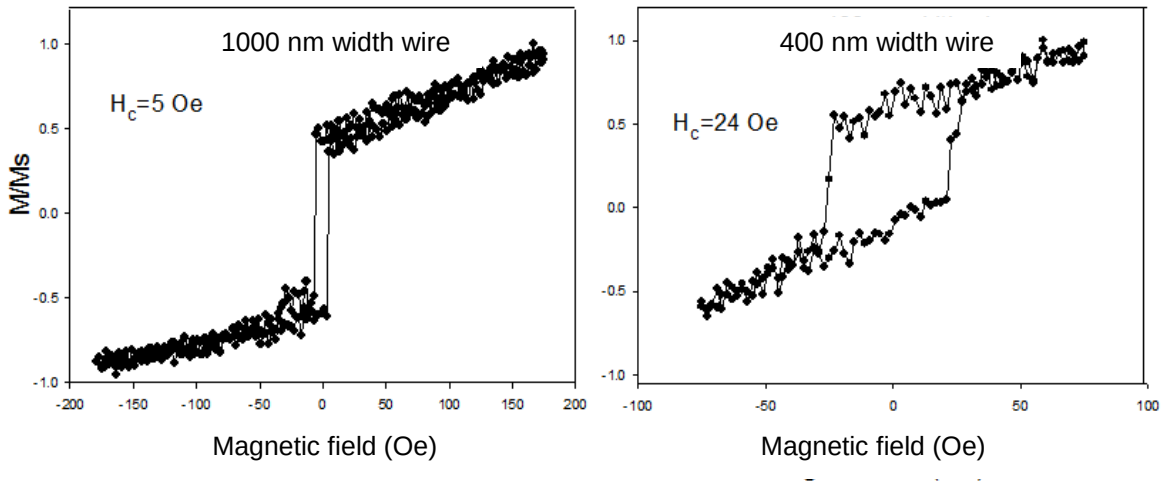

Figure 3.1: Hysteresis loops result from 1000 nm and 400 nm width nanowires using focused MOKE magnetometer. Each hysteresis loop is an average of 3 loops.

3.2 Result from nickel iron ($Ni_{80}Fe_{20}$) thin film

A NiFe thin film sample was used to test the Kerr microscope setup before doing experiments on nanostructures samples. This helps to confirm whether the setup is able to detect the Kerr effect or not. The microscope was set to longitudinal sensitivity mode and the thin film sample was oriented such that its easy axis is parallel to the longitudinal MOKE axis of the setup. As described before, 'mode' control was done by placing the aperture stop of the aperture diaphragm at the right position and this is explained in the experimental techniques part of this thesis. Given in Figure 3.2 is the result of single shot hysteresis loops of the thin film at different sizes of chosen area. It was explained in the experimental techniques chapter that the user is capable of choosing any area of any size in the field of view of the microscope for the extraction of hysteresis loop in the sample. From Figure 3.2, it clearly shows that increasing the region of interest (ROI) will increase the value of the detected Kerr signal. As predicted, larger area of samples will gives higher Kerr effect signal. In conclusion, results in Figure 3.2 confirm that the Kerr microscope is working well as well as capable of getting MOKE signal of up to an area of size 1x1 µm and smaller. The result is a single hysteresis loop data, by doing repetition and averaging of loops will help to improve the weak Kerr signal from

nanowires.

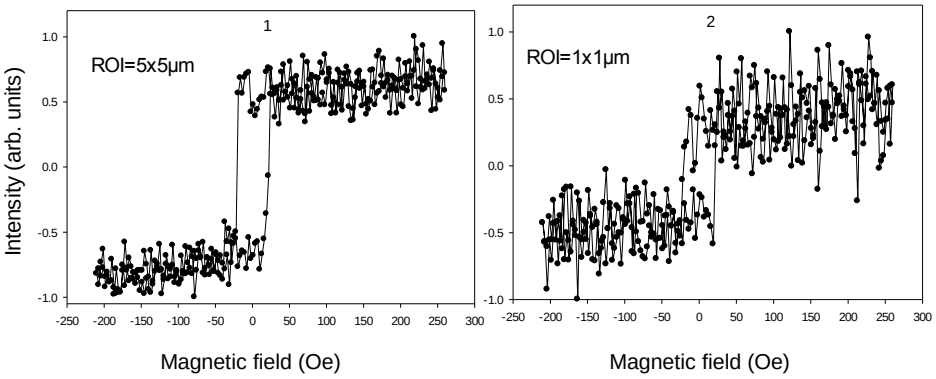

Figure 3.2: Single hysteresis loop at different size of region of interest (ROI).

3.3 Nanowires results

This project focused on the magnetic characteristic of nano-samples. All the samples were fabricated by Xuefeng Hu, the samples are $Ni_{80}Fe_{20}$ with the thickness of 20 nm. Before doing experiment on any of the nano-samples, it was first saturated with a +1000 Oe magnetic field and return back to 0 Oe. For all the nano-samples investigated in this project, the experiments were cycled 20 times to produce average of hysteresis loops with the magnetic field 'step' to be 5 Oe. It was found that these values are the optimum working condition of the whole setup in relation to the computer capability. The repetition also helps to enhance the magnetic domains contrast in the static images of the samples which is also examined in this project. When doing the extraction for hysteresis loops in different areas of the sample, the selected area size is always set to around less than 1 μm x 1 μm to easily generalise the magnetic property in each area without having to compare the different sizes effect of the examined regions. Furthermore, the known effective smallest size of focused MOKE laser point is at 1 μm diameter [56, 57], thus this gives an additional advantage for this Kerr microscopy technique for the possibility of hysteresis loop observation for an area smaller than 1μm width. This is especially useful when examining micro size samples with multiple magnetic domains with width smaller than 1 μm. For all the samples a positive magnetic field is to the right direction and a negative magnetic field aligned in the left direction.

3.4 Cross-wire sample

The first nanowire sample is a cross-shaped nanowire with width of around 1 µm. The experiment was done with the longitudinal Kerr sensitivity setup mode with the longitudinal axis shown in Figure 3.3. The regions of interest for hysteresis loops extractions are shown in Figure 3.3 and will further be discussed using the magnetic domains image results. From the hysteresis loops in Figure 3.4, the coercivity values at different parts of the nanowire are different, suggesting that there are magnetic domains formed at single arm of the wire before the wire is saturated. This is because, when only some parts of the wire has their magnetisation reversed by the external field, the parts that have not been reversed will have opposite magnetisation direction with the reversed parts. Therefore magnetic domains formed at different magnetisation directions. By referring to the hysteresis loop results in Figure 3.4, areas in parts 1 and 8 have the coercivities of 101±4 Oe and 108±4 Oe respectively where these are the two highest coercivity values, therefore magnetisation in these areas will be reversed at higher applied magnetic field than the other.

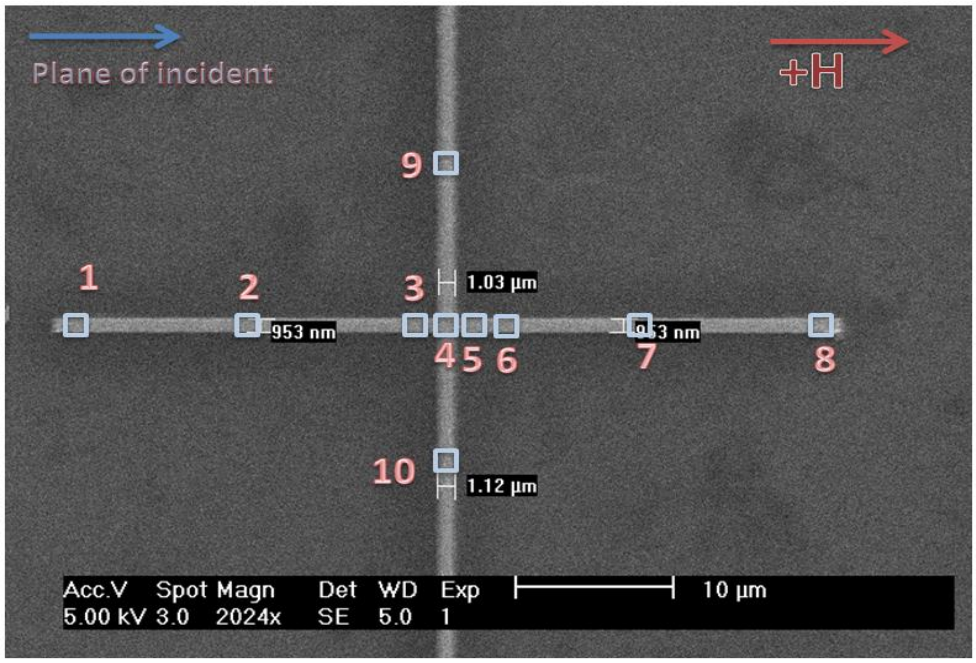

Figure 3.3: Scanning electron microscopy (SEM) image of the cross nanowire with the plane of incident and applied field direction *H* shown in the figure. The numbered areas represent the areas of interest for hysteresis loops extraction.

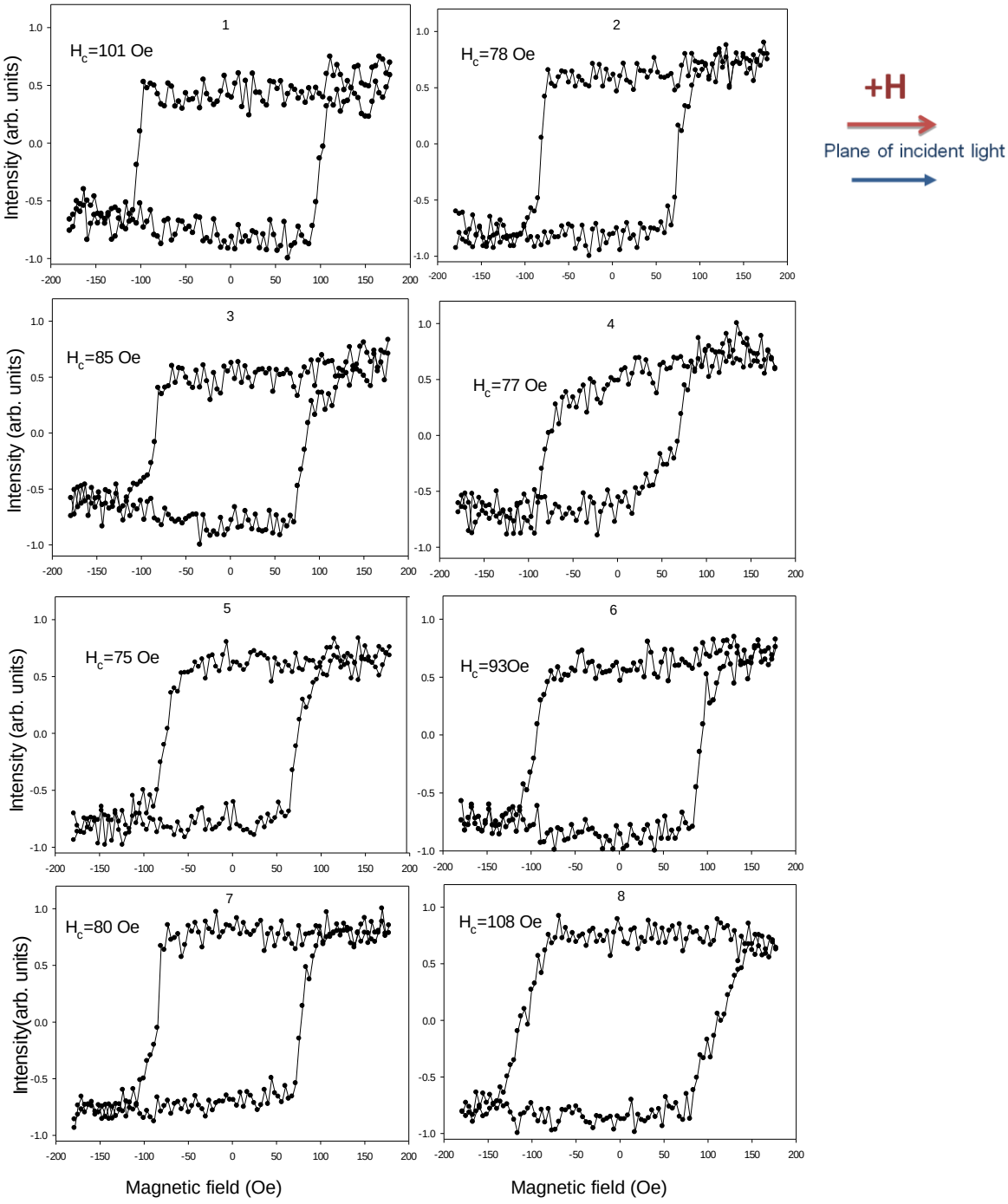

Figure 3.4: Hysteresis loop results of the cross wire at different regions with the coercivity values displayed for each parts. The numbers represent ROI (region of interest) corresponding to the numbered areas in Figure 3.3.

Because of the magnetostatic energy and the shape anisotropy effects, the magnetic moment spins in the cross wire will aligned along the edges for lower energy. For

example, lowest energy for vertical wire will be at vertical direction along the edges and vice versa. From the hysteresis loop results in Figure 3.4, all area except the centre (part 4) are easy axis loops which suggest that the easy axis of the magnetisation is along the wire edges. The hysteresis loop from part 4 is an inter-media axis loop which suggests that there is a vortex domain formed at the line orientation at the junction. The same result was observed by Yongbing [58] and at [59] where vortex domain was observed at the cross wire junction.

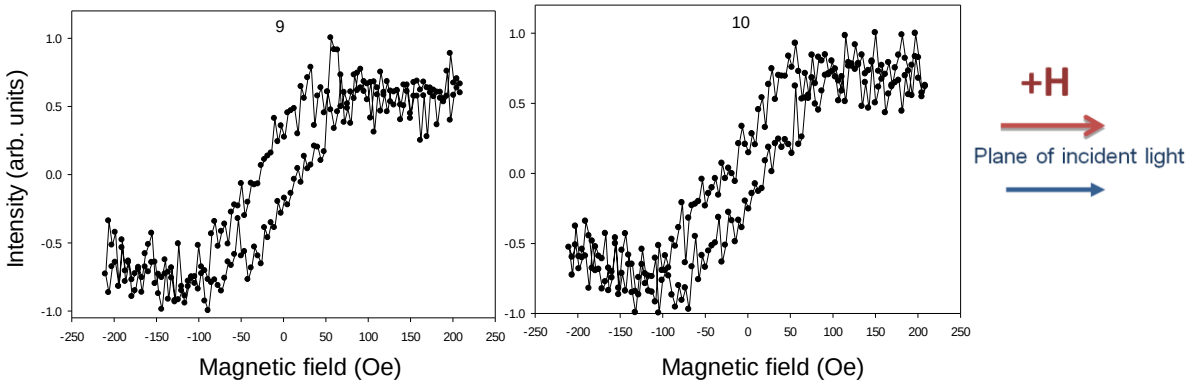

Figure 3.5: Hysteresis loops of the transverse magnetisations in the vertical arms of the cross wire. Shape of loops explains the magnetisation saturation along the hard axis (vertical) of the sample.

The vertical arms in the cross sample have transverse Kerr sensitivity because the magnetisation direction (vertical axis) is perpendicular to the plane of light incidence. Although the setup is for longitudinal Kerr effect, there is still transverse effect in the image as transverse Kerr effect causes change to the light intensity and is not affected by the presence of an analyser. The transverse Kerr effect results of area 9 and 10 (refer to Figure 3.3) are shown in Figure 3.5 and the hysteresis loops show the saturation of the wire along its hard axis.

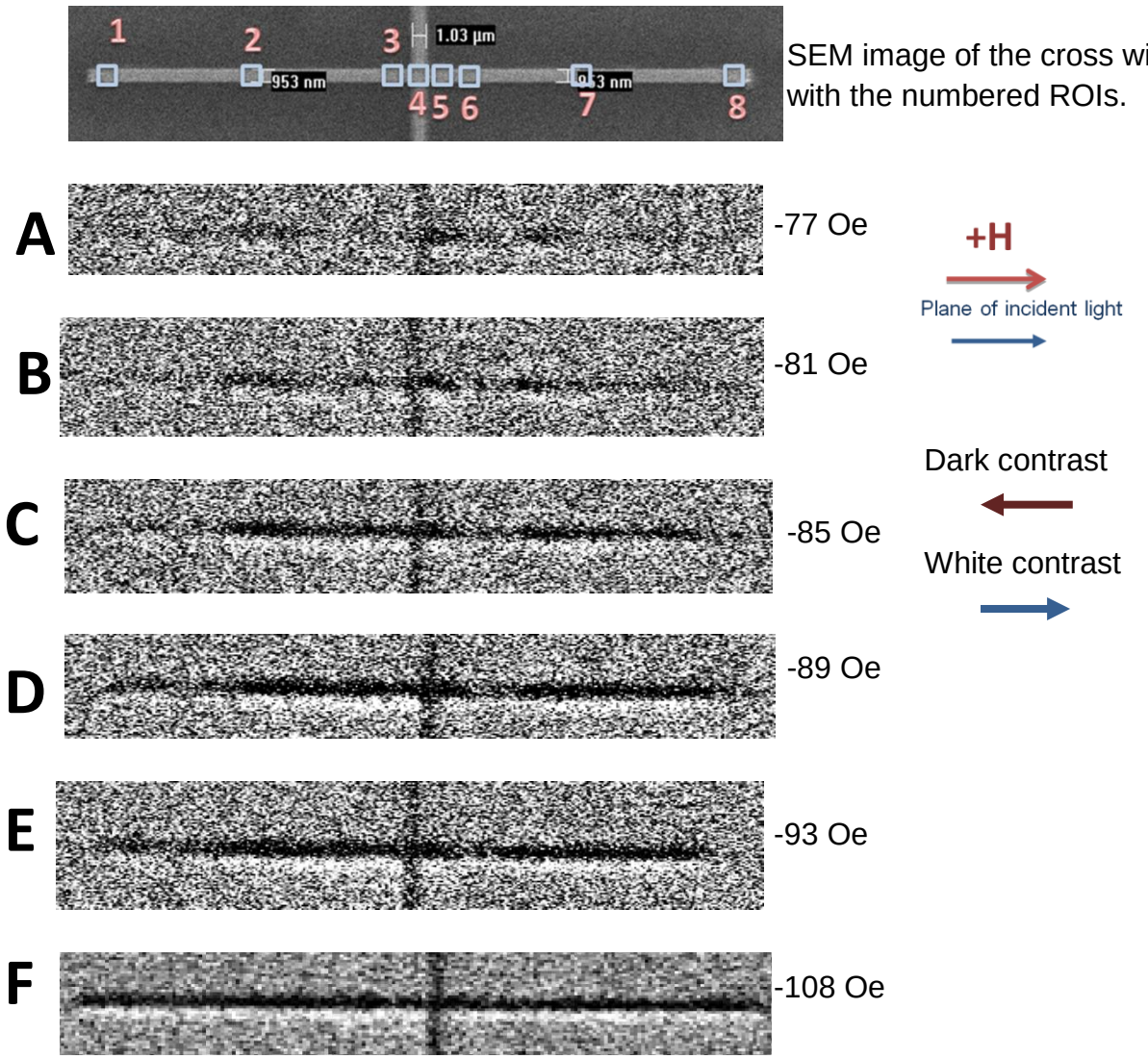

Figure 3.6: Magnetic domain images of the cross wire at different magnetic fields. These are the final results after the magnetic images are produced through image subtraction and image processing as explained in the experimental method section. The SEM image (top) of the sample is numbered at the ROIs. Dark contrast represents magnetisation reversal by applied magnetic field.

In the magnetic domains images in Figure 3.6, the dark contrast shows magnetic reversal and the light contrast represents the magnetic moment at parts which is not yet reversed by the applied magnetic field. From picture A in Figure 3.6, the magnetic domains image for the cross wire indicates that there is a formation of magnetic domains just before the wire is fully saturated. This confirms with the results from the hysteresis loops Figure 3.4 as explained before and the domain

walls motion can be seen in the images, though the structure of the domain wall is too small to be seen due to the resolution limit of the microscope. The same pattern of magnetic domains formation is discovered in the experiments both when the applied magnetic fields are in the positive and negative directions. This pattern is shown in Figure 3.6 in steps of different magnetic fields. For simplicity, magnetisation reversal pattern in the negative magnetic field will be discussed. From Figure 3.4, parts 2, 4, 5 and 7 have negative magnetic field coercivities of -81±4 Oe, -82±4 Oe, -77±4 Oe and -85±4 Oe respectively and referring to image A in Figure 3.6, it is shown that these areas are the first four areas to experience magnetisation reversal by applied magnetic field of -77 Oe. The coercivities for areas 1, 6 and 8 are around -105±4 Oe,-94 ±4 Oe and -107±4 Oe and it is shown that the spin in these areas are not yet reversed by applied magnetic field at -89±4 Oe (shown in image D Figure 3.6). Not until at -93±4 Oe (image E) where these area starts to reverse and finally at -108±4 Oe (image F) they are all saturated. This unique effect in the cross-shaped nanowire is caused by the ferromagnetic characteristics of the wire.

3.5 Zigzag nanowire

The next sample is a zigzag nanowire with width of around 841 nm. The geometry of the zigzag nanowire is shown in Figure 3.7 together with its width and length values. Directly referring to the hysteresis loops results in Figure 3.9 a hard to generalise loops patterns are observed. The coercivities in the positive and negative fields in each loops are different. This is the characteristic of the ferromagnetic zigzag nanowire for the reason that is related to the domain walls motion formed at the corners of the zigzag nanowire. The patterns can be easily studied by referring to the magnetic images results in Figure 3.9. The ROIs are also shown in Figure 3.9 and the magnetisation and the Kerr effects from different MOKE geometry is shown in Figure 3.8.

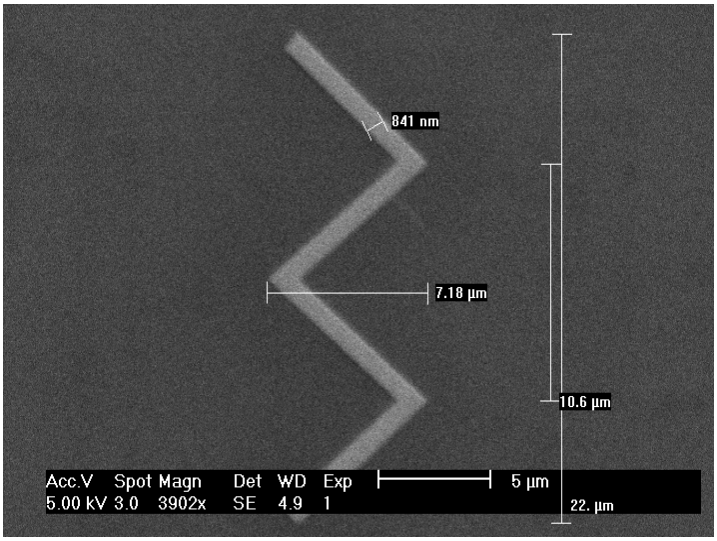

Figure 3.7: SEM image of the zigzag nanowire.

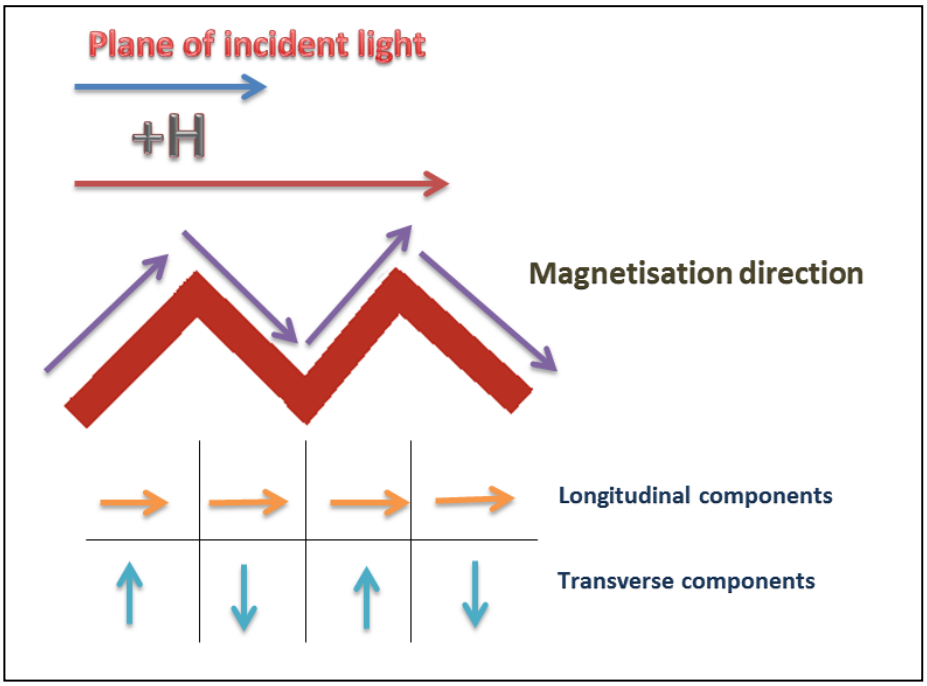

Figure 3.8: Zigzag nanowire Longitudinal and transverse MOKE geometry with the direction of the applied magnetic field and plane of incident light as shown above.

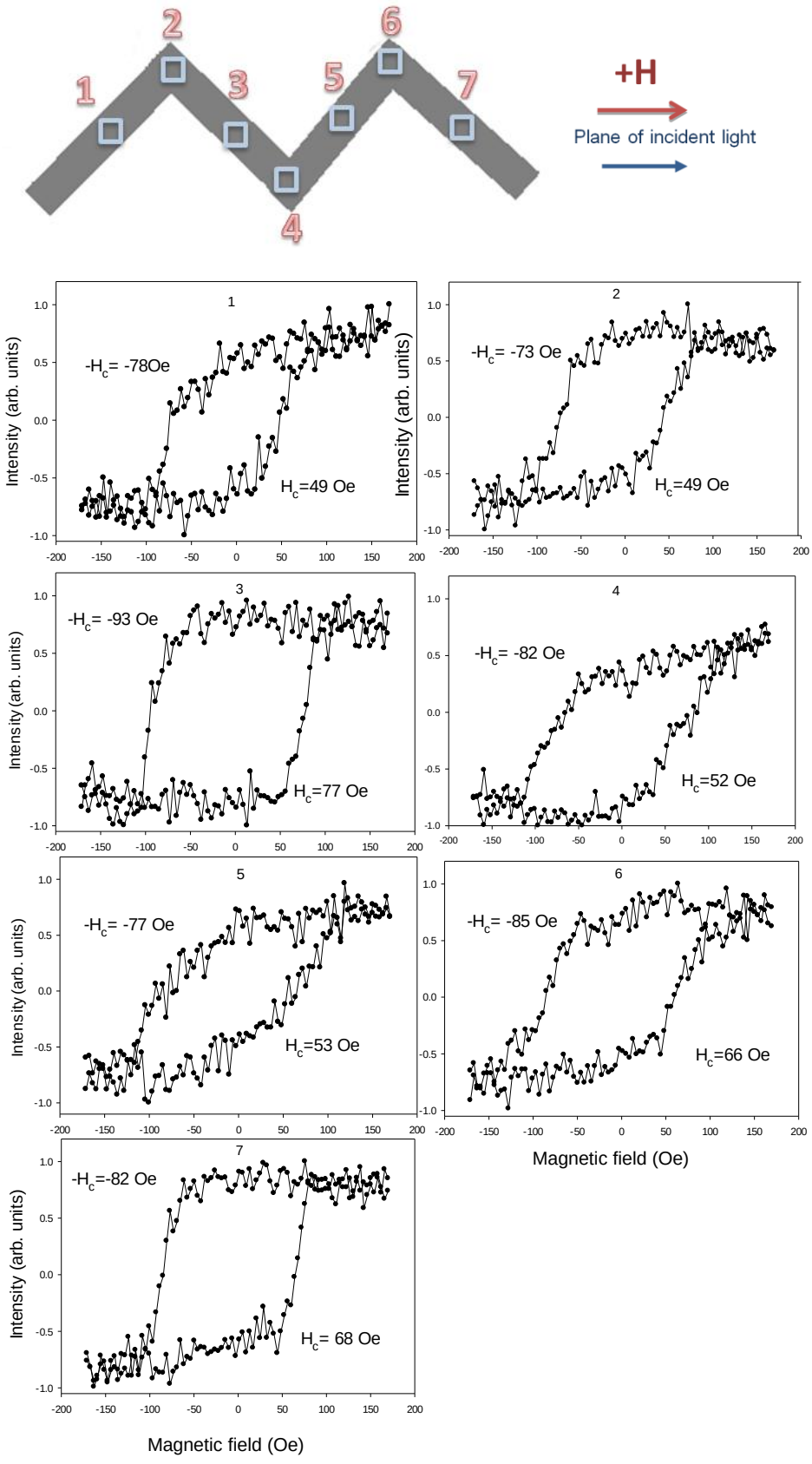

Figure 3.9: The hysteresis loops value of the zigzag nanowire (bottom) and the region of interests (ROIs) areas (top).

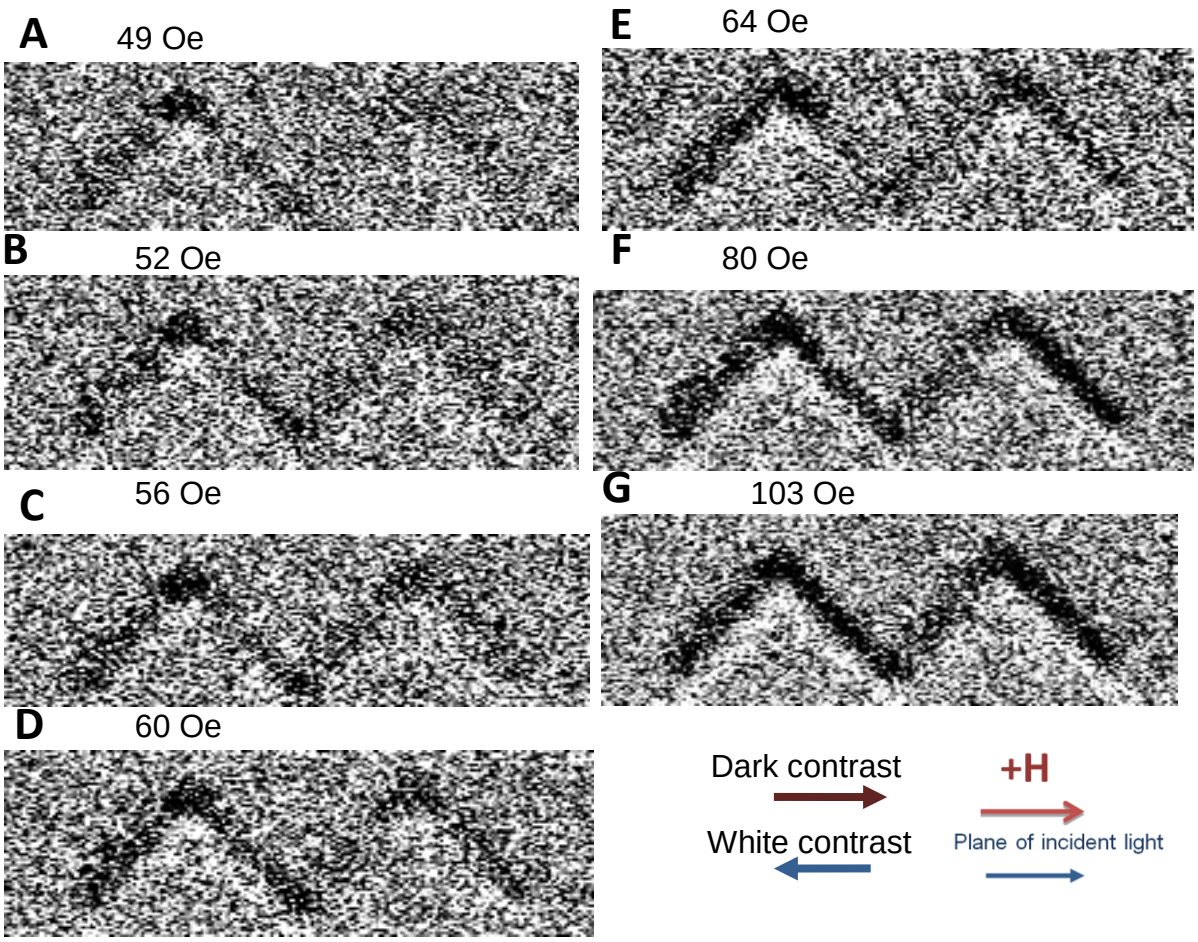

Figure 3.10: The magnetic images of zigzag nanowire at different fields. The dark domains represents magnetisation reversal.

Looking at the hysteresis loops shapes in Figure 3.9, for part 3 and 7, their M_r/M_s values are equal to one, therefore there is no vortex domain formed in these parts. And in part 1 and 5, their M_r/M_s values are the two smallest, therefore there are vortex domains of magnetic moment formed in these parts. In part 2 and 4, the M_r/M_s value is in between one and the smallest, thus the distribution of magnetisation must be in between part 1 and 3. From hysteresis loops results in Figure 3.9, by examining the image sequence, the first magnetisation reversal occurs at the corner of part 2 and it can be seen as the dark contrast in image A Figure 3.10. Then after that, part 1 and 5 start to reverse. Again from the hysteresis loop results, part 3 has the highest coercivity at 77 Oe at the positive field. Thus by referring to the domains image in picture E at magnetic field 64 Oe, the magnetic moment in this area remains not reversed until at applied magnetic field 80 Oe where reversal occur as shown at image F. The early magnetisation reversals in part 1 and 5 are caused by

the domain walls motion that formed earlier at the corners of the sample. These walls will move driven by the magnetic field to cause early magnetisation reversal than usual. Additionally in part 1, the end of the arm has a shape anisotropy effect where the magnetic moments tend to align along the edge, therefore there is magnetic domain formed due to this effect that also contribute to the magnetisation distribution in that area. In image E Figure 3.10, it is shown that the domain wall separating domains in part 2 and part 3 moves to the right side at magnetic field of 64 Oe. The results display the complicated distributions of magnetisation in zigzag nanowire which was caused by the magnetostatic effect and the domain walls motion. Same patterns are also observed in the positive magnetic field experiment and thus, confirming the ferromagnetic properties of the zigzag nanowires. It is observed that the coercivity values at opposite applied magnetic fields are different in zigzag nanowire. The differences in the coercivity values between the negative and positive magnetic fields are shown in Table 3.1.

Area no.	$-H_c$ (Oe)	H_c (Oe)	Coercivites difference (Oe)
1	78	49	29
2	73	49	24
3	93	77	16
4	82	52	30
5	77	53	24
6	85	66	19

Table 3.1: Table showing the difference in coercivities between the positive and negative field.

The transverse Kerr effect in the zigzag nanowire gives different transverse directions in each arm, this is summarised in diagram form in Figure 3.8. For that reason, a distinct black and white contrasts will form in each arm describing the opposite magnetisation direction of transverse Kerr effect. To observe this effect, the Kerr microscope setup was changed into the transverse MOKE sensitivity by means of longitudinal to transverse sensitivity setup. This method change the transverse Kerr effect into longitudinal Kerr effect as described in the experimental section of

this thesis and thus will effectively observe the transverse Kerr effect. The resulting magnetic domains in the zigzag nanowire are shown in Figure 3.12. Black and white contrasts formed in the image in Figure 3.12. It means that the magnetisation direction of white and black contrast is opposite to each other. Because the measurement is a transverse Kerr effect, opposite 'jumps' of the hysteresis loops in arms 1 and 4 are observed shown in Figure 3.11. Therefore, this strongly supports the transverse Kerr effect discussion above. The results not just verify the transverse Kerr effect in the zigzag nanowire but in addition to that, they also demonstrate the working ability of the Kerr microscope to detect the transverse Kerr effect by using the longitudinal with transverse sensitivity setup.

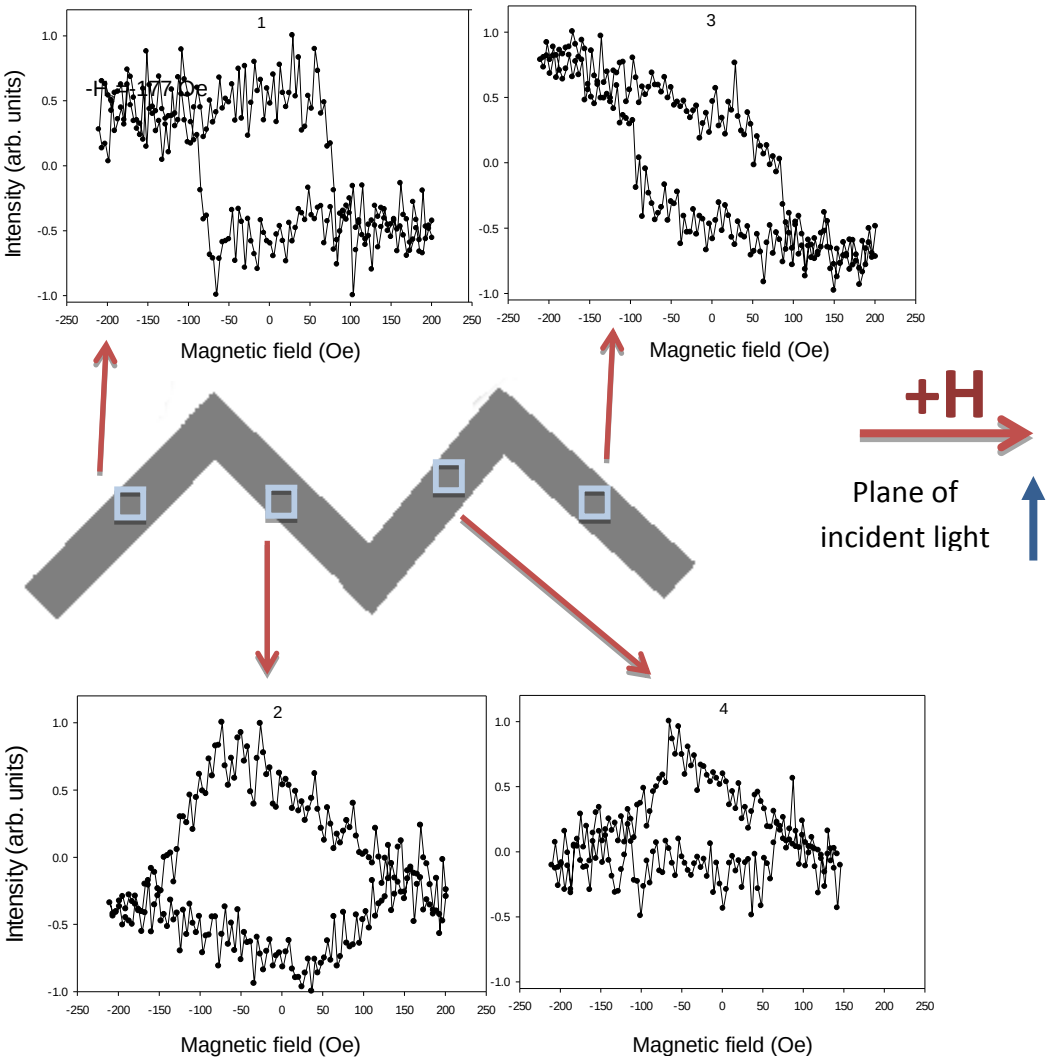

Figure 3.11: Hysteresis loops of zigzag nanowire for the transverse geometry but by using longitudinal with transverse sensitivity setup.

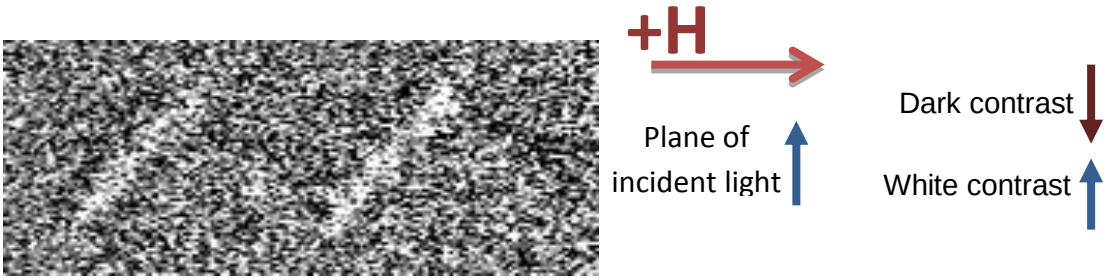

Figure 3.12: Transverse MOKE image of the nanowire showing black and white pattern.

3.6 Nanowires with asymmetric notch and nucleation pad

Due to the effect of shape anisotropy on the alignment of magnetic spins in the sample, the pad will has lower coercivity because the magnetic spin in the pad form a vortex along the circular edge of the pad. Because of this fact, there is a domain wall at the junction between the nanowire and the pad separating the magnetic domains in each area. This domain wall can be propagated along the wire driven by the magnetic field to cause an early magnetisation reversal along the wire. But the introduction of notch will pin the domain wall to cause different distribution of magnetisation direction in the nanowires.

A set of samples was prepared for the magnetic domains observation in nanowires with asymmetric notch. For all the samples, their asymmetric notches are fabricated to have one short side and one long side. Measuring from the long axis of each wire, the short side have angle of between 12^{o} and 15^{o}, whereas the long side have angle of between 42^{o} and 55^{o}. All the short side of the notches are facing the nucleation pad of the nanowire. The samples can be generalised into two categories, the first group is for samples with their notches located in the middle of the nanowire and the second group is for samples with their notches positioned at about a quarter length of the wire away from the nucleation pad. Their dimensions are described in Table 3.2.

Group	Sample number	Width of wire (nm)	Notch depth (nm)	Percentage of notch depth to the width of wire (%)
1	4	321	92	28.7
	11	324	131	40.4
2	7	384	152	39.6
	6	435	202	46.4
	5	334	111	33.2
	14	394	223	56.6
	13	374	192	51.3
	12	354	172	48.6

Table 3.2: Table showing the geometry of the wires with notch.

In the first group, there are two wires with nearly the same width but different notch depth. The experiments were done using the usual longitudinal Kerr sensitivity setup where the magnetisation direction is parallel to the plane of incidence.

3.6.1 Group one

Sample 11

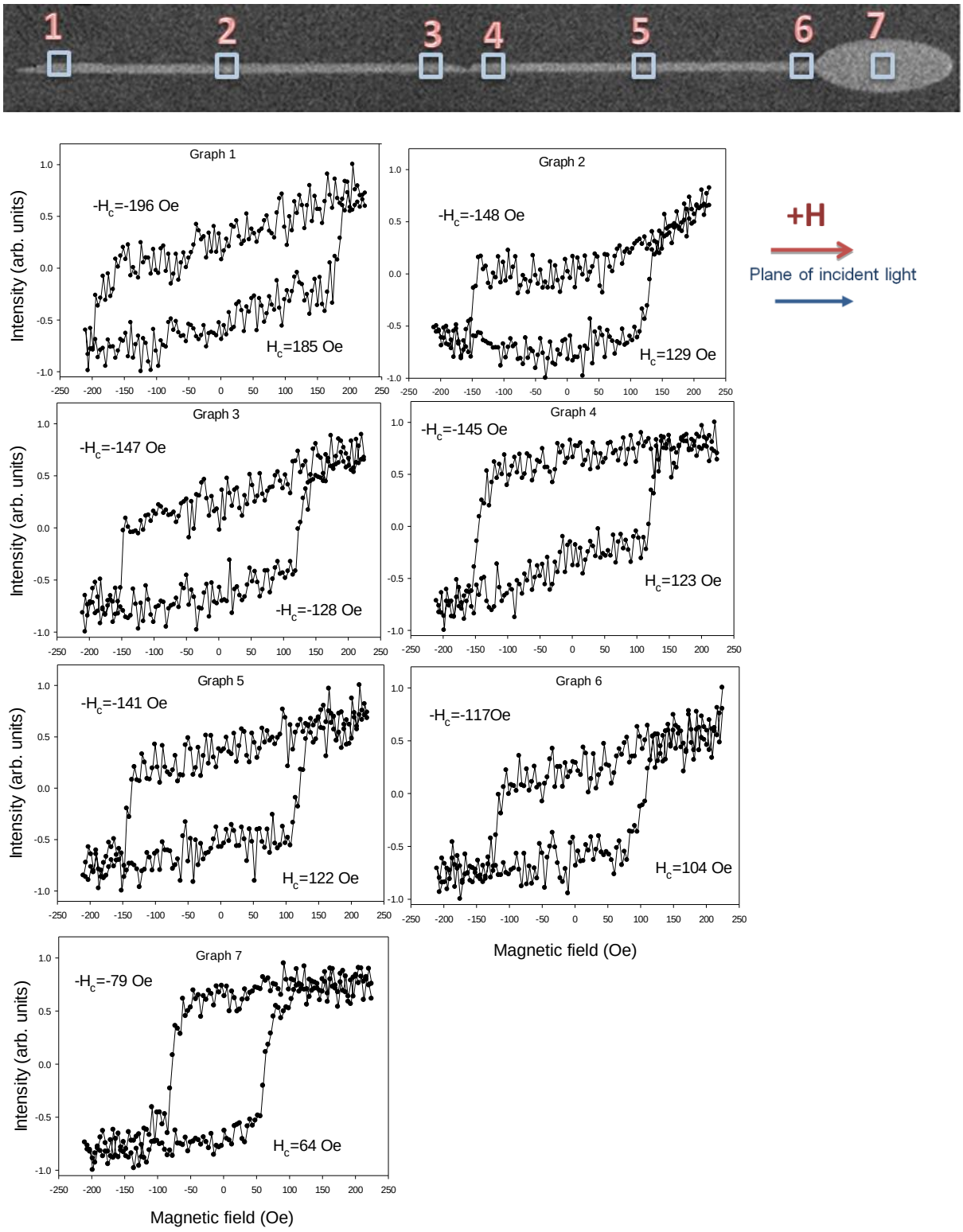

Figure 3.13: SEM image (top) of sample 11 with the numbered ROIs. Hysteresis loops (bottom) result of sample 11 corresponding to the area shown at the nanowire.

Sample 11 has wire width of 324 nm and notch depth of around 131 nm. The hysteresis loop results at different parts of the wire are shown in Figure 3.13 and magnetic domain images of the sample are shown in Figure 3.14. There is a dominant grey region in the pad of the sample at all magnetic fields and can be seen in the domain images in picture F in Figure 3.14. This is not a magnetic contrast in the sample and is caused by the saturated pixels in that area. The main reason is because the light intensity and exposure time for the camera was set to optimum only for the nanowire part. As a result, the large pad size is too bright and causes saturation to the pixels. Though, it still contains some Kerr signal which is proven by the hysteresis loop at part 7 of Figure 3.13. In general, the propagation of domain wall in both negative and positive applied magnetic field are the same, but for this sample the discussion will focus on magnetic domain wall formed at negative applied magnetic field. As discussed before, the elliptical pad has the lowest coercivity compared to the other parts of the nanowire. From graph 6 in Figure 3.13, it is indicated that the domain wall started to propagate to the wire at magnetic field strength of -117 Oe (negative field coercivity). This propagation is shown in the magnetic image A in Figure 3.14 for which the magnetisation in part 6 has started to reverse. Again from Figure 3.13, regions in part 2, 3 and 4 have nearly the same coercivity values. As a result, the magnetisation reversals in these regions are nearly at the same time and this is pictured in the magnetisation reversal at image B and C of Figure 3.14. The end of the nanowire at part 1 have the highest coercivity and its magnetisation is not yet reversed at negative field of -151 Oe which is presented in picture C of Figure 3.14. However the magnetisation is reversed at coercivity value of -196 Oe as shown in the hysteresis loop result (Figure 3.13) and the image after reversal can be seen at picture E in Figure 3.14. At the range of -196 Oe the domain wall in the nanowire disappear because in the whole region of the nanowire, the magnetisation is aligned in the same direction along the long axis of the nanowire. Finally, it can be seen that the difference of coercivity values between part 2 and 5 is only around 7 Oe for both negative magnetic field and positive magnetic field which means that the pinning of domain wall propagation affected by the notch structure is very weak as the coercivity values difference is too small.

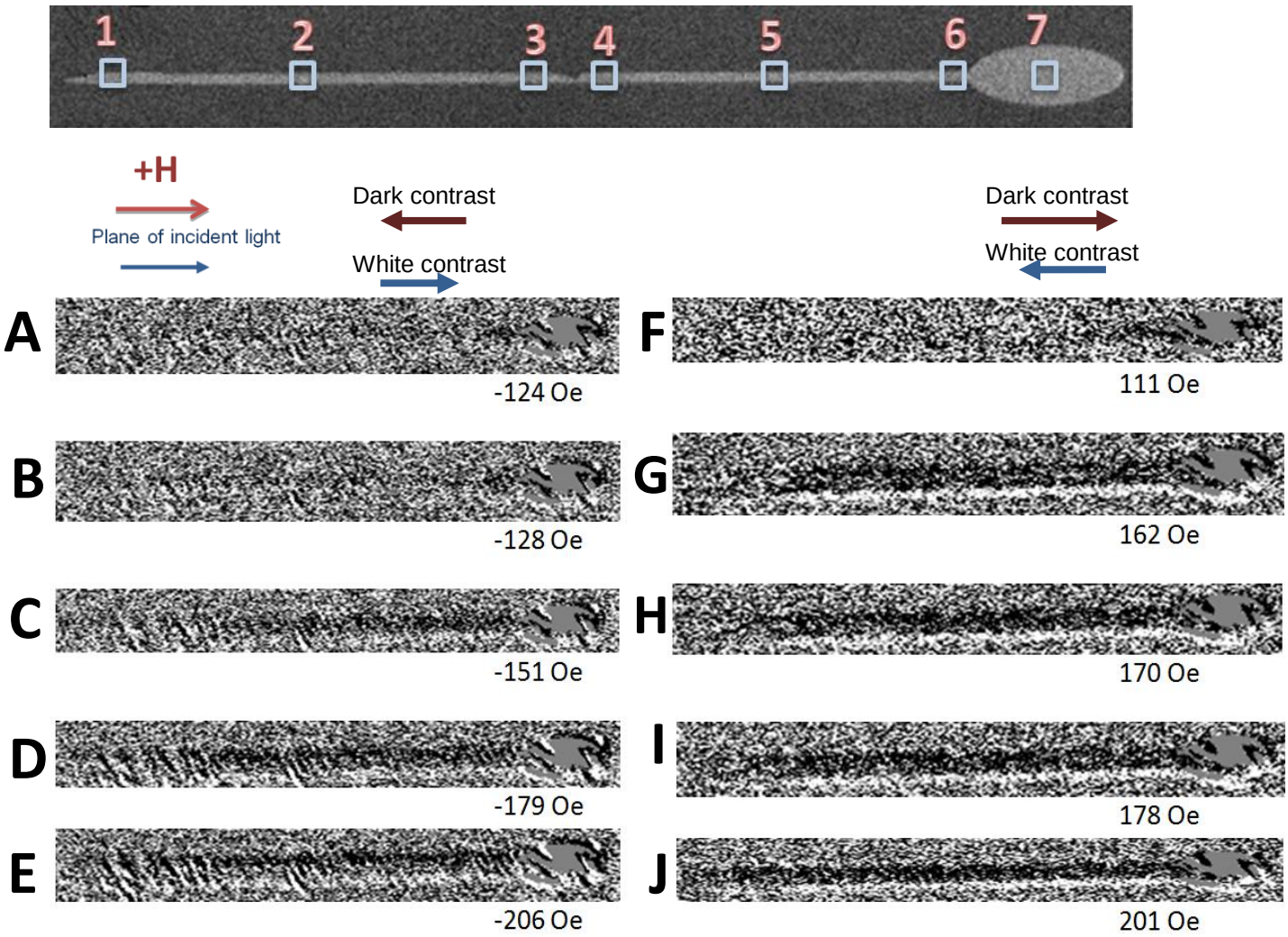

Figure 3.14: SEM image (top) of sample 11 with the numbered ROIs. Magnetic domain images (bottom) of sample 11, dark contrast corresponds to reversed magnetisation by the applied magnetic field.

Sample 4

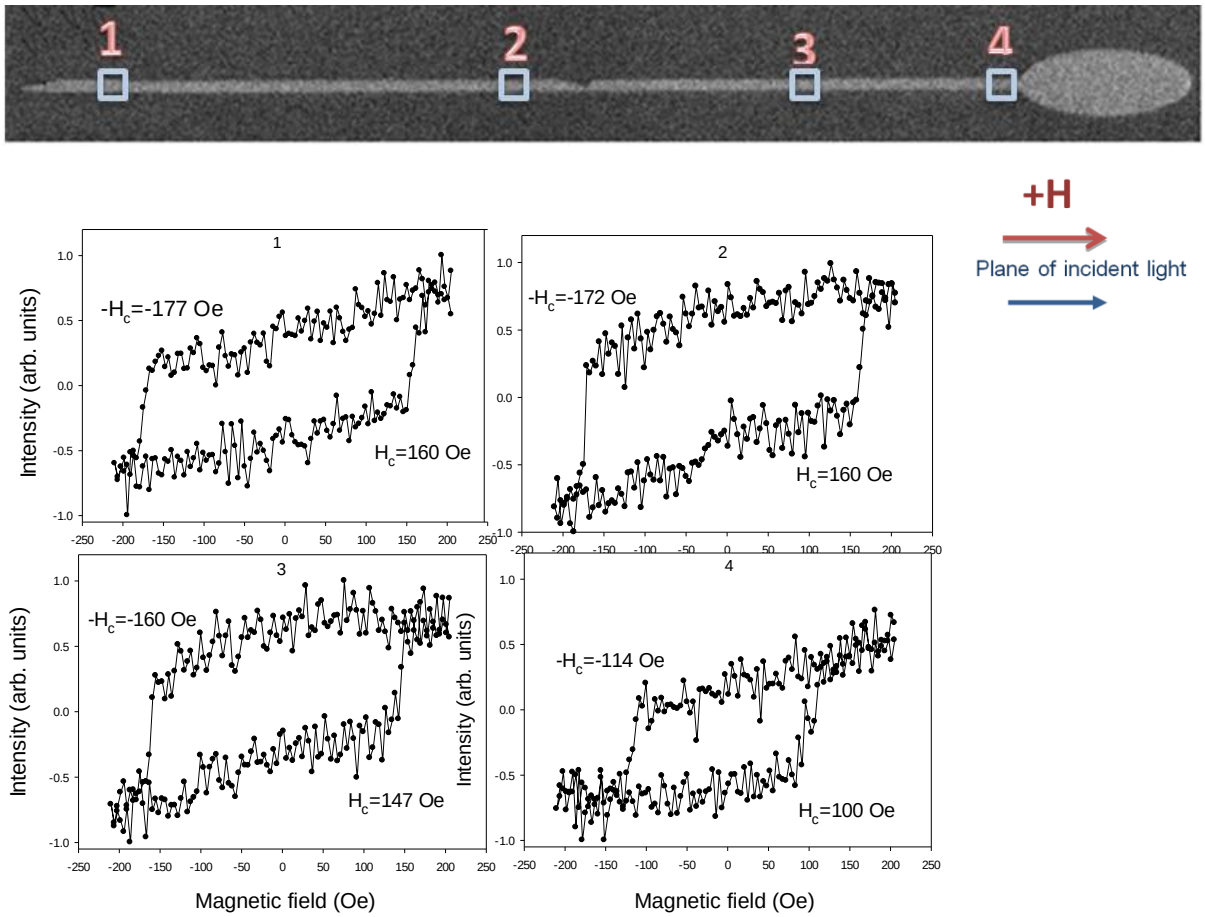

Figure 3.15: SEM image (top) of sample 4 with the numbered ROIs. Hysteresis loops (bottom) result of different parts of wire 4.

The wire width of sample 4 is 321 nm and notch depth of around 92 nm. As demonstrated by the hysteresis loops in Figure 3.15, the same progression occur in the second sample similar to the progression in sample 11. Again due to pixels saturation, the pad is covered by strong grey contrast as seen in Figure 3.16. The image results focus only at the positive magnetic field for generalisation of the magnetisation distribution in this sample. In this case, for the positive magnetic field the domain wall produced at the junction between the pad and the wire is a tail-to-tail domain wall. Domain wall propagation starts at 100 Oe at part 4 as shown by the coercivity result in graph 4 of Figure 3.15. At 146 Oe, the domain wall remains in the region around part 4 as shown by the magnetic image in picture A of Figure 3.16. The difference in coercivity in part 2 and 3 of the wire is 12 Oe and 13 Oe for the

negative field and positive field respectively. This can be seen in picture b in Figure 3.16 where only half of the wire has its magnetisation reversed and the other half near the end is not yet reversed.

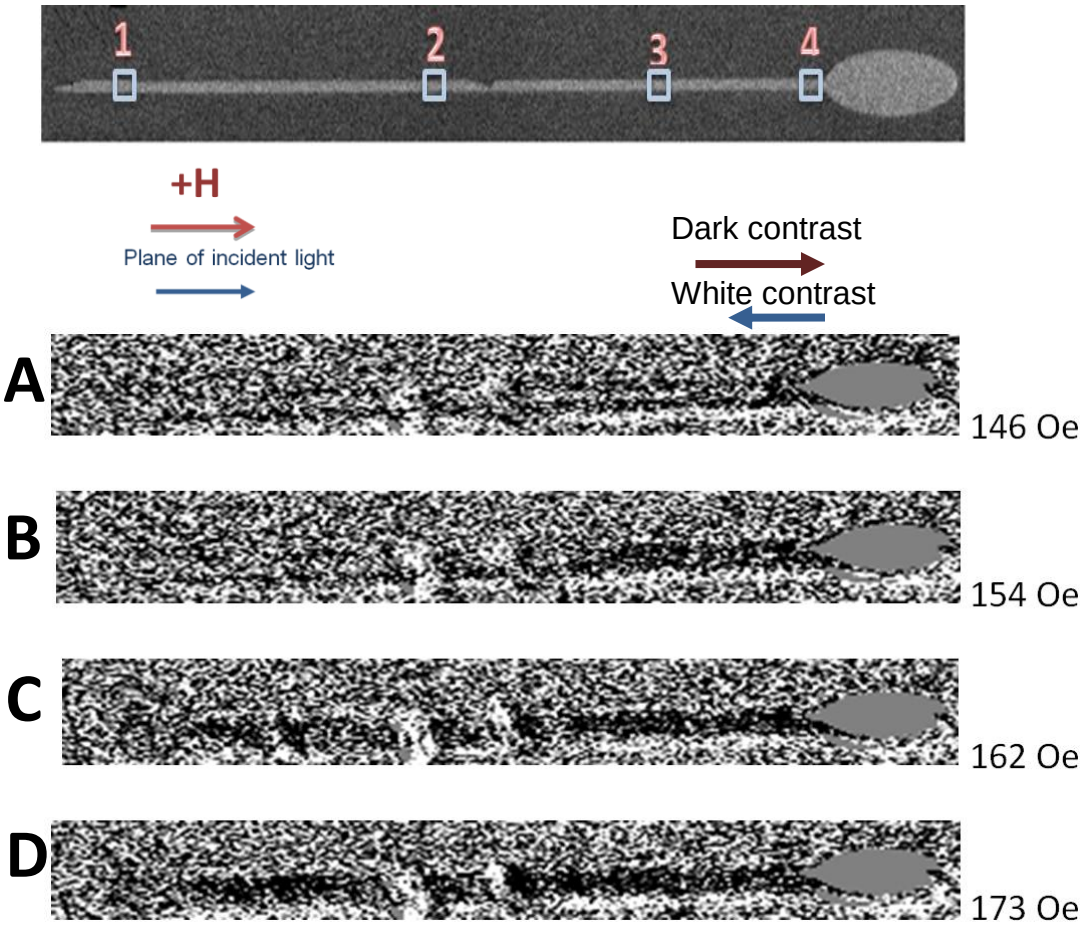

Figure 3.16: SEM image (top) of sample 4 with the numbered ROIs. Magnetic domain images (bottom) of sample 4, dark contrast corresponds to reversed magnetisation by the applied magnetic field. The grey regions in the pad are the saturated pixels (no Kerr data) of the camera.

3.6.2 Discussion for group one

The results show that the pinning of domain wall causes different magnetisation distributions in the wire at different magnetic field. Further, the magnetic field driven depinning of the domain wall at the notch is also observed. It is proven from the result that the strength of domain wall pinning depends on the percentage depth of the notch with the wire width. For sample 11 with percentage notch depth of 28.7%,

it has a coercivity difference between before and after notch at about 6 Oe. And the difference in coercivity between before and after notch for sample 4 is around 12 Oe. Thus, the difference is two times larger in sample 4 than in sample 11. This proves that the deeper the notch is the stronger the pinning effect will be. To produce a much larger difference in coercivities of area before and after notch, the nucleation pad for the samples can be modified to a shape that have lower coercivity so that domain wall can be formed at a much lower magnetic field.

3.6.3 Group two

For group two samples, the magnetic domains formed at the samples when the magnetisation starts to reverse and before the wire magnetisation is fully saturated. The patterns are repeatable and formed at both positive applied magnetic field and negative applied magnetic field. Each sample produces different magnetic domains pattern and will be describe in detail in this section.

Sample 14

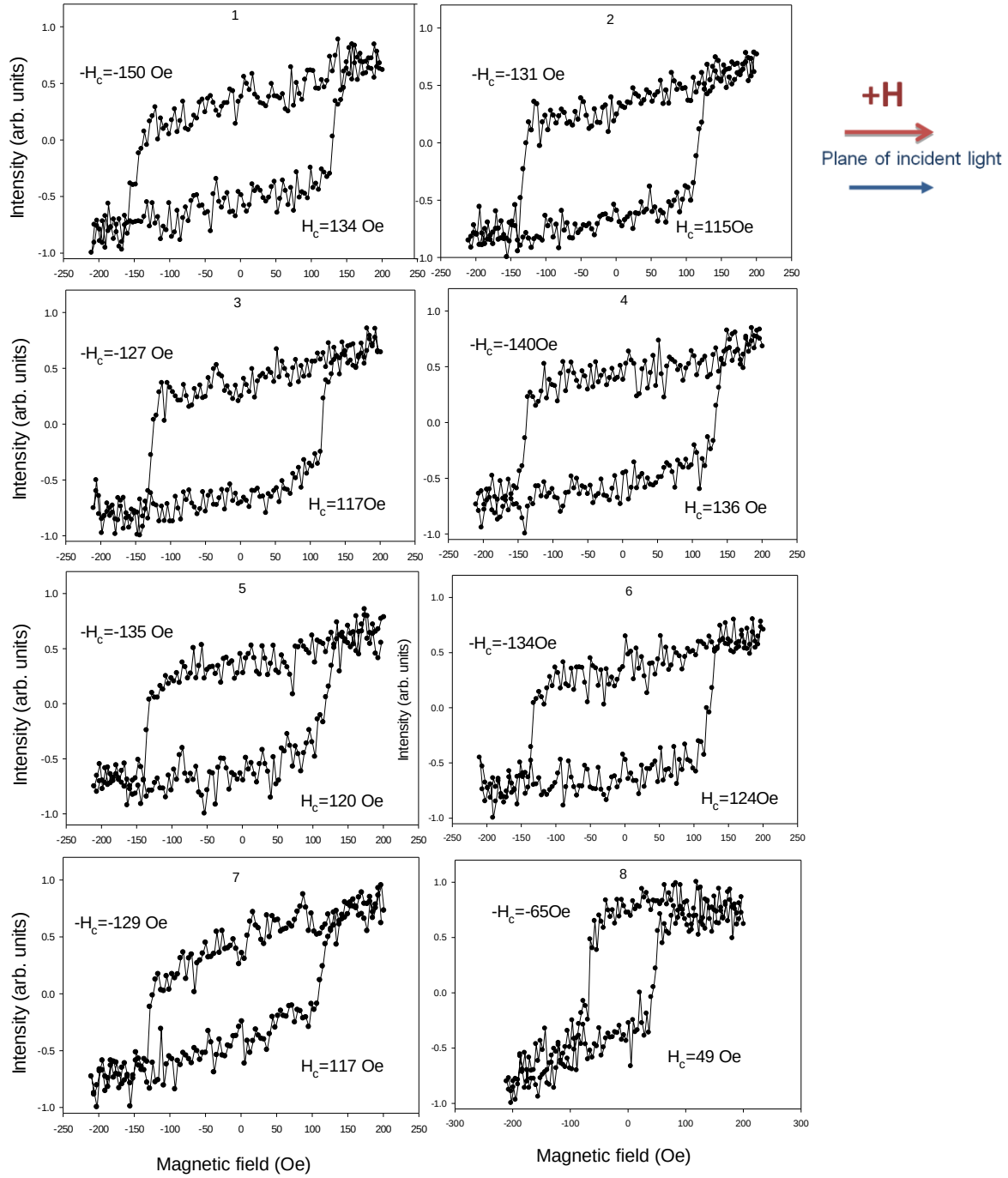

Figure 3.17: Scanning electron microscopy (SEM) image (top) of sample 14 with the numbered ROIs. Hysteresis loops (bottom) of sample 14 at different parts of the wire.

The coercivity values shown in Figure 3.17 indicate that there is a multiple magnetic domains formation in the nanowire during magnetisation reversal. The pattern of the magnetic domains can be easily explained by referring to the magnetic domain image results of the nanowire shown in Figure 3.18. The domain wall propagation from the junction at part 7 can be seen at picture A in Figure 3.18. Before the domain wall propagate further to the notch, at the same time, region around part 2 undergo magnetisation reversal as shown in picture B in Figure 3.18 and it is confirmed by the hysteresis loop result shown in Figure 3.17. This is unexpected as such pattern was never been observed before [60, 61, 62]. The two domain walls in part 2 propagate sideways until all the magnetisation in the whole wire gets reversed. The whole events can be seen in details by the magnetic domains image in Figure 3.18.

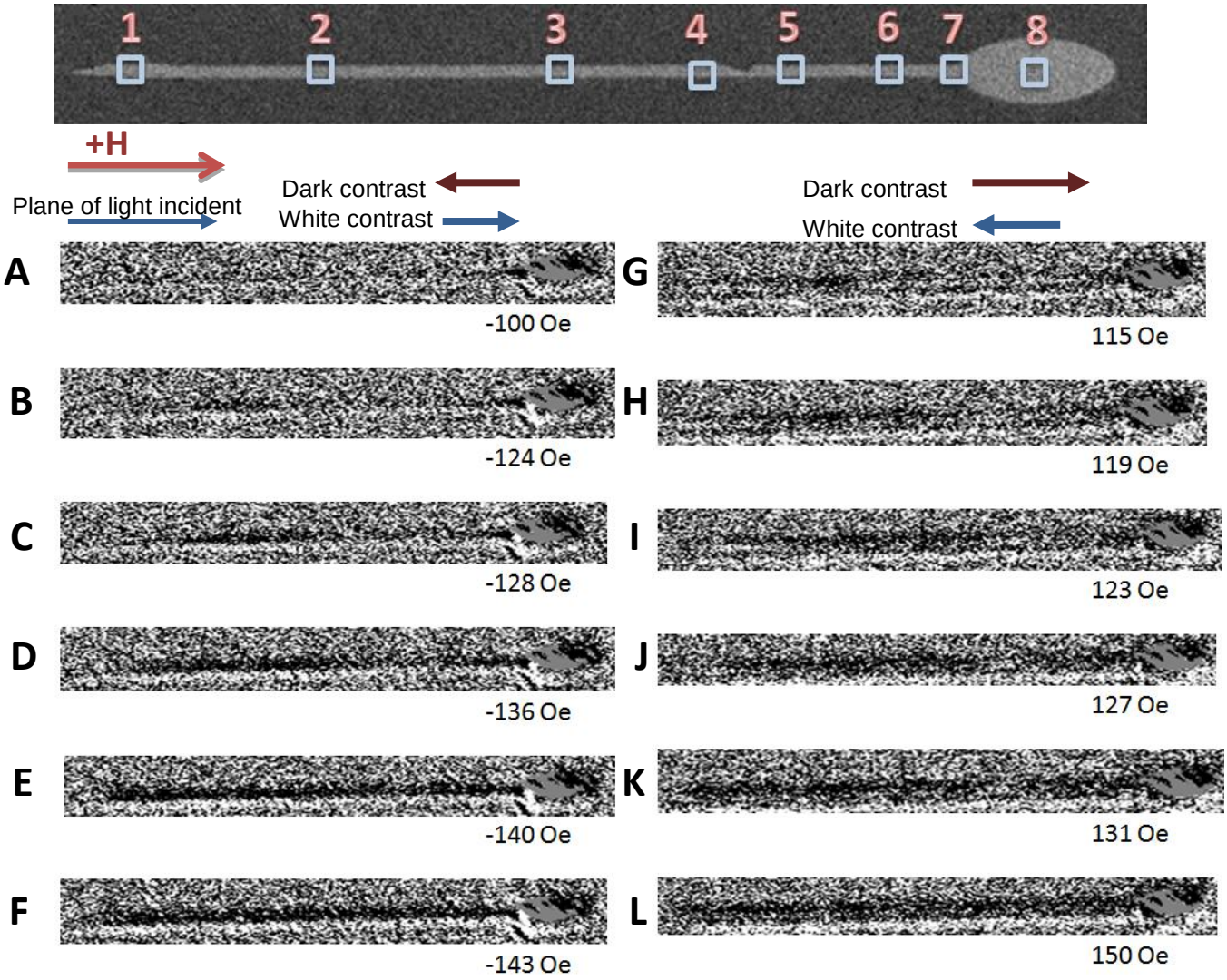

Figure 3.18: SEM image of sample 14 (top). Magnetic domain images (bottom) of sample 14 where the dark domain contrast represents magnetisation reversal.

Simulation result for sample 14

(a) Pad simulation

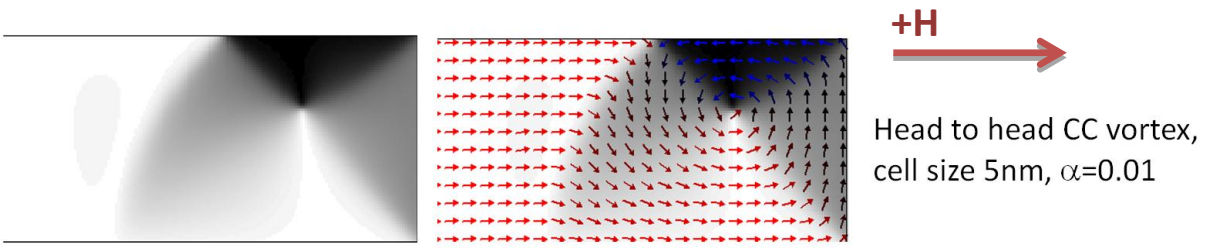

(b) Wire simulation

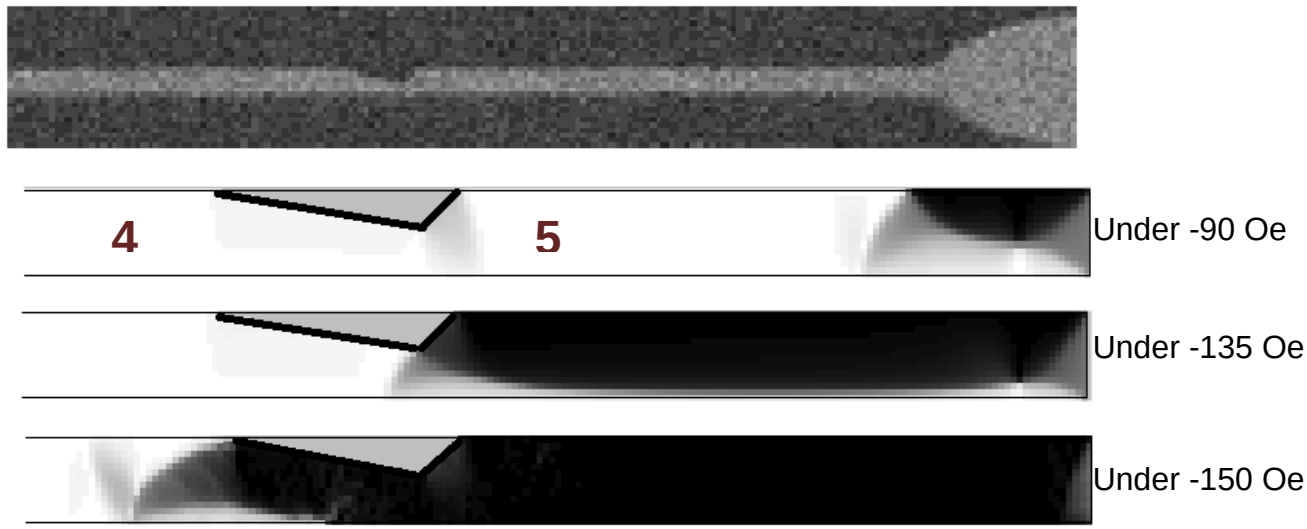

Figure 3.19: (a) Pad simulation showing the cell size and magnetisation direction. (b)The top image is the scanning electron microscopy (SEM) image of sample 14 and then the simulation results of sample 14 showing domain wall motion before the notch.

The simulation results confirms with the hysteresis loops result at part 5 of Figure 3.17 where the coercivity is exactly -135 Oe, and also at part 4 where the coercivity is -14O Oe which is at an accepted range of simulation result of -150 Oe. The motion of domain is also the same as observed in the domains image in Figure 3.18.

Sample 13

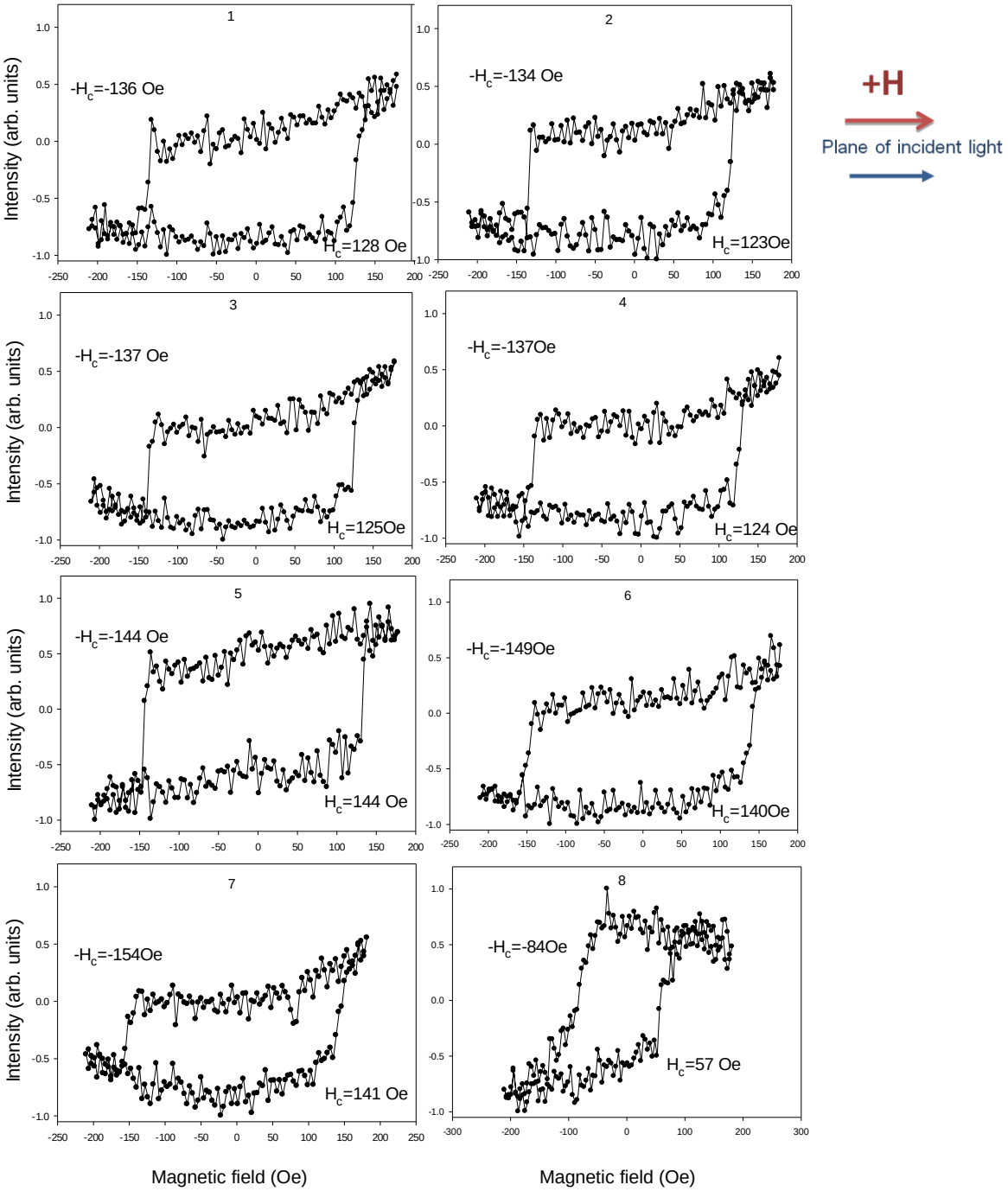

Figure 3.20: SEM image of sample 13 (top) with numbered ROIs (regions of interest). Hysterersis loops (bottom) of sample 13 at different ROIs.

Figure 3.20 shows the hysteresis loops result for different regions in the sample. Similar to sample 14, it can be deduced that there is a random distributions of magnetic domains in the wire before full magnetisation reversal. The discussion will focus on the negative magnetic field results. The first magnetisation reversal occurs at the region of the wire which is after the notch. From the hysteresis loops result in Figure 3.20, the magnetisation reversal for the parts after the notch (part 1, 2, 3 and 4) are nearly at the same value of applied magnetic field. It is demonstrated in image C in Figure 3.21, where the whole region of the wire which is after the notch is reversed at magnetic field of -140 Oe. The magnetisation distributions remain in that state until at -144 Oe (as shown by part 5 hysteresis loop result in Figure 3.20) where the domain wall becomes depinned and spread to part 5. The domain wall continue to spread towards the nucleation pad until it disappear at -154 Oe (coercivity of part 7 shown in hysteresis loop result in Figure 3.20) where the whole magnetisations of the wire are reversed along the applied magnetic field.

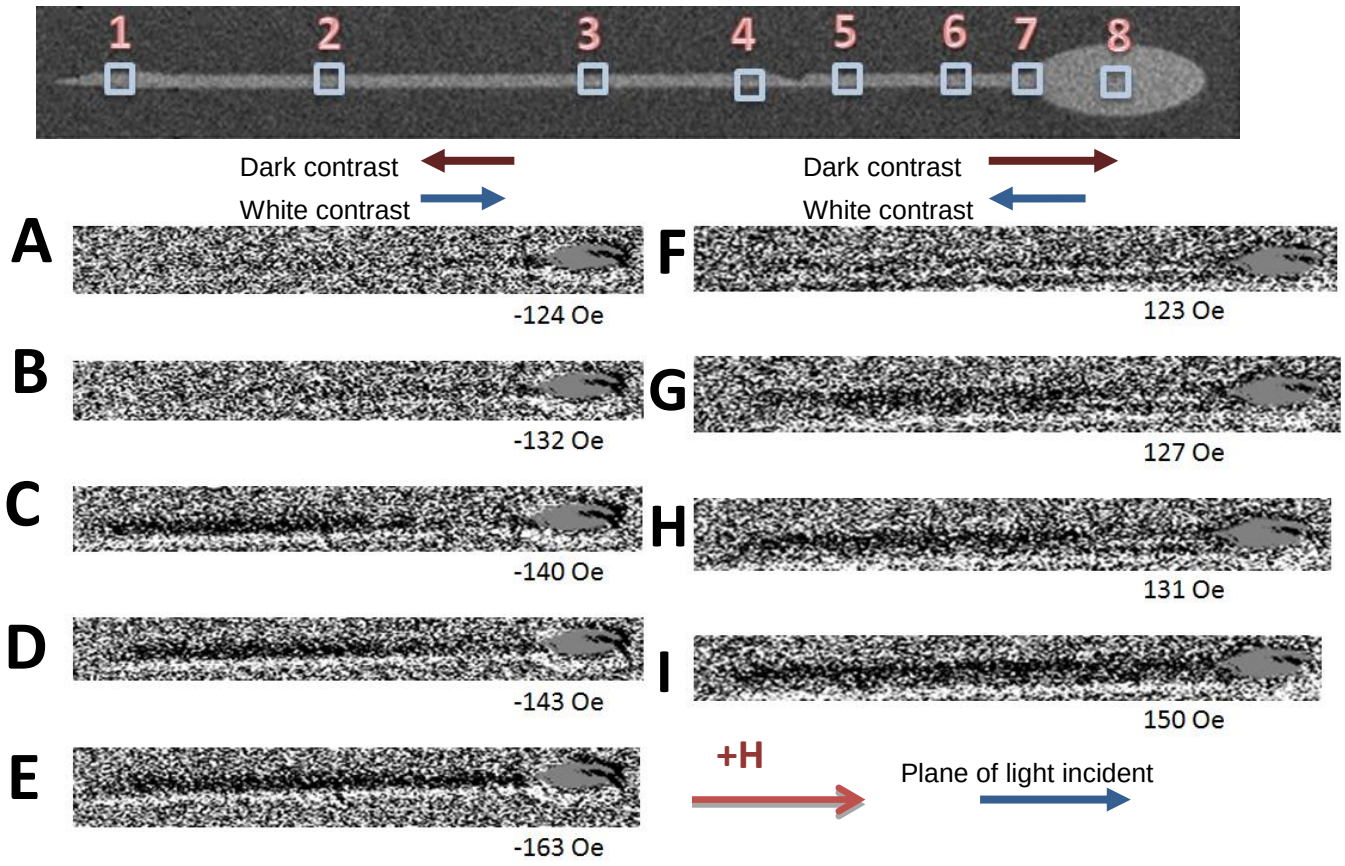

Figure 3.21: SEM image of sample 13 (top) with numbered ROIs. Magnetic images (bottom) of sample 13 at different magnetic field. Dark contrast represents magnetisation reversal in the area by the applied magnetic field.

Sample 7

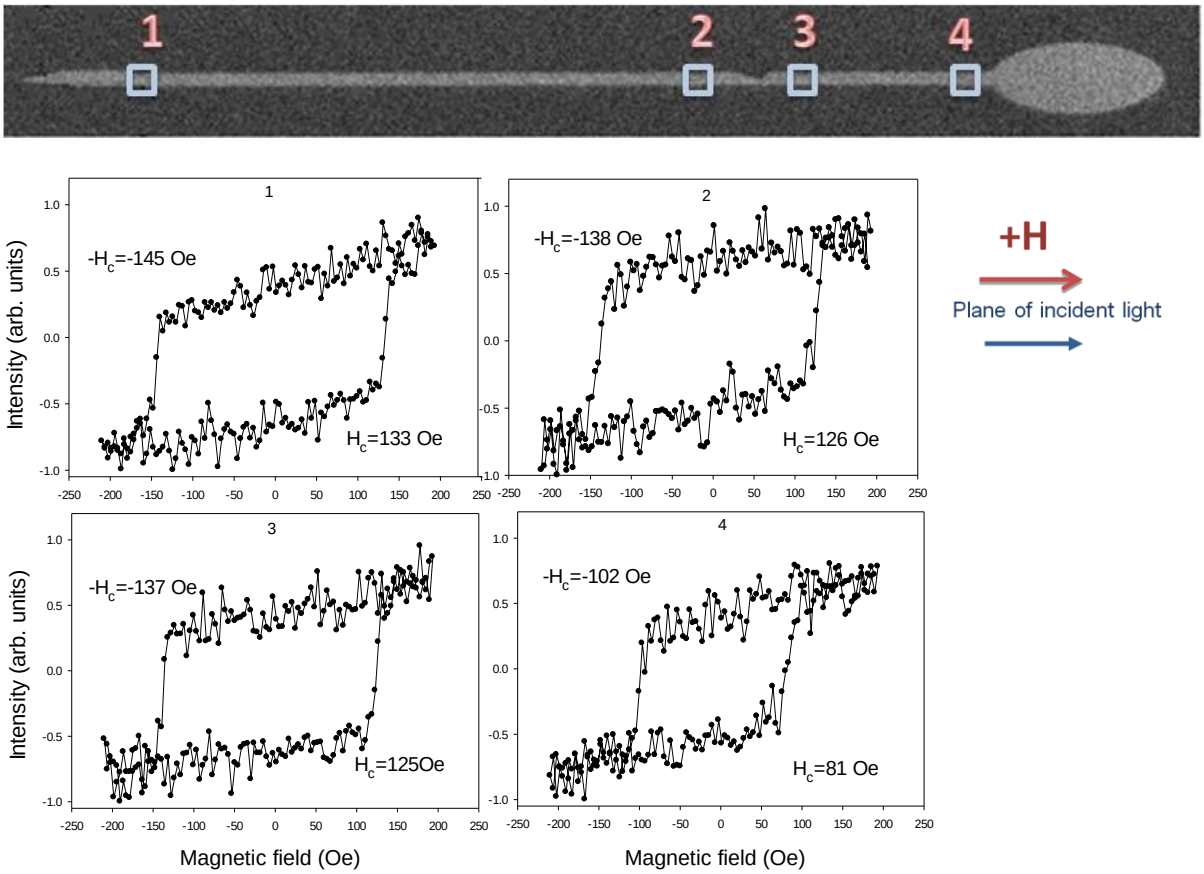

Figure 3.22: SEM image of sample 7 (top) with numbered ROIs and Hysteresis loops (bottom) of sample 7 at each ROI.

For sample 7, the hysteresis loop extractions are focused into 4 parts of the wire where magnetic domains form upon full magnetisation reversal. Part 4 of the wire has the lowest coercivity as shown in Figure 3.22 and domain wall spread to this part from the junction as shown in image B of Figure 3.23. Part 2 and 3 have nearly the same coercivity and their magnetisation reverse after part 4. The domain wall move further to the left and reach part 1 at -145 Oe from the hysteresis loop result in Figure 3.22 and the reversal can be seen in image -155 Oe where the whole magnetisation in the wire is reversed.

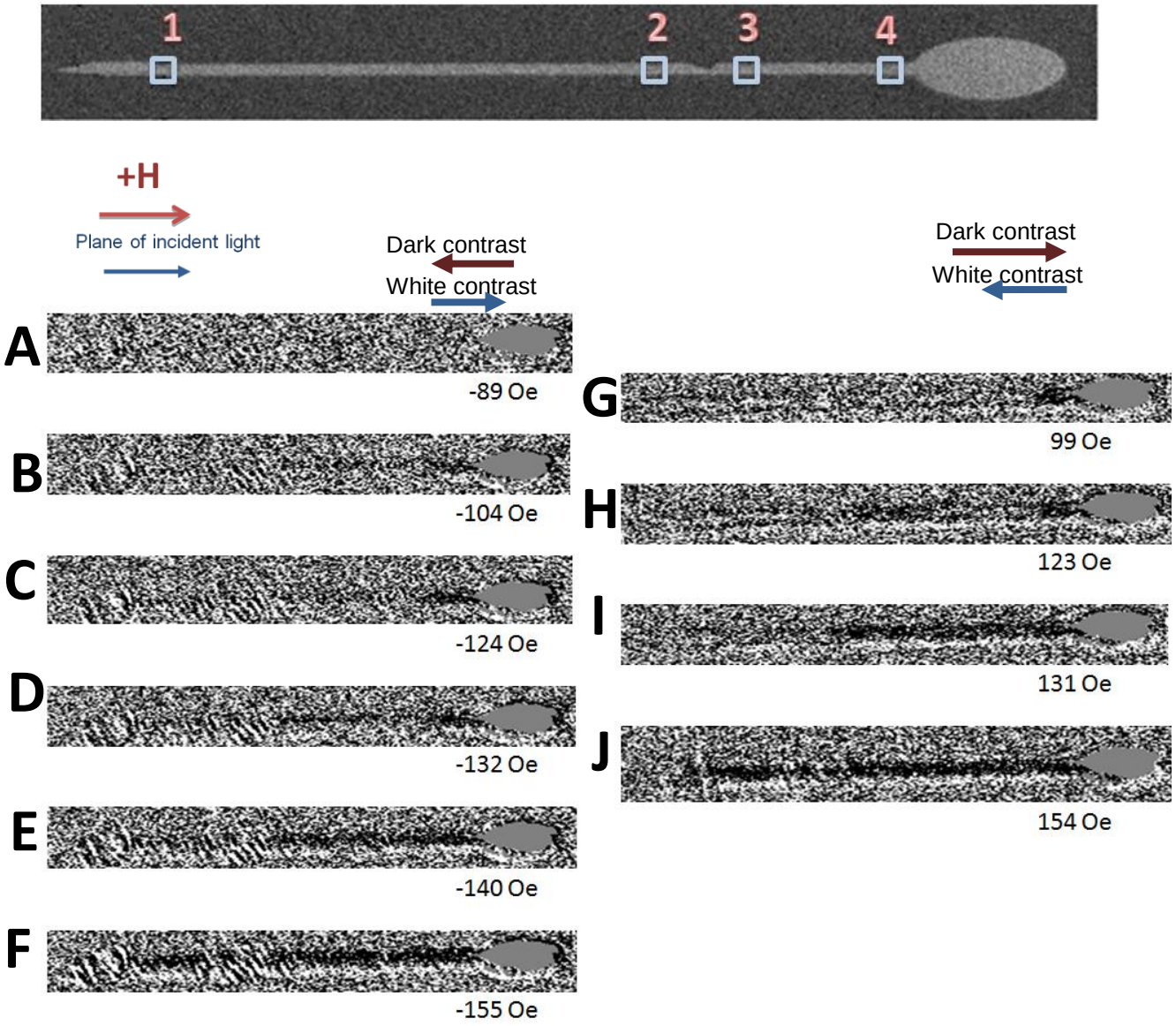

Figure 3.23: SEM image of sample 7 (top) with numbered ROIs. Magnetic images (bottom) of sample 7 at different magnetic field. Dark contrast represents magnetisation reversal in the area by the applied magnetic field.

Sample 12

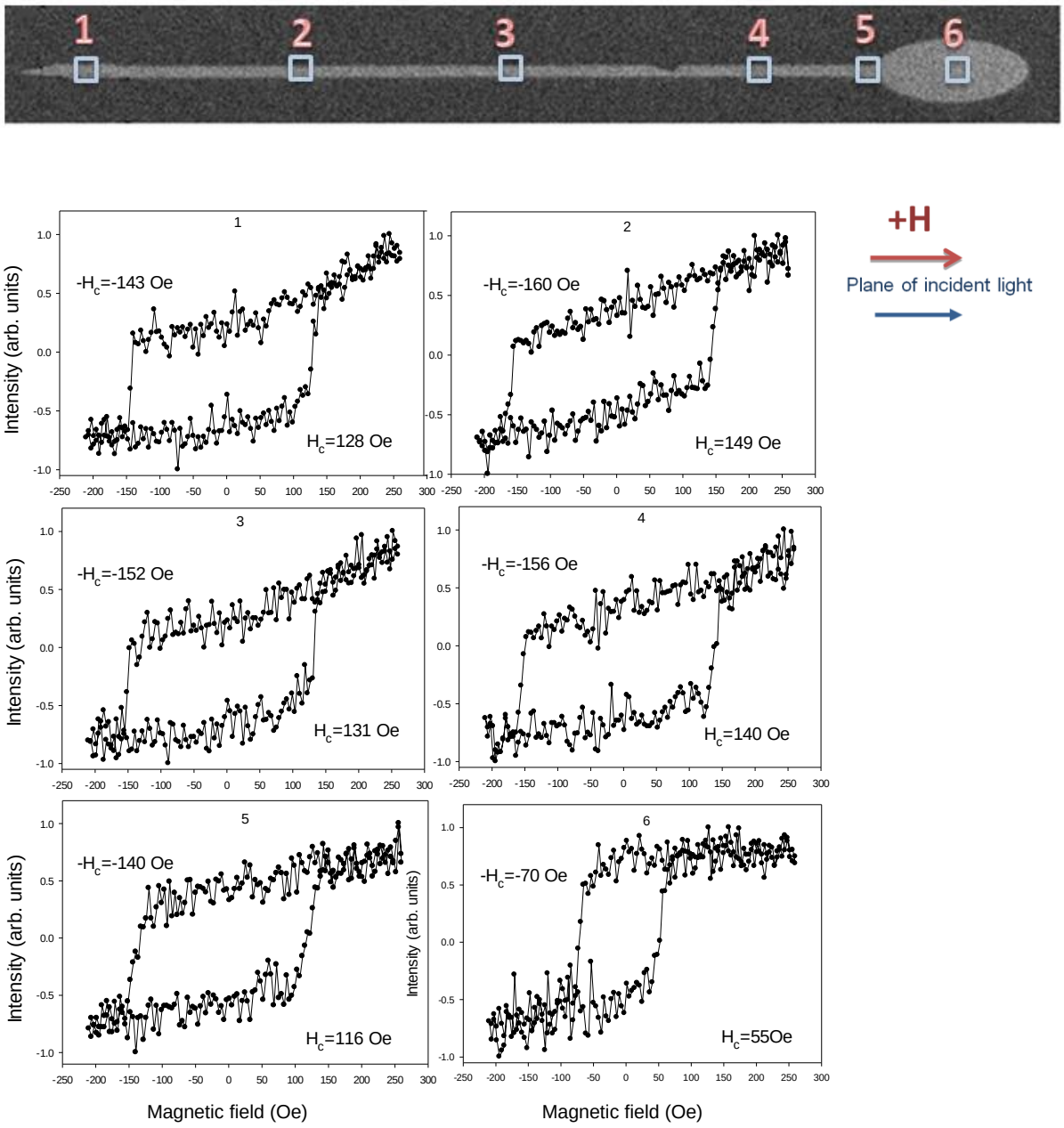

Figure 3.24: SEM image of sample 12 (top) with numbered ROIs (regions of interest). Hysterersis loops (bottom) of sample 12 at different ROIs.

As described before, the grey region in the pads shown in the magnetic images in Figure 3.25 are the saturated pixels. But the focus in here is the magnetisation distribution of the wire part which is optimised when at high light intensity. However, a separate experiment was done with lower exposure time of the camera to get the hysteresis loop from the pad as shown in graph 6 of Figure 3.24. The magnetic domain patterns can be examined from Figure 3.25. Unlike sample 14, 13 and 7, this sample has three regions of early magnetisation reversal as shown in image H and also proven by the coercivity values at different parts in Figure 3.24. The final region that experience magnetisation reversal is part 2 with coercivity values of –160 Oe and 149 Oe for the negative and positive magnetic fields respectively.

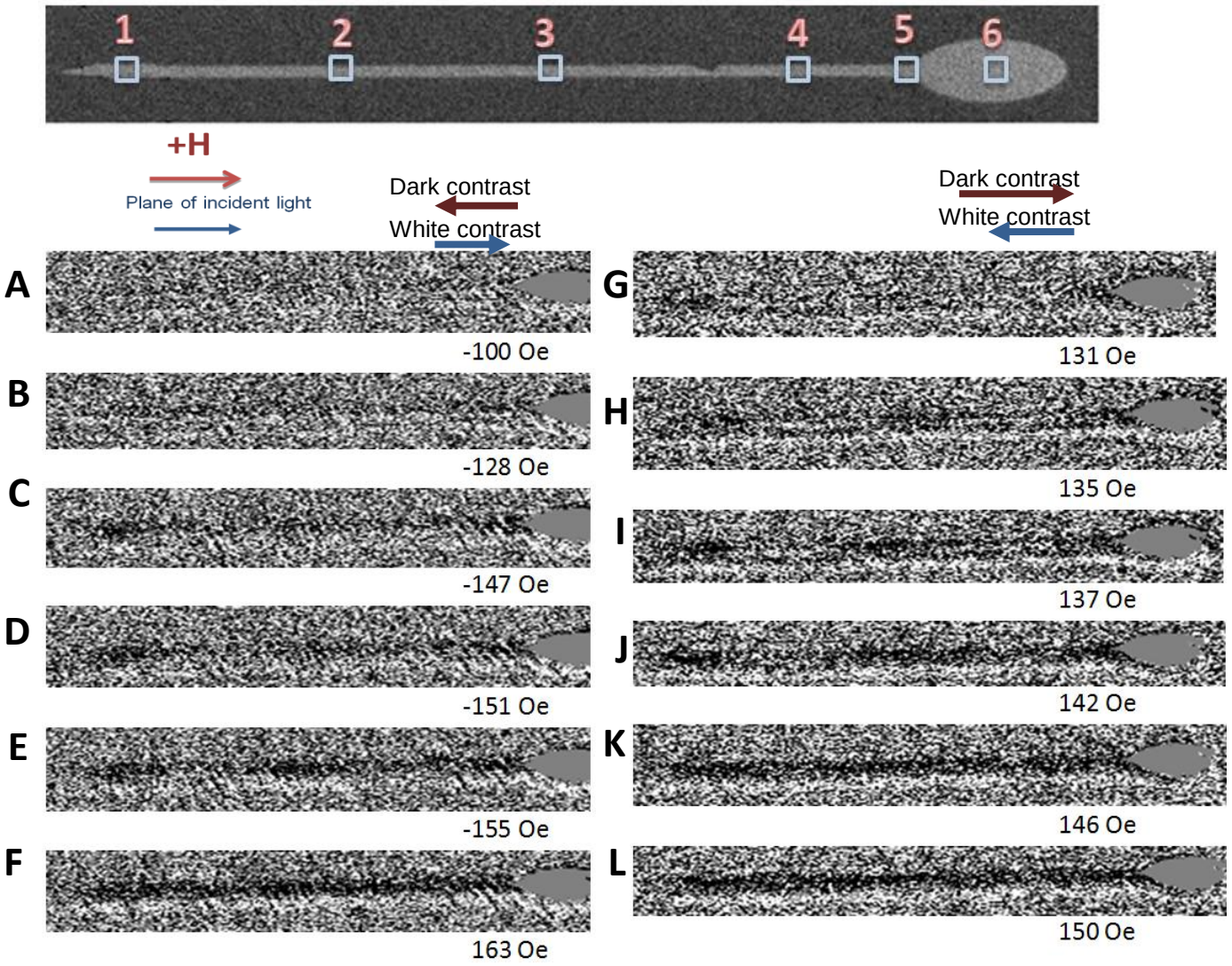

Figure 3.25: SEM image of sample 12 (top) with numbered ROIs. Magnetic images (bottom) of sample 12 at different magnetic field. Dark contrast represents magnetisation reversal in the area by the applied magnetic field.

Sample 6

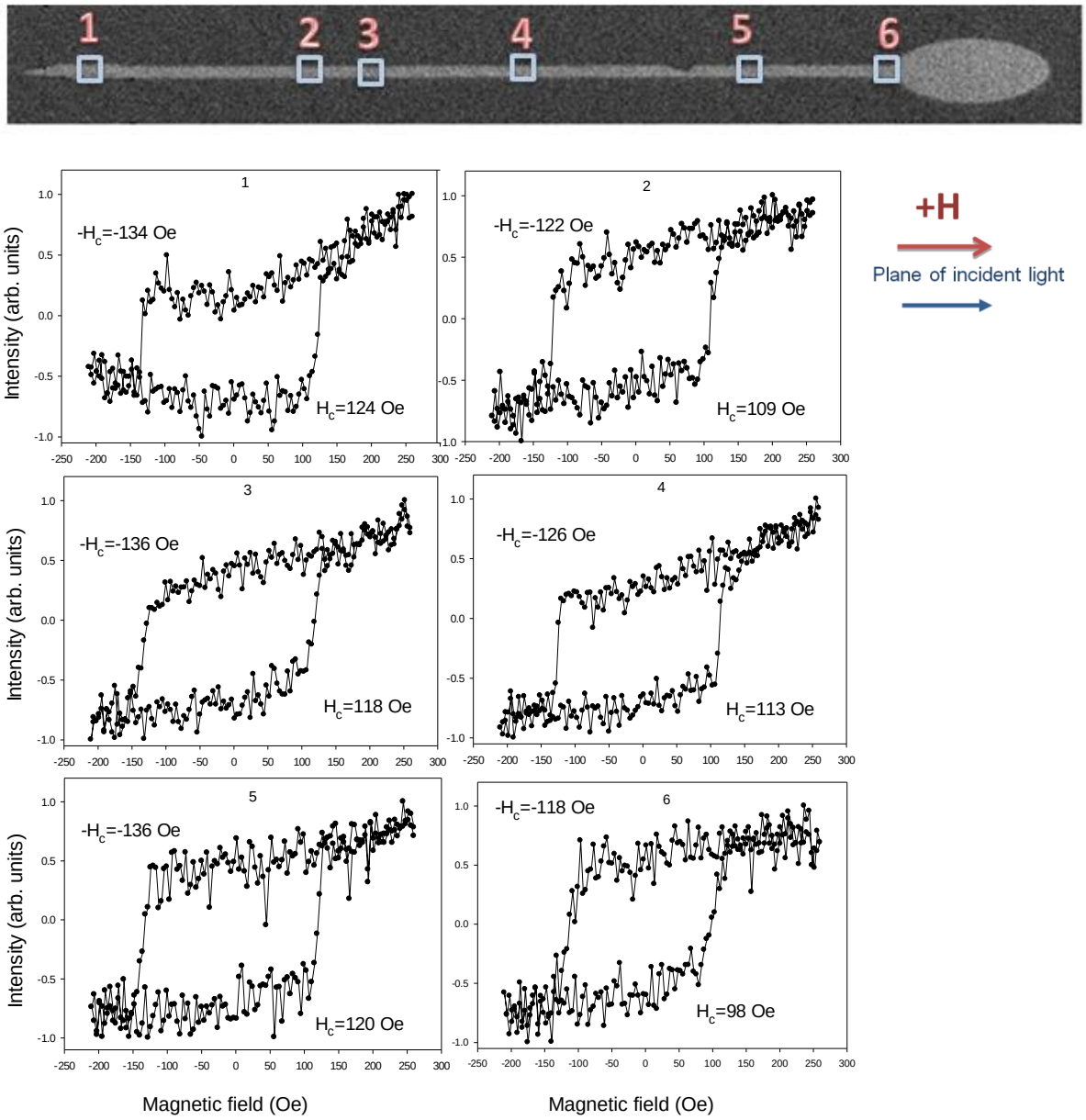

Figure 3.26: SEM image of sample 6 (top) with numbered ROIs (regions of interest). Hysterersis loops (bottom) of sample 6 at different ROIs.

Similar to sample 12, there are three parts that undergone early magnetisation reversal compared to the other parts. The three parts are part 2, 4 and 6 in which their reversals can be observed in image C at magnetic field of -128 Oe and also image H at magnetic field 119 Oe both in Figure 3.27. Referring to the hysteresis loops result in Figure 3.26, the two last magnetisation reversals occur together at part 5 and 1. This concludes that the domain wall produced from the junction at the pad and the wire did not progress to the notch, not until when the magnetisation in part 5 reversed, then after that the domain walls disappear.

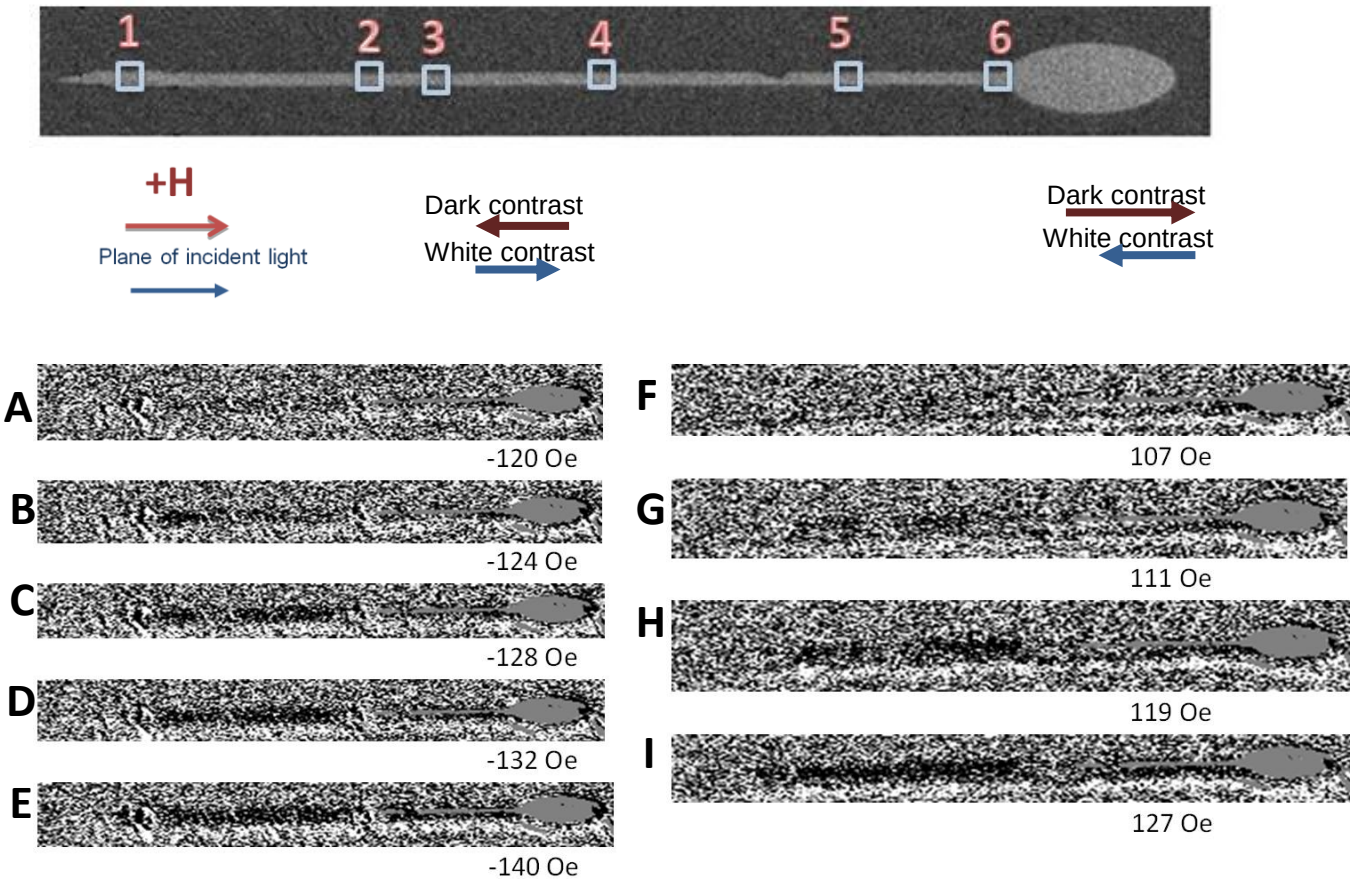

Figure 3.27: SEM image of sample 6 (top) with numbered ROIs. Magnetic images (bottom) of sample 6 at different magnetic field. Dark contrast represents magnetisation reversal in the area by the applied magnetic field. The grey region on the pad of the nanowire is saturated pixels region of the camera.

Result of a 245 nm width nanowire

This wire is a broken wire although it was fabricated to be nanowire with notch shape. The results in Figure 3.28 strongly prove that the Kerr microscope is capable of observing magnetic domains in a sample as small as 245 nm width although the resolution limit of the microscope is at 505 nm. This supports the technical success of this experiment in observing magnetic domains in ultrasmall magnetic sample.

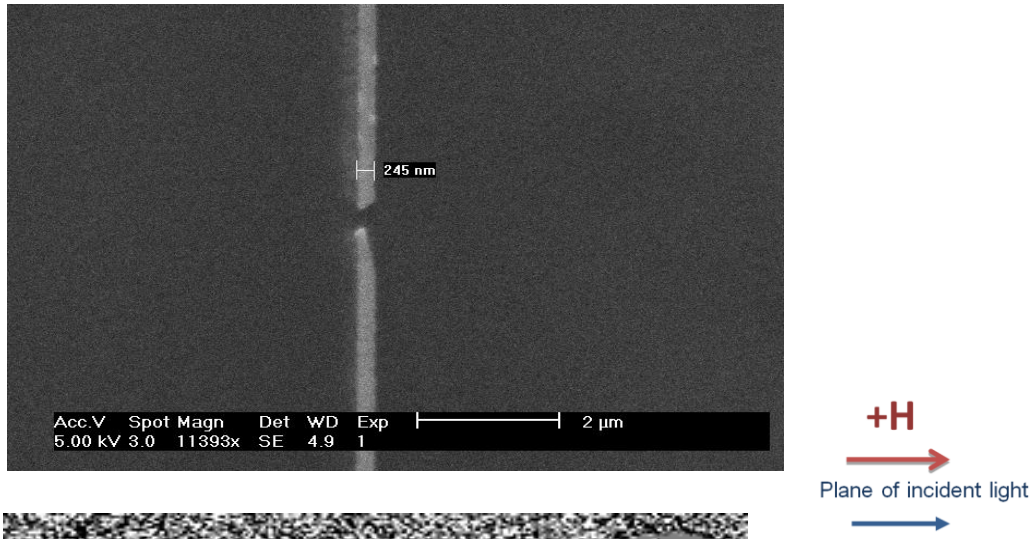

Figure 3.28: SEM image of the 245 nm width nanowire (top) and magnetic images (bottom) at different magnetic fields. The magnetic images prove that the Kerr microscope setup is capable of observing magnetic image of sample as small as 245 nm widths.

3.6.4 Discussion

In general, the examined results of the group two wires agree with the magnetostatic energy and shape anisotropy effects on the samples which cause the lower coercivity of the nucleation pad than the nanowire. Moreover, the magnetisation direction is along the easy axis for the wire part and for the nucleation pad the magnetisation directions are forming vortex along the edges. A new phenomenon is observed in the group two wires where there are multiple magnetic domains formation upon magnetisation reversal. This could open a new path of research for the possible application of this new behaviour of notched wire with nucleation pad. The magnetic domains pattern is repeatable and forms at both positive and negative applied magnetic fields. Therefore, each domain

can be encoded as storage information and has the possibility to be used as magnetic storage devices. As seen from the hysteresis loop results, the asymmetric notch caused different coercivity values at positive and negative applied magnetic field. This is caused mainly by the introduction of notch at the wire.

It is deduced that the reason for the low coercivities difference at areas before and after the notch is because of the high coercivity of the nucleation pad. Similar experiment done using a more circular nucleation pad resulted in a large coercivities difference and is caused by the pinning of domain wall at the notch [34]. This is also proven by the simulation results where the domain wall forms at higher magnetic field and the pinning of domain wall is very weak as shown in Figure 3.19.

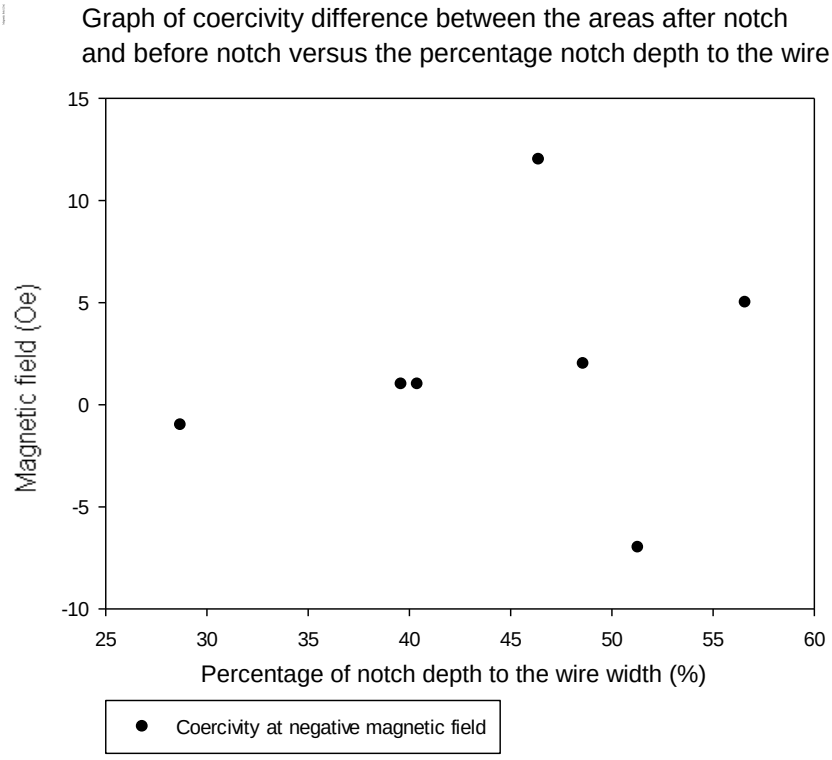

Figure 3.29: Graph showing the relation between the coercivities difference before and after notch with the percentage notch depth.

Instead of strong pinning effect of domain wall at the notch, the wires form multi domains upon reversal giving a non-linear relationship of the coercivities

difference before and after notch related to the percentage notch depth. The non-linear result is shown in the graph at Figure 3.29. However a relationship between the domain wall propagation at the junction and the percentage notch depth to the wire width is observed. The relationship is shown in graph at Figure 3.30. The graph shows that the deeper the notch is the higher the coercivity at the junction. There is also a relationship between the percentage notch depth to the wire width and the coercivity before notch as shown in graph at Figure 3.31. This graph shows that, if the nanowire widths are considered to be nearly equal, increasing the notch depth will reduce the coercivity value at point exactly before the notch.

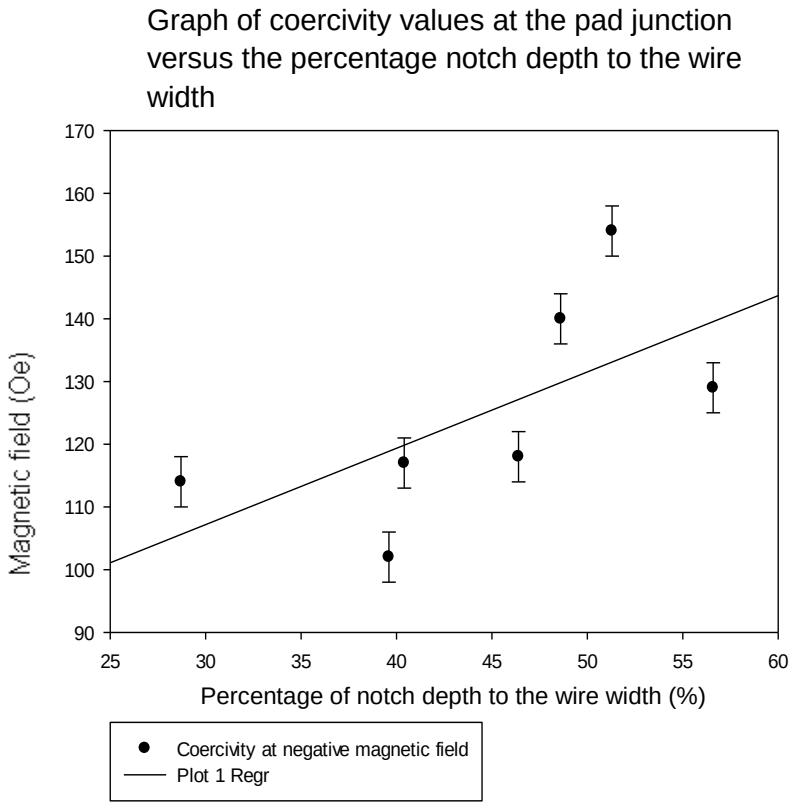

Figure 3.30: Graph showing the relation between the coercivities at the junction between the pad and the wire and the percentage notch depth to the wire width.

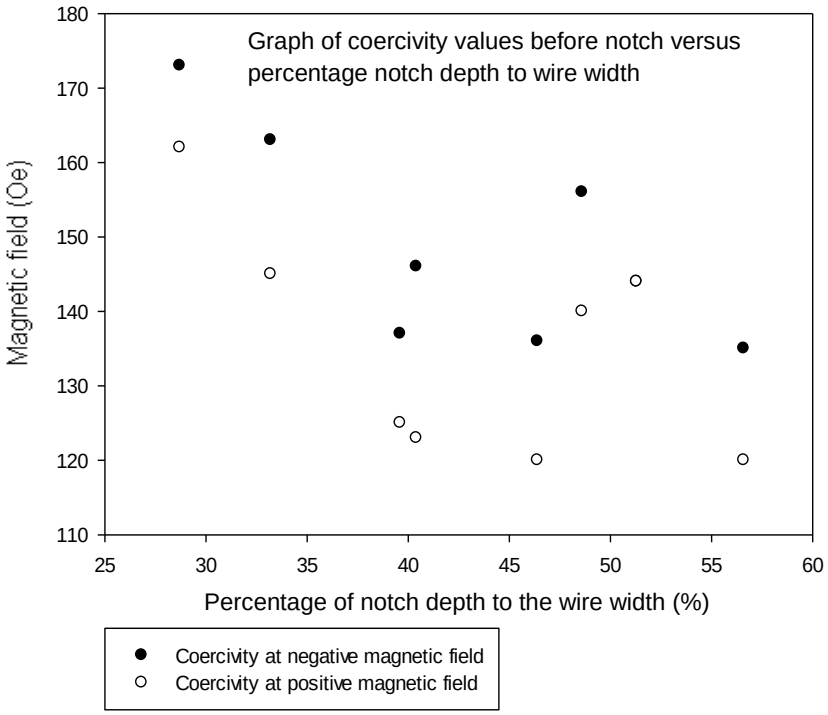

Figure 3.31: Graph showing the relationship between the coercivity before notch and percentage notch depth to the wire width.

4. Summary and conclusions

It has been demonstrated that the Kerr microscope is capable of observing magnetic domains in a sample as small as 245 nm width although the resolution limit of the microscope is at 505 nm. The Kerr microscopy setup makes it possible for the observation of magnetic field driven domain wall propagation in magnetic nanowires. This could be the first wide-field microscopy setup which demonstrated the ability to produce magnetic domains image from magnetic nanostructures. Kerr microscopy remains as the best method for visualization of moving domains in the laboratory due to its flexibility and versatility. Following the outstanding capability of imaging domain motions in nanowire as proven in this research project, it is therefore the most suitable method for magnetic nanowire observation. Furthermore, the ‘homemade’ Kerr microscopy will exceed the limits of commercial wide-field microscopy such as the introduction of cryostats or heating stage at the sample holder. The combination of hysteresis loops and

magnetic domains observations for studying a magnetic sample helps to provide a three-dimensional understanding of the magnetic characteristic of the sample. This is important in investigating nanosamples where the theoretical arguments with the experimental results are always limited by the experimental part. The images captured during the experiment are all saved for future use, thus the data can be analysed so many times for new findings. Therefore, the experiment does not require a repetition if a hysteresis loop result is needed in different part of the sample which is the case for the MOKE magnetometry method. Digital image enhancement helps to increase domains contrast for small objects with very weak Kerr effect. Image averaging from repeated cycles have shown to cause significant contrast enhancement to the magnetic domains image. The Kerr microscopy setup is proven to be capable of investigating Kerr effect at different MOKE geometry.

From the nano objects results, the final image shows an extremely strong domains contrast which have never been achieved before by using wide field microscopy. The observed magnetisation distributions in the nano samples are caused by the magnetostatic energy and the shape anisotropy effect. Domains walls propagation plays an important role in causing magnetisation reversal at lower magnetic field in nanowire. The observed magnetisation alignment along the easy axis of the nanowire confirms with the magnetostatic energy and shape anisotropy theories. Both cross and zigzag nanowires formed multiple domains upon magnetisation reversal and their magnetisation behaviour can be analysed in further detail by observing their hysteresis loops and also their magnetic domains image results.

For the nanowire with notch, the elliptical pad is proven to have lower coercivity than the wire due to shape anisotropy. The observation of weak domain wall pinning by the notch is mainly caused by the large coercivity of the elliptical pad because a lower coercivity nucleation pad is essential so that the domain wall formed will start to progress at lower field. A relationship between the percentage notch depth with the coercivity at the junction was observed in which when increasing the percentage notch depth, the coercivity at the junction increase.

Overall, the microscope setup alongside the developed programmes has proved to be an outstanding method for in-depth investigation of magnetic nano objects.

4.1 Further work

With the unlimited new types of nano structures which can be fabricated, the set up can be used further for magnetic domains observations of these nano objects. With the newly achieved high domain contrasts image, a variety of nanostructures can be investigated. A temperature dependent experiment on nanowires with notch can be done in the future by using the setup. A domain wall pinning experiments for different nucleation pad and different notch shapes can be continued. A temperature dependent domain wall motion visualisation can be done in the future as this setup is proven to produce very strong magnetic domains for small magnetic structures. Experiments that focus on different coercivities at positive and negative fields can give a new understanding of the magnetic properties of nanowire. With the flexibility and versatility of the Kerr microscope, unlimited experiments on magnetic nano objects can be performed.

5. Appendices

5.1 Appendix 1: Programme to extract the hysteresis loop for the magneto-optical magnetometry

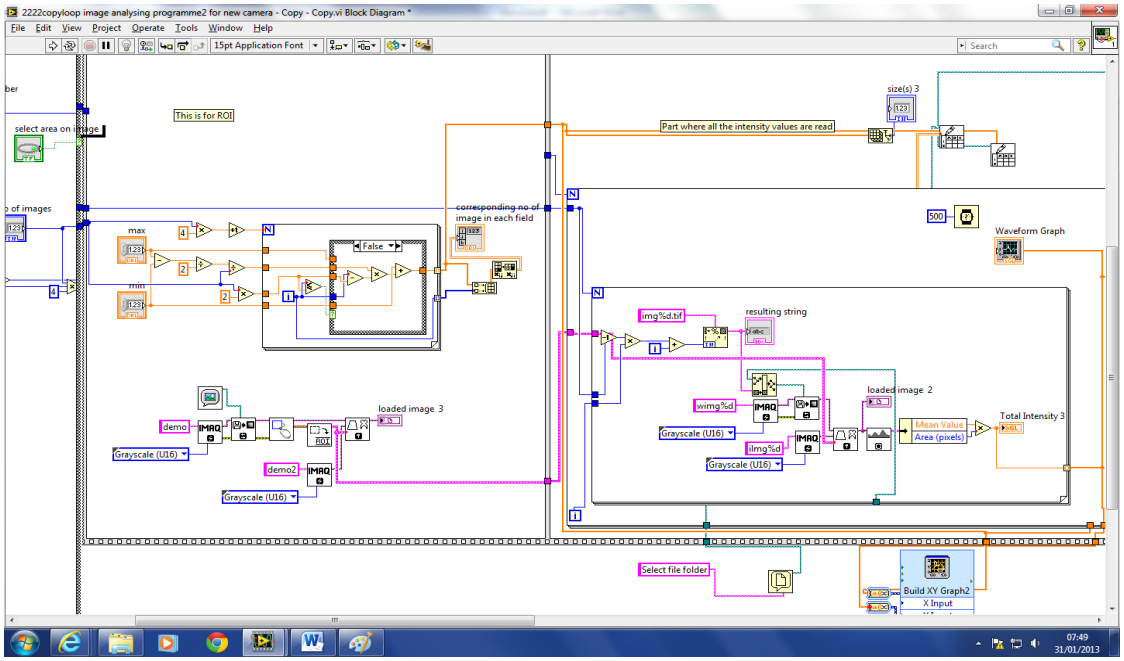

5.2 Appendix 2: Programme for taking a sets of pictures with known magnetic field for each picture

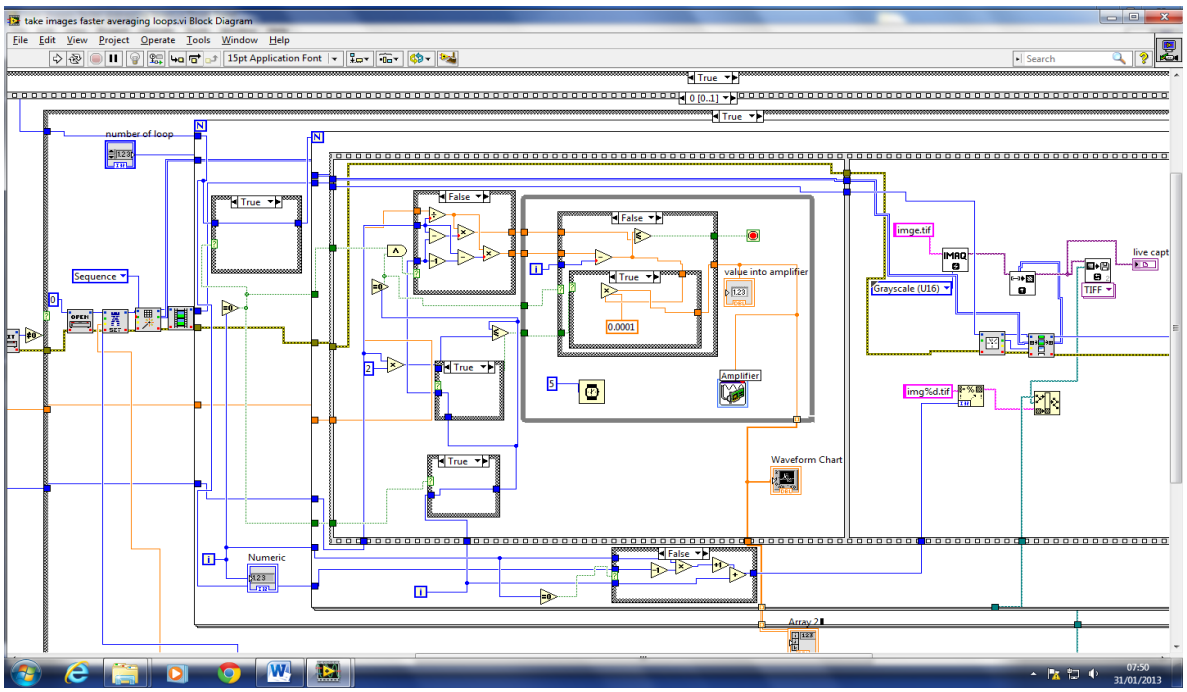

5.3 Appendix 3: Programme to analyse the sets of images and to do digital contrast enhancement

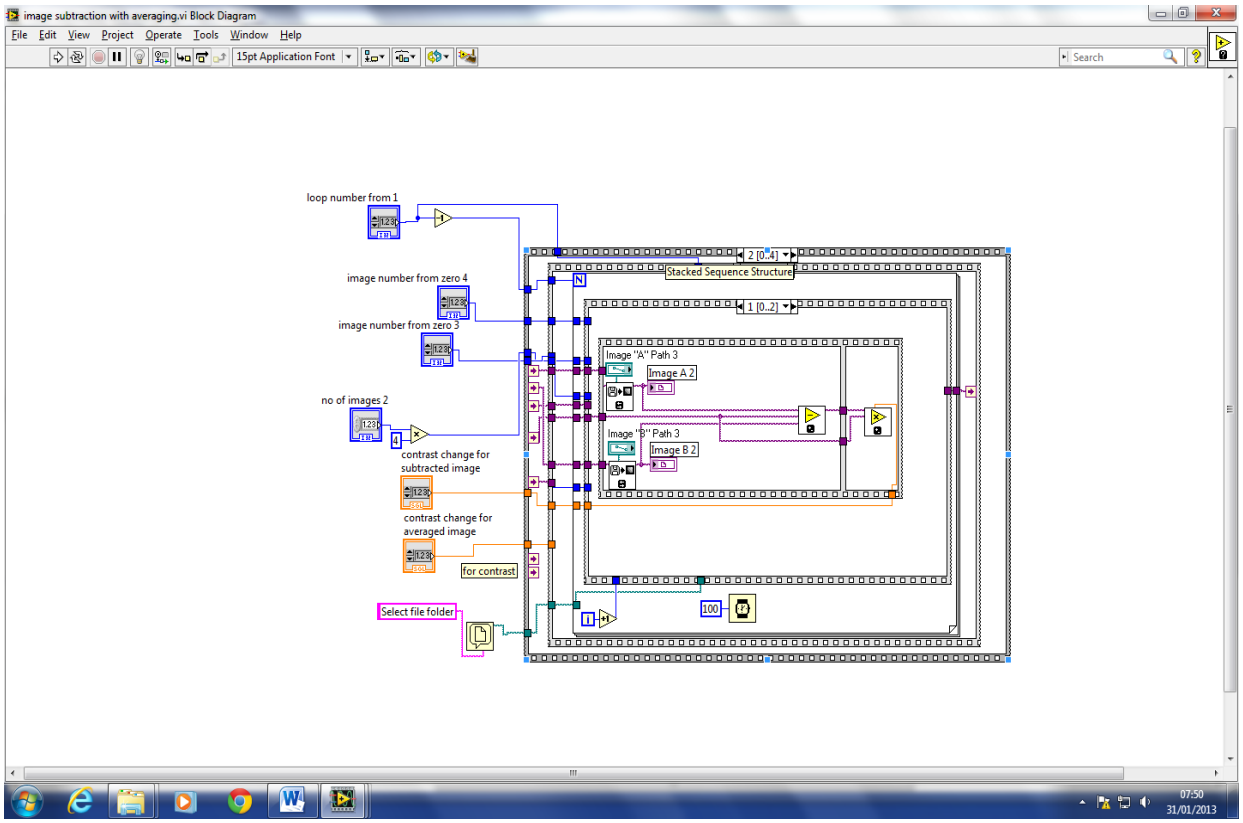

6. Bibliography

[1] B.D Cullity and C.D Graham, Introduction to Magnetic Materials, second edition, Wiley(2009), pp1-2, 115, 102.

[2] Available at <http://www.recording-history.org/HTML/wire2.php> [Acessed: 31 January 2013].

[3] Available at <http://www.emc.com/collateral/analyst-reports/diverse-exploding-digital-universe.pdf> [Acessed: 31 January 2013].

[4] Available at <https://www.ibm.com/developerworks/mydeveloperworks/blogs/storagevirtualization/entry/a_brief_history_of_access_density1?lang=en> [Acessed: 31 January 2013].

[5] M. Tsoi, R. E. Fontana, S. S. P. Parkin, "Magnetic domain wall motion triggered by an electric current", ppl. Phys. Lett. 83, 2617 (2003).

[6] Parkin S S P, Hayashi M and Thomas L, "Magnetic Domain-Wall Racetrack Memor"**,** Science 320 190 (2008).

[7] M. T. Bryan, T. Schrefl, D. A. Allwood, "Symmetric and asymmetric domain wall diodes in magnetic nanowires", Appl. Phys. Lett. 91, 142502 (2007).

[8] D. A. Allwood, G. Xiong, C. C. Faulkner, D. Atkinson, D. Petit, and R. P.Cowburn, "Magnetic Domain-Wall Logic", Science 309, 1688 (2005).

[9] Weiss, P., "La variation du ferromagnetisme avec la temperature" (The variation of ferromagnetism with temperature) Comptes Rendus 143 (1906), pp 1136-1139.

[10] Weiss, P., "L'Hypothese du champ moleculaire et de la propriete ferromagnetique", (The hypothesis of the molecular field and the property of ferromagnetism) Journal de Physique et le Radium 6 (1907), pp 661-690.

[11] David Jiles, Introduction to Magnetism and Magnetic materials, Second Edition, Published by: Chapman & Hall, (1998), p138.

[12] Amikam Aharoni, Introduction to The Theory of Ferromagnetism, second edition, Oxford University Press (2007), P 5, 35.

[13] Available at <url:http://physics.unl.edu/~tsymbal/teaching/SSP-927/Section%2016_Magnetic_ Properties_2.pdf> [Accesssed: 31 January 2013].

[14] Available at <url:http://physics.unl.edu/~tsymbal/teaching/SSP-927/Section%2016_Magnetic _Properties_2.pdfPhysics 927 E.Y.Tsymbal 1 Section 16: Magnetic properties of materials (continued).> [Acessed: 31 January 2013].

[15] Heisenberg, W., “Zur theorie des ferromagnetismus” (On the theory of

ferromagnetism) Zeitschrift fur Physik A 49 (1928), pp 619-636.

[16] Available at <url: http://www.ndt-ed.org/EducationResources/ Community College/MagParticle/Physics/HysteresisLoop.htm> [Acessed: 31 January 2013].

[17] Sixtus, K. J., and Tonks, L., “Propagation of large Barkhausen discontinuities”, Physical Review 37 (1931), pp930-958.

[18] Bitter, F., “Experiments on the nature of ferromagnetism”, Physical Review 41 (1932), pp 507-515.

[19] Landau, L.D., and Lifshitz, E., “On the theory of the dispersion of magnetic permeability in ferromagnetic bodies”, Physikalische Zeitschrift der Sowjetunion 8 (1935), pp 153-169.

[20] Available at:<http://www.birmingham.ac.uk/research/activity/metallurgy-materials/magnets/background/magnetic-materials-domains.aspx> [Acessessed: 31 January 2013].

[21] Bruce M. Moskowitz. (1991), Hitchhiker's Guide to Magnetism, Available at <url: http://www.irm.umn.edu/hg2m/hg2m_c/hg2m_c.html.> [Accessed: 27th, Jan, 2013].

[22] Kronmuller H., and Fahnle M., Micromagnetisation and the microstructure of ferromagnetic solids Cambridge University Press, Cambridge (2003).

[23] Robert C. O'Handley, Modern Magnetic Materials Principles and Applications, Wiley-Interscience Publication (2003), p 184, 289.

[24] Bozorth, R. M., "Directional ferromagnetic properties of metals", Journal of Applied Physics 8 (1937), pp 575-588.

[25] Available at <url:http://physics.unl.edu/~tsymbal/teaching/SSP-927/Section% 2016_Magnetic _Properties_2.pdfPhysics 927 E.Y.Tsymbal 1 Section 16: Magnetic properties of materials (continued). > [Acessed: 18 January 2013].

[26] Neel, L., "Energie des parois de Bloch dans les couches minces" (Bloch wall energy in thin films) Comptes Rendus de l'Academie des Sciences 241 (1955), pp 533-536.

[27] Available at <url:http://www.solutioninn.com/physics/solid-state/general-problem/neel-wall-the-direction-of-magnetization-change-in-domain> [Acessed: 31 January 2013].

[28] M. Herrmann, S. McVitie, and J. N. Chapman, "Investigation of the influence of edge structure on the micromagnetic behavior of small magnetic elements", J. Appl. Phys. 87, 2994 (2000).

[29] X. Liu, J. N. Chapman, S. McVitie, and C. D. W. Wilkinson," Reversal mechanisms and metastable states in magnetic nanoelements", J. Appl. Phys. 96, 5173 (2004).

[30] Available at <url:http://www.magnetics.group.shef.ac.uk/? Research:Patterned_magnetic_structures> [Acessed: 31 January 2013].

[31] Yoshinobu Nakatani, Andre´ Thiaville, Jacques Miltat, "Head-to-head domain walls in soft nano-strips: a refined phase diagram", Journal of Magnetism and Magnetic Materials 290–291 750–753 (2005).

[32] Diegel, M., Mattheis, R., and Halder E., "360° domain wall investigation for sensor applications" IEEE Transactions of Magnetics 40 (2004), pp 2655-2657.

[33] Weiwei Zhu, Jialin Liao, Zongzhi Zhang, B. Ma, Q.Y Jin, ” Depinning of vortex domain walls from an asymmetric notch in a permalloy”, Nanowire,Appl. Phys. Lett. 101, 082402 (2012).

[34] P. R. Cantwell, U. J. Gibson, D. A. Allwood, and H. A. M. Macleod, “Optical coatings for improved contrast in longitudinal magneto-optic Kerr effect measurements”, J. Appl. Phys. 100, 093910 (2006).

[35] J. N. Chapman, “The investigation of magnetic domain structures in thin foils by electron microscopy”, J. Phys. D: Appl. Phys. 17, 623 (1984).

[36] H. Lichte and M. Lehmann, “Electron holography—basics and applications”, Rep. Prog. Phys. 71, 016102 (2008).

[37] S. Hankemeier, A. Kobs, R. Fro¨mter, and H. P. Oepen, “Controlling the properties of vortex domain walls via magnetic seeding fields”, Phys. Rev. B 82, 064414 (2010).

[38] S. Krause, G. Herzog, T. Stapelfeldt, L. Berbil-Bautista, M. Bode, E. Y. Vedmedenko, and R. Wiesendanger, “Magnetization Reversal of Nanoscale Islands: How Size and Shape Affect the Arrhenius Prefactor”, Phys. Rev. Lett. 103, 127202 (2009).

[39] J. P. Davis, D. Vick, D. C. Fortin, J. A. J. Burgess, W. K. Hiebert, and M. R. Freeman, “Nanotorsional resonator torque magnetometry”, Appl. Phys. Lett. 96, 072513 (2010).

[40] W. Wernsdorfer, “From micro- to nano-SQUIDs: applications to nano-magnetism”, Supercond. Sci. Technol. 22, 064013 (2009).

[41] P. Weinberger, “John Kerr and his effects found in 1877 and 1878”, Philosophical Magazine Letters, 88:12, 897-907 (2008).

[42] Faraday, M., "On the magnetisation of light and the illumination of magnetic lines of force", Philosophical Transactions of the Royal Society (London) 136, 1-20 (1846).

[43] A. Hubert, R. Schäfer, Magnetic Domains,The analysis of magnetic micro-structures, (Berlin) Springer-Verlag Berlin and Heidelberg GmbH & Co. KG (1999).

[44] R. Schafer, "Investigation of domains and dynamics of domain Walls by the magneto-optical Kerr-effect", Handbook of Magnetism and Advanced Magnetic Materials, John Willey & Sons (2007).

[45] G. S. Krinchik and V. A. Artem'ev, "Magneto-optical Properties Of Ni, Co, And Fe In The Ultraviolet Visible, And Infrared Parts Of The Spectrum", Soviet Physics Jept Volume 26, No 6 1968 [Zh. Eksp. Teor. Fiz. 53, 1901-1912 (December, 1967)].

[46] J. Zak, E. R. Moog, C. Liu, and S. D. Bader, "Fundamental magneto-optics", J. Appl. Phys. 68, 4203 (1990).

[47] J. M. Florczak and E. Dan Dahlberg, "Detecting two magnetization components by the magneto-optical Kerr effect", J. Appl. Phys. 67, 7520 (1990).

[48] C. You and S. Shin, "Effects of polarizer and analyzer imperfections in a magneto-optical Kerr spectrometer", J. Opt. Soc. Am. B 17, 910-913 (2000).

[49] Available at <url :http://www.olympusmicro.com/primer/techniques/fluorescence/anatomy/fluoromicroanatomy.html> [accessed at: 31 January 2013].

[50] Ambar, H., Y. Aoki, N. Takai, and T. Asakura, "Mechanism of speckle reduction in laser-microscope images using a rotating optical fiber", Applied Physics B: Lasers and Optics 38, no. 1, 71-78 (1985).

[51] Available at <url :http://www.mitutoyo.com/pdf/E4191-378_010611.pdf > [Accessed: 31 January 2013].

[52] Available at <url:http://sales.hamamatsu.com/assets/pdf/hpspdf/C4742-95-12ER.pdf > [Accessed: 31 January 2013].

[53] Available at <url:Code package http://math.nist.gov/> [Accessed on 31 January 2013].

[54] Gilbert, T. L., “A phenomenological theory of damping in ferromagnetic materials”, *IEEE Trans. Magn.* 40, 3443-3449 (2004).

[55] Serban Lepadatu (2006), ”Domain wall scattering and current induced magnetic switching in patterned ferromagnetic nanowires”, PhD thesis, The University of York.

[56] D. S. Eastwood, J. A. King, L. K. Bogart, H. Cramman, and D. Atkinson , “Chirality-dependent domain wall pinning in a multinotched planar nanowire and chirality preservation using transverse magnetic fields”, J. Appl. Phys. 109, 013903 (2011).

[57] Dorothée Petit, Ana-Vanessa Jausovec, Dan Read, and Russell P. Cowburn, “Domain wall pinning and potential landscapes created by constrictions and protrusions in ferromagnetic nanowires”. J. Appl. Phys. 103, 114307 (2008).

[58] Y. B. Xu, C. A. F. Vaz, A. Hirohata, H. T. Leung, C. C. Yao, and J. A. C, “Bland Magnetoresistance of a domain wall at a submicron junction”, Physical Review B Vol 61, NUMBER 22 (2000).

[59] A. Hirohata, C. C. Yao, H. T. Leung, Y. B. Xu, C. M. Guertler, and J. A. C. Bland, “Magnetic Domain Studies of Permalloy Wire-Based Structures with Junctions”, IEEE TRANS. M., VOL. 36, NO. 5 (2000).

[60] Weiwei Zhu, Jialin Liao, Zongzhi Zhang, B. Ma, Q.Y Jin, “Depinning of vortex domain walls from an asymmetric notch in a permalloy nanowire”, Appl. Phys. Lett. 101, 082402 (2012).

[61] D. McGrouther, S. McVitie, J. N. Chapman and A. Gentils, “Controlled domain wall injection into ferromagnetic nanowires from an optimized pad geometry”, Appl. Phys. Lett. 91, 022506 (2007).

[62] Mi-Young Im, Lars Bocklage, Peter Fischer and Guido Meier, “ Direct Observation of Stochastic Domain-Wall Depinning in Magnetic Nanowires”, PRL 102, 147204 (2009).